Institut für Physikalische und Theoretische Chemie der
Technischen Universität München

Femto- to Nanosecond Time-Resolved Pump-Probe Spectroscopy on Electron Transfer in Ferrocenophanone/Oxazine-1, Merocyanine-3/TiO_2 and Acridine-Modified DNA

Reinhard Haselsberger

Vollständiger Abdruck der von der Fakultät für Chemie der Technischen Universität München zur Erlangung des akademischen Grades eines

Doktors der Naturwissenschaften
(Dr. rer. nat.)

genehmigten Dissertation.

Vorsitzende: Univ.-Prof. Dr. S. Weinkauf

Prüfer der Dissertation:
1. Univ.-Prof. Dr. M.-E. Michel-Beyerle, i. R.
2. Univ. Prof. Dr. N. Rösch

Die Dissertation wurde am 23. 1. 2003 bei der Technischen Universität München eingereicht und durch die Fakultät für Chemie am 12. 3. 2003 angenommen.

Contents

Chapter 1

Introduction

Redox reactions are an important class of reactions in chemistry, physics and biology. They involve charge transfer (in particular electron transfer) between an electron donating species (the donor) and an accepting species (the acceptor). Since the development of electron transfer theory [1.1], [1.2] a significant number of theoretical and experimental efforts resulted in the verification of the fundamental transfer mechanism.

The fastest processes are completed in some femtoseconds. This is the time scale of the oscillation periods of molecular bonds which govern the elementary processes in chemistry and became accessible by the technical progress of laser technology in the last decades (see for example [1.3]). The application of these new techniques in laser spectroscopy not only leads to the observation of the primary transfer step with femtosecond time resolution and tunable excitation and probe wavelengths, but also to the understanding of secondary processes following the charge transfer.

Recently, the studies of photoinduced electron transfer reactions became more and more important because of their central role in biology and photochemistry (see for example the theoretical and experimental work on photosynthesis [1.4]). The first step is the absorption of a photon which excites the electron from a lower state (usually the ground state) into a higher electronic state which is subsequently involved in the electron transfer process.

The reactions following charge separation or charge shift (when the initial donor state was charged) often result in highly reactive atoms or molecules with an unpaired electron which are known as radicals. These species are thoroughly investigated in the last years because of their harmful implication for human tissue. This is a consequence of the fact, that electronically excited molecules or atoms can be strong oxidants and even can induce oxidative damage on DNA itself (for recent reviews, see [1.5]).

It is now well known that a cyclobutane pyrimidine dimer formed by UV irradiation is one of the major photolesions in DNA [1.6] which is highly mutagenic if it is not repaired as soon as possible. For the clarification of a recently discovered light-driven repair mechanism (photoreactivation by the enzyme DNA-photolyase [1.7]), more information is needed about the general mechanism of electron transfer involving small aromatic molecules as acceptors.

However, the dynamics of photoinduced charge transfer are difficult to observe by optical spectroscopy whenever the electronic transitions of short lived molecular intermediates are not well known, overlap, or are located in the experimentally not easily accessible UV range, as is to be expected for small molecules like pyrimidines.

In **Chapter 3** an electron transfer reaction is monitored via its effect on the vibrational frequency of suitable sensor bonds (vibrational Stark-effect). The recent developments in the field of infrared laser technology [1.8] extended the time scale of infrared measurements into the femtosecond time domain, so that even the fastest charge transfer reactions can be followed in real time using such sensor bonds.

The selective observation of suitable transitions requires a source of ultrashort IR pulses with tunable wavelengths, which can be achieved by well established nonlinear optical mixing techniques. These techniques are based on the nonlinear interaction of intense pulses with atoms or molecules in crystals or liquid and gaseous media (see for example [1.9]). A short introduction in the theory of three wave mixing and in particular parametric optical generation (OPG) and amplification (OPA) will be given in the experimental chapter (**Chapter 2**).

Photoinduced electron transfer also plays a fundamental role in solar energy conversion. At present, commercially available photovoltaic devices are dominated by silicon-based devices wich are still more expensive than conventional methods of electricity generation. A promising new approach is the photon-to-current conversion by a photoelectrochemical cell (the ”Graetzel Cell”, [1.10]).

The feasibility of this technique depends on the understanding of interfacial electron transfer between a suitable photosensitizer adsorbed on small semiconductor particles or thin films as the electrode. In these cells the function of light absorption is separated from charge carrier transport, so that their characteristic parameters can be varied independently to optimize the conversion efficiency.

In **Chapter 4** the investigation of a newly synthesized merocyanine dye (Mc3) for its use as photosensitizer of TiO_2-nanoparticles (colloids) in a Graetzel-type cell is reported. After steady-state absorption and fluorescence measurements were applied to characterize the optical properties of the dye/nanoparticle system in solution, the recombination kinetics after photoinduced electron transfer were investigated by nanosecond time-resolved spectroscopy.

Another subject of current research is charge migration in DNA. In the early 90ies the postulate of conduction over large distances (up to 200 Å, ref. [1.11]) led to the conclusion that the easiest-to-oxidize DNA base guanine plays an important role in the observation, that oxidative strand cleavage occurs preferentially in guanine rich sequences [1.12], [1.13].

These findings seem to be in contradiction to the conventional description of charge transfer in donor/acceptor systems with energetically higher lying bridges (superexchange). The clarification of the underlying processes has important implications not only in the understanding of the pathways of oxidative damage and repair in DNA [1.5] but also in the development of biosensoric [1.14] and nanoelectronic devices [1.15].

In order to study the distance dependence of this hole transfer mechanism care must be taken on a reliable donor/acceptor distance. Recent investigations focused on the transfer kinetics of newly developed short synthetical DNA sequences (oligonucleotides) with covalently attached intercalating agents as hole injectors (see for example [1.16]).

Chapter 5 will deal with the investigation of charge migration between an intercalated acridine derivative as hole donor and either the native base guanine (G) or the modified base analogue 7-deaza-guanine (Z) as acceptor over short DNA sequences separated from the donor by one or two (A,T) base pairs.

All following measurements were performed by time-resolved absorption spectroscopy in the pump-probe configuration. In the next chapter a brief review of this technique is given followed by the description of the experimental set-ups for the femtosecond and nanosecond time-resolved measurements, respectively.

Chapter 2

Experimental Methods

2.1 The Pump-Probe Method

A useful method especially for studies of photoinduced transfer reactions is a measurement method, where two independent laser sources are used to first initiate the charge transfer reaction by a strong pump beam and then monitor the temporal evolution of the system by the absorption signal of a weaker probe beam.

2.1.1 Definitions

Consider a sample at a given concentration c in a cuvette of thickness d which is irradiated by a light beam of intensity I_0. According to the Lambert-Beer-law the intensity after traversing the sample is given by

$$\frac{I}{I_0} = \exp(-\epsilon.c.d) \tag{2.1}$$

Here I is the intensity after the sample and ϵ the absorption coefficient of the sample which is dependent on the wavelength of the incoming light and thus displays the individual wavelength characteristics of the molecules.

Taking the logarithm of I_0/I one obtains the absorption A (or extinction E)

$$A = log(\frac{I_0}{I}) = \epsilon'.c.d \tag{2.2}$$

with $\epsilon' = \epsilon/ln(10)$.

If there are several kinds of absorbing molecules in the sample they add up to a total absorption:

$$A_{total} = \sum_{i=1}^{n} A_i = \sum_{i=1}^{n} \epsilon'_i . c_i . d \tag{2.3}$$

When the absorption bands of the different species in the sample don't overlap, we see that the absorption is directly proportional to the population of the state under observation. In this way one can follow the time trace of a state involved in a chemical reaction (e. g. electron transfer).

When ultrafast phenomena are studied, time resolutions down to the sub-picosecond domain are required for optimal performance. This is beyond the resolutions of today's conventional detectors with time resolution of around 1 ns. In this case the method of choice is the time-resolved pump-probe-Method.

2.1.2 The Pump-Probe Set-up

In this set-up we have a pump-laser at a given excitation wavelength and a probe-laser tuned to the characteristic wavelength of the observed state. The sample is photoexcited ("pumped") from the ground-state to the excited state by the strong pump beam and is brought out of thermal equilibrium. The excited state will decay to other states with a characteristic decay time.

By measuring the absorption of the weaker probe beam which is delayed relative to the excitation, the time evolution of the state under study (ground state, excited state, radical pair, ...) can be monitored. The time resolution is now dependent on the temporal convolution of pump and probe pulses (instrument function) and the precision of the variable time delay, whereas the time resolution of the detector has no influence. The importance of a precise and reproduceable time delay between pump and probe is obvious.

2.1.3 Difference-Absorption

The difference-absorption ΔA is the difference between the measured absorption of the sample without excitation and with excitation at a given delay time t.

$$\Delta A = A_{with}(t) - A_{without} \tag{2.4}$$

Because of technical properties the detector signals are not equal to the measured intensities, so the intensities can only be measured proportional to a factor α (detector signal = αI).

$$A = log\left(\frac{\alpha_{ref} I_{ref}}{\alpha_{mess} I_{mess}}\right) = log\left(\frac{I_{ref}}{I_{mess}}\right) + log\left(\frac{\alpha_{ref}}{\alpha_{mess}}\right) \tag{2.5}$$

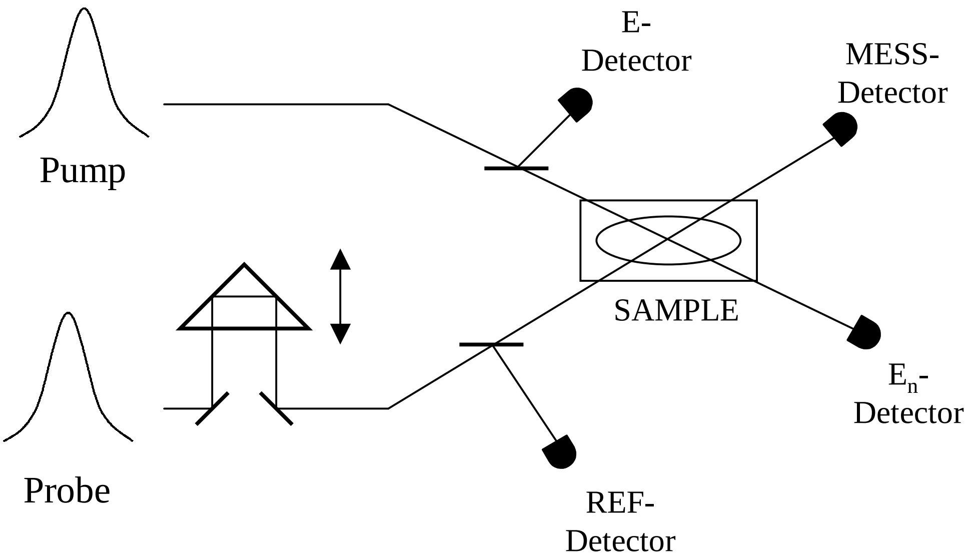

Figure 2.1: Scheme of a pump-probe-experiment with optical delay-line

Here, *mess* and *ref* refers to the detector signals in front of and after the sample, respectively (MESS and REF in figure 2.1).

When we take the difference of two signals from the same detectors, the logarithm of the proportionality factor α cancels. With the notation of figure 2.1 and defining w = with excitation and w/o = without excitation we can write:

$$\begin{aligned} \Delta A &= log\left(\frac{\alpha_{ref} I_{ref,w}}{\alpha_{mess} I_{mess,w}}\right) - log\left(\frac{\alpha_{ref} I_{ref,w/o}}{\alpha_{mess} I_{mess,w/o}}\right) = \\ &= log\left(\frac{I_{ref,w}}{I_{mess,w}}\right) - log\left(\frac{I_{ref,w/o}}{I_{mess,w/o}}\right) = log\left(\frac{I_{mess,w/o}}{I_{mess,w}}\right) \end{aligned} \tag{2.6}$$

Because the population of the excited state depends on the excitation energy, the intensity of the pump-beam in front of and after the sample is recorded (E and E_n, respectively) in order to control the stability of the excitation energy and to normalize the difference-absorption to the excitation intensity.

The dependence of the difference-absorption on time and wavelength $\Delta A(\lambda, t)$ is obtained by assuming, that the number of molecules in the sample is constant. Then the total concentration of the molecules under study is the sum of the concentration of the molecules in the ground state c_0 and the molecules in the higher excited states c_i (i = 1, 2, ...)

$$c(t) = c_0(t) + \sum_i c_i(t) \tag{2.7}$$

With the absorption coefficients for the ground state and the excited states, $\epsilon_0(\lambda)$ and $\epsilon_i(\lambda)$ (i = 1, 2, ...), respectively, we get with the Lambert-Beer law (equation 2.1)

$$A_{without}(t,\lambda) = \epsilon_0(\lambda) c d \tag{2.8}$$

$$A_{with}(t,\lambda) = \epsilon_0(\lambda) c_0(t) + \sum_i \epsilon_i(\lambda) c_i(t) \tag{2.9}$$

When we take $c_0(t)$ from equation 2.7 and substitute it into the right side of equation 2.9, we obtain

$$A_{with}(t,\lambda) = \left[\epsilon_0(\lambda) c - \sum_i \epsilon_0(\lambda) c_i(t) + \sum_i \epsilon_i(\lambda) c_i(t) \right] d \tag{2.10}$$

and finally

$$\Delta A(t,\lambda) = A_{with}(t,\lambda) - A_{without}(t,\lambda) = \sum_i [\epsilon_i(\lambda) - \epsilon_0(\lambda] c_i(t) d \tag{2.11}$$

When $\epsilon_i(\lambda) - \epsilon_0(\lambda) \neq 0$, the transients of the difference- absorption $\Delta A(t,\lambda)$ give information about the temporal evolution of the population of the involved states (i = 1, 2, ...).

Figure 2.2 shows a simple example for a pump-probe measurement on a charge transfer reaction.

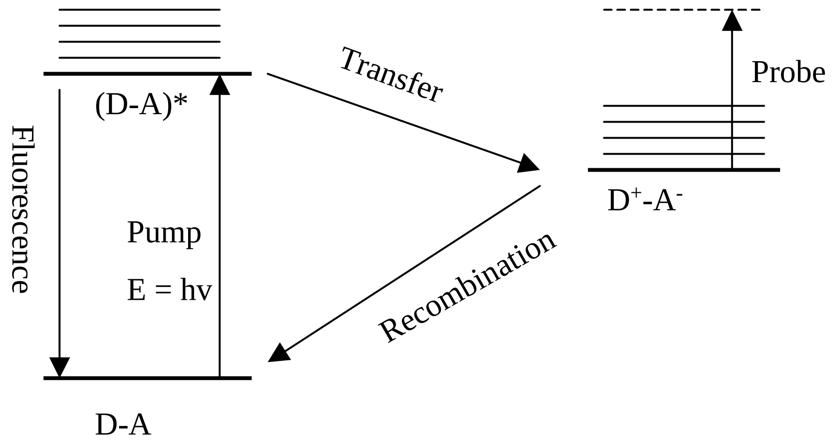

Figure 2.2: Simplified scheme for pump-probe measurements of charge-transfer reactions.

Tuning the probe wavelength to the characteristic absorption bands of the involved states we can get information about the following processes:

- **Ground-state bleaching**: After excitation there are less molecules in the ground state D-A. The absorption decreases and the difference-absorption becomes negative (bleaching). A recovery can occur after recombination of the radical pair or by other competitive processes (fluorescence from excited state or radiationless processes).
- **Excited state decay**: The excited state and its higher lying vibronic substates are formed upon excitation and decay into product states with a characteristic decay-time.
- **Product states**: The time evolution of product states (here: ion pair) can be observed by their characteristic rise times (charge separation of excited state) and decay times (recombination).

2.1.4 Analysis

In order to get information from the measured kinetics it must be kept in mind, that meaningful results can only be extracted when the temporal width of the excitation and probe pulses are considerable smaller than the temporal response of the sample. Since in most applications the pulses cannot be treated as instantaneous perturbations like delta functions, the instrument response function $R(t-t_0)$ (the cross correlation of pump and probe pulses) must be taken into account.

Briefly, he mathematical description is based on the assumption, that there are intermediate states with spectroscopically well-defined properties. Furthermore, the populations N_i of these states obey differential equations of the form

$$\frac{dN_i(t)}{dt} = -\sum_j k_{ij} N_j(t) \tag{2.12}$$

where the matrix of the rate constants k_{ij} has no degenerate eigenvalues.

Then, the experimental data can be fitted to a multi-exponential decay function convoluted with the instrument response function $R(t-t_0)$ centered at the zero point t_0 (here a free parameter):

$$\Delta A(t) = \int_0^{+\infty} \left(\Delta A_0 + \sum_{i=1}^{n} \Delta A_i exp(t'/\tau_i) \right) \times R(t-t'-t_0) dt' \tag{2.13}$$

where $\Delta A(t)$ is the difference absorbance at time t, ΔA_i is the amplitude of the component with lifetime τ_i and ΔA_0 is the offset due to long lived species (for example triplet states).

The instrument response function $R(t-t_0)$ can be modeled by a gaussian function with temporal width (FWHM) t_0 corresponding to the cross correlation of pump and probe pulses. This cross correlation can be experimentally obtained by replacing the sample with a species whose lifetime is much faster than the pulse width, for instance a dye in solution. The resulting time curve will yield the pump-probe cross correlation, which is used to deconvolute the difference absorption data.

2.2 Femtosecond Pump-Probe Measurements

For performing fs time-resolved IR-spectroscopy in the pump-probe geometry a laser-system was established [2.1], [2.2], which amplifies the 100 fs output pulses of a commercially available Ti:Sapphire oscillator by "chirped pulse amplification". The pulses are temporally stretched by a factor of 1000 and are recompressed after amplification in two independent compressors (pump-compressor and probe compressor, respectively) in order to get optimal adjustment for the particular performance of pump and probe, respectively.

2.2.1 The Laser-System

An Ar-Ion Laser (INNOVA 310, Coherent, CW-mode) pumps a passively mode-locked Ti:Sapphire-Laser (MIRA 900F Basic, Coherent). Mode locking is achieved by self focusing the beam in the Ti:Sapphire crystal (Kerr-effect). We get laser pulses with a temporal width of 100 fs (FWHM), a spectral width of approximately 15 nm around 780 mid-wavelength and a repetition rate of 76 MHz.

The output power of 0.5 W (corresponding to appoximately 100 nJ per pulse) is too small for our transient absorption measurements and must be amplified. However, a direct amplifaction is not possible because of the high peak power of 1 MW, which will destroy our amplifier medium. Therefore, we apply the scheme described below and sketched in figure 2.3.

Optical Switch

A combination consisting of a Faraday-rotator, a $\lambda/2$-plate and two thin-film-polarizers (TFP) serves as a "optical switch" to couple the pulses into the desired components. The Faraday-rotator material becomes birefringent, when a magnetic field is applied, i. e. the polarization components of the incident light parallel and orthogonal to an optical axis (here oriented at 22.5 ° to the horizontal) experience different refraction indices. Therefore,

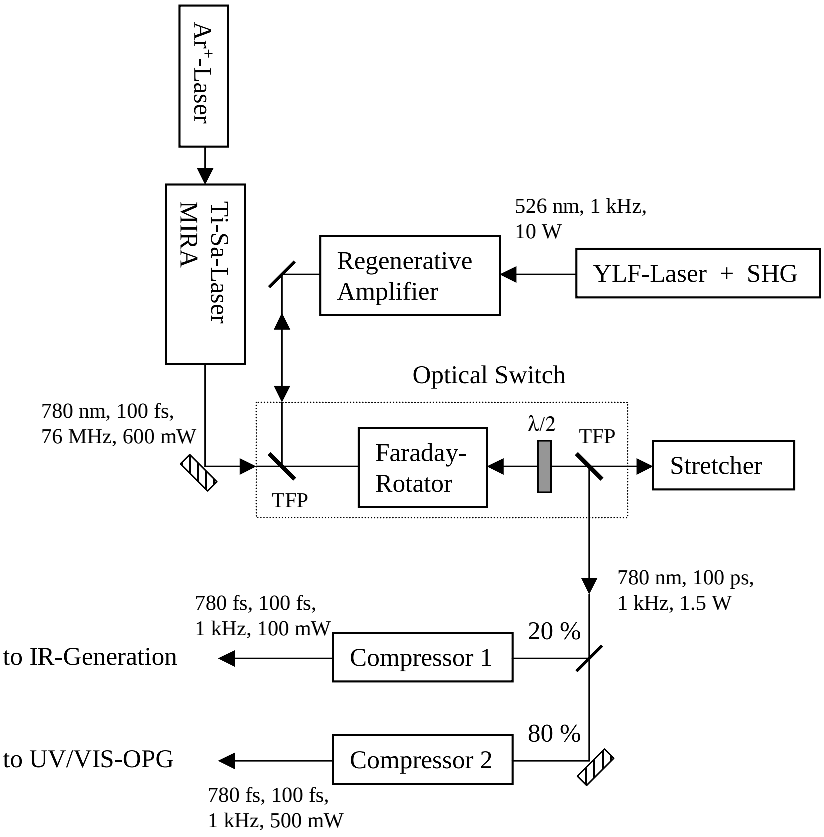

Figure 2.3: Scheme of the laser system for generating pulses with a temporal width of 100 fs. See text for details.

they travel with different velocities through the material. Depending on the strength of the magnetic field and the length of the rotator the polarization of the beam is rotated by a certain angle. This effect is proportional to the vector product of polarization and magnetic field. Thus, the rotation direction is dependent on the direction of the beam.

A $\lambda/2$-plate is a material with a permanent birefringence (for example quartz). For a given wavelength it induces a constant phase difference of π ($\lambda/2$) between parallel and orthogonal polarization relative to the optical axis (also oriented 22.5 ° to the horizontal). The polarization of the incident light thus is mirrored by the optical axis.

The thin-film polarizers in front of and behind the Faraday-rotator and the $\lambda/2$-plate transmit horizontally polarized light (parallel to the table) and reflect vertically polarized light.

MIRA pulses are horizontally polarized and pass the first polarizer. In the Faraday-rotator the polarization is rotated by 45 ° clockwise (always seen in the beam-direction). This rotation is canceled by the $\lambda/2$-plate and the pulses are directed to the stretcher.

Pulse Stretcher

To stretch the fs pulses mirrors, prisms and gratings are arranged in such a geometry, that the wavelengths of the laser pulses will have to traverse optical paths of different lengths. In the stretcher a positive group velocity dispersion (GVD) is induced, this means the components with shorter wavelengths (the "blue" part) are delayed with respect to the longer wavelengths (the "red" part). Thus, the pulses are stretched to about 100 ps.

The stretched and still horizontally polarized pulses pass the optical switch in the opposite direction and are rotated by the $\lambda/2$-plate and the Faraday-rotator counterclockwise by 45 ° (vertically polarized). The thin-film-polarizer reflects the pulses to the regenerative amplifier.

Regenerative Amplifier

At the entrance of the regenerative amplifier (BMI Alpha 1000S) there are a Pockel‘s cell (optical axis 45 ° to horizontal), another thin-film-polarizer and a mirror. Like the Faraday rotator a Pockel‘s cell rotates the polarization of an incident beam, but here the birefringence is induced by an applied electric field. Note that this effect does not depend on the direction. Because of the mirror, all pulses must traverse the Pockel‘s cell twice.

The Pockel‘s cell has three possible states:

1. Without electrical field it serves as a $\lambda/4$-plate and converts the vertical polarization after two passes into horizontal polarization. The pulse is coupled into the amplifier.

2. While the first pulse is in the amplifier, the Pockel‘s cell is switched as a $\lambda/2$-plate. All incoming pulses are rejected. The Q-Switch of a frequency doubled Nd:YLF laser (BMI, 621 D) is synchronized with the Pockel‘s cell, so that the pulse is amplified in the amplifier medium (a Ti:Sapphire crystal) by stimulated emission.

3. When the maximal amplification is reached, (observed by detecting the leak transmission of a mirror) the Pockel‘s cell is switched as a $3\lambda/4$-plate, and the pulse is coupled out.

The Pockel‘s cell is operated with a frequency of 1 kHz. Thus, every 76000th pulse is amplified and can be compressed again.

The Compressor

The amplified pulses are vertically polarized and pass the optical switch unchanged. They are reflected by the second TFP and are splitted 20 %/80 %. In the compressors the pulses experience a negative group velocity dispersion, i. e. the geometry of a grating and a prism leads to the delay of the red part of the pulses relative to the blue part.

2.2.2 Synchronization and Data Acquisition

Right after the MIRA a small part of the beam is reflected to a photodiode. The frequency of the detector signals are reduced by a divider from 76 MHz to 1 kHz and is used as trigger for synchronizing the regenerative amplifier (Pockel‘s cell and Nd:YLF-Q-Switch). A security circuit connected to the trigger electronics blocks the Q-Switch-trigger, when the Ti:Sapphire oscillator shows too high fluctuations. Moreover, the frequency of the Nd:YLF can be varied from 1 Hz to 1 kHz.

Triggering of the measurement electronics (CAMAC, Computer Aided Measurement and Control) is achieved by the signal of a photodiode at the exit of the regenerative amplifier.

The signals of the measurement detectors are digitalized by an ADC (10-bit Anolog-to-Digital Converter, LeCroy 2249SG) and are integrated in a 200 ns time gate. The ADC output signals are transferred via a IEEE-interface to a computer. With a self developped C program they can be stored and processed. The program also drives a delay line (hollow retroreflector, Laser Components) for pump-probe delay. With proper statistics (1000 shots per measurement point) a resolution of 0.1 mOD with a time resolution of 6.67 fs is obtained.

2.3 Nonlinear optical Processes

To generate and amplify the desired wavelengths for the excitation of oxazine-1 (650 nm) and for probing the vibrational bands of carbonyl (around 5.8 μm), we will use the widespread method of three-wave-mixing. In this method new wavelengths can be generated and amplified by the second order interactions of intense ultrashort pulses in nonlinear crystals. These are crystals with not more than one axis of rotation symmetry (optical axis) and are also called *uniaxial*.

After amplification, the higher pulse peak power gives rise to higher order interactions in the nonlinear medium. In the following, there is a list of the most important processes, which will be described in more detail below:

- Optical parametric generation (OPG) and optical parametric amplification (OPA) of the sum frequency of two incident light waves with frequency ω_1 and ω_2: $\omega_3 = \omega_1 + \omega_2$
  A special case of this process is the second harmonic generation (SHG). In this process both frequencies are equal: $\omega_1 = \omega_2 = \omega$. The frequency of the new light wave is doubled: $\omega_3 = 2\omega$.
- Optical parametric generation and amplification of the difference frequency of two incident light beams $\omega_3 = \omega_1 - \omega_2$.
- Spontanous parametric fluorescence: One incident light wave of frequency ω gives rise to two new frequencies $\omega = \omega_1 + \omega_2$

2.3.1 Wave Equation in Nonlinear Media

An electromagnetic field is described by the field vectors $\vec{E}$ (electric field), $\vec{D}$ (electric displacement), $\vec{H}$ (magnetic field) udn $\vec{B}$ (magnetic displacement). Their interaction in a dielectric medium without charge density can be derived from Maxwellt's equations:

$$rot(\vec{H}) = \frac{\partial \vec{D}}{\partial t} \tag{2.14}$$

$$rot(\vec{E}) = -\frac{\partial \vec{B}}{\partial t} \tag{2.15}$$

$$div(\vec{B}) = 0 \tag{2.16}$$

$$div(\vec{D}) = 0 \tag{2.17}$$

The electric and magnetic displacement vectors are given by

$$\vec{D} = \epsilon_0 \vec{E} + \vec{P}(\vec{E}) \quad \text{und} \quad \vec{B} = \mu_0(\vec{H} + \vec{M}(\vec{B})) \tag{2.18}$$

with $\vec{P}$ and $\vec{M}$, the electric and magnetic polarization, respectively. ϵ_0 and μ_0 are the electric and magnetic permeabilities in vacuum.

In a nonlinear crystal the vector of the induced polarization $\vec{P}$ in general is not parallel to the vector of the electric field $\vec{E}$. The specific components must be written in the following way:

$$P_i = \epsilon_0(\chi^{(1)}_{ij} E_j + \chi^{(2)}_{ijk} E_j E_k + \chi^{(3)}_{ijkl} E_j E_k E_l + \ldots) \tag{2.19}$$

with $\chi^{(n)}$ the susceptibility tensor of n-th order and summation over the indices j, k and l. We obtain

$$\vec{D} = \epsilon \vec{E} \tag{2.20}$$

with $\epsilon = \epsilon_0(1+\chi)$.

These equations hold for the assumption, that the wave suffers no dispersion in the medium. This precondition is fulfilled, when there is a lossless transmission in the wavelength region under study. Moreover, we can assume plane waves with a frequency ω and a wavenumber $k = n(\omega)\omega/c$, the absolute value of the propagation vector $\vec{k}$.

The processes mentioned above (OPG, OPA, ...) are results of the interaction with the second term on the right side of equation 2.19. The polarization is proportional to the square of the electric field $P(2\omega_1) \propto E^2(\omega_1)$.

The third term at the right side induces third order interactions (four-wave-mixing). These interactions can also be observed in linear media provided that the peak power of the incident light is high enough. Important applications are third harmonic generation (THG), Raman scattering or self-focusing by Kerr-effect.

For the second order nonlinear coefficients the symmetry condition $\chi_{ijk} = \chi_{ikj}$ holds, because the exchange of E_j with E_k has no physical meaning. That‘s why they are often given in the reduced Voigt-notation d_{ij}. The first index is written as x = 1, y = 2 and z = 3 and the last two indices are replaced by xx = 1, yy = 2, zz = 3, yz = zy = 4, xz = zx = 5, xy = yz = 6.

2.3.2 Phase-Matching Condition

The nonlinear interaction gives rise to the generation of a new electromagnetic wave with the frequency $\omega_3 = \omega_1 \pm \omega_2$. The incoming waves traverse the medium with the phase velocity $v_{ph} = \omega_{1,2}/k = c/(n\omega_{1,2})$ (n is the refractive index with the relation $n^2 = \epsilon/\epsilon_0$). However, the microscopic contributions generated by atoms or molecules at different positions in the nonlinear medium can only add up to a macroscopic wave of appreciable intensity if the vectors of the phase velocities of the inducing waves and the polarization waves are properly matched. This ”phase-matching condition” can be written as:

$$\vec{k}(\omega_1 \pm \omega_2) = \vec{k}_1(\omega_1) \pm \vec{k}_2(\omega_2) \tag{2.21}$$

and can be interpreted as the momentum conservation of the three photons involved.

The efficiency of the interaction depends on the overlap region of the focused beams and thus on the angles between the three wave vectors. Maximal efficiency is achieved for collinear propagation of all three waves (figure 2.4). In this case we get with the energy conservation $\omega_3 = \omega_1 + \omega_2$ snd $\omega/k = c/n$:

$$n\omega_3 = n_1\omega_1 + n_2\omega_2 \quad \Rightarrow \quad n(\omega_3) = n_1(\omega_1) = n_2(\omega_2) \tag{2.22}$$

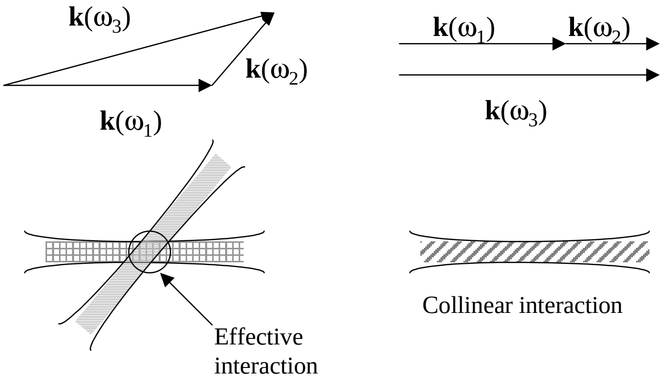

Figure 2.4: Left: Effective interaction for three-wave-mixing. Right: Maximal interaction for collinear case.

Can this condition be fulfilled? We already know that birefringent crystals have two different refractive indices n_o and n_e for the ordinary (polarization orthogonal to the optical axis) and the extraordinary waves (polarization parallel to the optical axis). While the ordinary refractive index is a constant, the extraordinary index depends on both the directions of the polarization $\vec{E}$ and the propagation $\vec{k}$.

2.3.3 Index-Ellipsoid

The refractive indices can be illustrated by the index ellipsoid defined by the three principal axis of the dielectric susceptibility tensor. Consider the electric energy density Ω defined like in isotropic media:

$$\Omega = \frac{1}{2}\vec{E}\vec{D} = \frac{1}{2}\sum_{j,k=1}^{3} E_j \epsilon_{jk} E_k \tag{2.23}$$

The susceptibility tensor ϵ can be diagonalized by a principal axis transformation. This is done by defining the optical axis as z-axis in the coordinate system (x,y,z). Then we have

$$\Omega = \frac{1}{2}\left(\frac{D_x^2}{\epsilon_x} + \frac{D_y^2}{\epsilon_y} + \frac{D_z^2}{\epsilon_z}\right) \tag{2.24}$$

With the substitution $\vec{r} = \vec{D}/\sqrt{2\epsilon_0\Omega}$ we define a unit vector $\vec{r} = (x, y, z)$ in the propagation direction of the plane wave. Then we can write with the relation $n_k^2 = \epsilon_k/\epsilon_0$:

$$\frac{x^2}{n_x^2} + \frac{y^2}{n_y^2} + \frac{z^2}{n_z^2} = 1 \tag{2.25}$$

This is the definition equation for an ellipsoid. For uniaxial crystals, two of the principal axis are equal and the index ellipsoid becomes symmetric with respect to the optical axis.

$$\frac{x^2}{n_o^2} + \frac{y^2}{n_o^2} + \frac{z^2}{n_e^2} = 1 \tag{2.26}$$

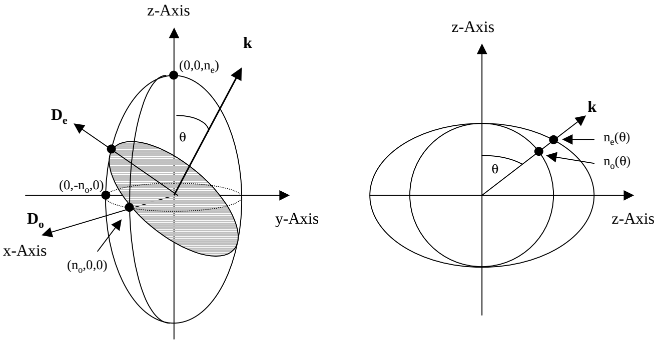

Figure 2.5: Left: Index ellipsoid for a wave with propagation vector $\vec{k}$. Right: Dependence of the refractive indices on the angle θ between the wave vector and the optical axis.

Consider now the propagation vector of a wave, which has an angle θ to the optical axis. We can describe the refractive indices by a plane through the center of the index ellipsoid with its normal in the direction of $\vec{k}$. The intersection of this plane with the ellipsoid forms an ellipse with the principal axes n_o and n_e. As illustrated in figure 2.5 the problem is rotation symmetric around the z-axis, and the extraordinary index is only dependent on the angle θ.

$$\frac{1}{n_e^2(\theta)} = \frac{\cos^2\theta}{n_o^2} + \frac{\sin^2\theta}{n_e^2} \tag{2.27}$$

The uniaxial crystal is called positively birefringent if $n_e > n_o$ and negatively birefringent if $n_e < n_o$. The phase-matching condition for collinear phase-matching can be fulfilled if one of the three waves propagate as extraordinary wave and the others as ordinary waves through the crystal in a direction θ specified by equation 2.22 and 2.26. Figure 2.6 is an example for the generation of the second harmonic $\omega_2 = 2\omega_1$ in a negative crystal. The phase-matching condition for $n_o(\omega_2) = n_e(2\omega_1)$ is fulfilled at the angle θ_{pm}.

One distinguishes between type-I and type-II phase-matching depending on which of the three waves propagates as ordinary or as extraordinary wave:

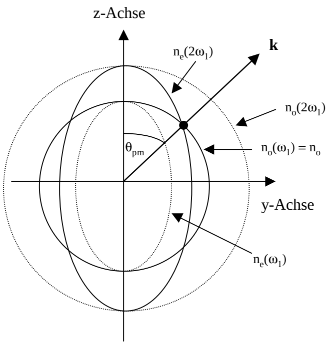

Figure 2.6: Phase-matching in a negative uniaxial crystal for generation of the second harmonic $\omega_2 = 2\omega_1$, θ_{pm} = phase-matching angle

- Type-I corresponds to (1 → e, 2 → e, 3 → o) in positive uniaxial crystals and to (1 → o, 2 → o, 3 → e) in negative uniaxial crystals.

- Type-II is characterized by (1 → o, 2 → e, 3 → o) for positive and by (1 → e, 2 → o, 3 → e) for negative uniaxial crystals.

Until now we only discussed the generation of a new frequency as sum or difference of two original frequencies (optical parametrical generation, OPG). However, the nonlinear interaction can also be used for the amplification of a weak tunable signal wave of frequency ω_1 by a strong pump wave with frequency ω_2 (optical parametric amplificaton, OPA). The resulting third wave with ω_3 is called the idler wave.

Another possibility is the generation of two new frequencies from one strong pump frequency without signal input. This is called spontaneus parametric fluorescence and can only be explained by quantum theory as the interaction of the zero point energies of the generated modes with the pump frequency modes.

Table 2.1 is a brief summary of the described interactions and also gives a short insight in the quantum view (photonic picture), where the problem is described as creation and annihilation of photons in a three-photon-state $|n_1, n_2, n_3\rangle$.

For each of these processes the collinear phase-matching condition in the transparent wavelength region can be fulfilled and the optimal phase-matching angle can be calculated. When the desired interaction and the wavelengths for the three waves are known, the crystal already can be cut to the optimal geometry to achieve maximum efficiency.

In the following experiment BBO (Beta-Barium-Borat, $\beta - \mathrm{BaB_2O_4}$) and

Process	Wave	Frequencies	Photon view
sum frequency	Signal	ω_1	$n_1 \rightarrow n_1 - 1$
	Pump	$\omega_2 < \omega_1$	$n_2 \rightarrow n_2 - 1$
	Idler	$\omega_1 + \omega_2 \rightarrow \omega_3$	$n_3 \rightarrow n_3 + 1$
difference frequency	Signal	ω_1	$n_1 \rightarrow n_1 - 1$
	Pump	$\omega_2 < \omega_1$	$n_2 \rightarrow n_2 + 1$
	Idler	$\omega_1 - \omega_2 \rightarrow \omega_3$	$n_3 \rightarrow n_3 + 1$
optical parametrc amplification	Signal	$\omega_1 < \omega_2$	$n_1 \rightarrow n_1 + 1$
	Pump	$\omega_2 \rightarrow \omega_1 + \omega_3$	$n_2 \rightarrow n_2 - 1$
	Idler	ω_3	$n_3 \rightarrow n_3 + 1$
spontaneous parametric fluorescence	Signal	$\omega_1 < \omega_2$	$n_1 = 0 \rightarrow n_1 + 1$
	Pump	$\omega_2 \rightarrow \omega_1 + \omega_3$	$n_2 \rightarrow n_2 - 1$
	Idler	ω_3	$n_3 \rightarrow n_3 + 1$

Table 2.1: Summary of the interactions in the optical three-wave-mixing

$AgGaS_2$ (Silver-Gallium-Sulfide) are used. Table 2.2 lists some of their porperties.

Crystal	**BBO**	**$AgGaS_2$**
Crystal type	negative uniaxial	negative uniaxial
Nonlinear coeff. $\neq 0$	d_{11}, d_{22}, d_{13}	d_{14}, d_{36}
Transparent region	190 – 3500 nm	0.5 – 13.5 μm
Phase-matching region	400 – 3500 nm	1.8 – 11.2 μm

Table 2.2: Some important properties of the uniaxial crystals used for OPG and OPA.

2.3.4 Excitation

Generation and amplification of the excitation wavelength of 650 nm is achieved by a two stage optical parametric generation and amplification unit (OPG/OPA BMI Venturi II, [2.3]) illustrated in figure 2.7. The delay line is established by the moveable mirrors used for adjusting the overlap between the pulses. Dichroic mirrors reflect the pump at 390 nm (HR = high reflection) and transmit the signal and idler wavelengths (HT = high transmission).

The output of the pump compressor is frequency-doubled to 390 nm (BBO, Type-I phase-matching, cutting angle 28 °) and is splitted in two

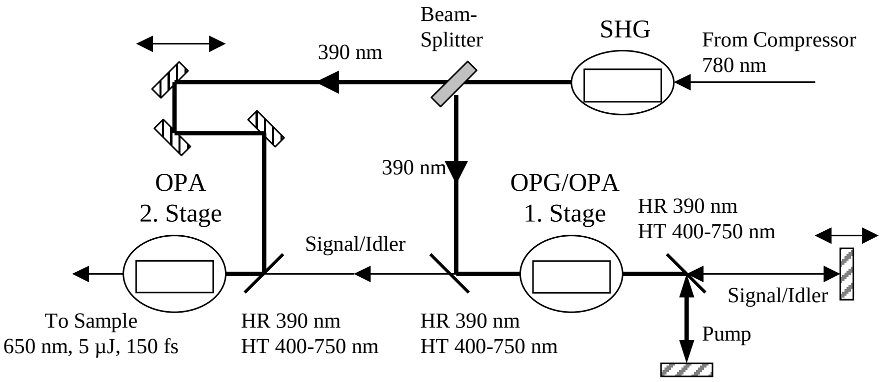

Figure 2.7: Two stage optical parametric generation and amplification of the excitation wavelength of 650 nm

beams used as pump beams for two BBO crystals (optimized for OPG and OPA, respectively, Type-I phase matching). In the first pass through the first crystal the pump generates signal and idler (OPG). After reflection by the mirror and optimal temporal overlap one of the generated wavelengths is amplified by the pump beam (OPA, first stage). Signal or idler beam then overlaps with the second part of the pump beam in the second crystal and is further amplified (OPA, second stage).

Thus, the output of the system covers a wavelength region from the visible (450 - 750 nm, with signal) to the near-IR (850 - 1000 nm, with idler).

After optimal adjustment we got 150 fs pulses with an energy of 5 μJ. Bandpass-filters were used for cutting off pump and idler wavelengths.

2.3.5 IR Generation

IR generation was also achieved by a two stage optical parametric set-up (see figure 2.8).

The hollow retroreflector (Laser Components, gold coated) is controlled by a C program for pump and probe delay. The glass plate reflects approximately 5 % of the beam to a 2 mm sapphire plate. The pulses are focused and produce a white-light continuum, which is a highly nonlinear process involving nonlinear terms of third and higher order. We obtained a broad continous spectrum from 450 nm to 1400 nm.

The red portion of the white light (approximately 15 nm broad) is selected by a dichroic mirror (HR 1300 - 1500 nm/HT 780 nm) and is focused into a BBO crystal (5x4x4 mm, cutting angle 20°, Type-I phase-matching) mounted in a rotation stage (for adjusting the optimal phase-matching angle), where it is overlapped with the delayed pump beam. There, the signal is amplified

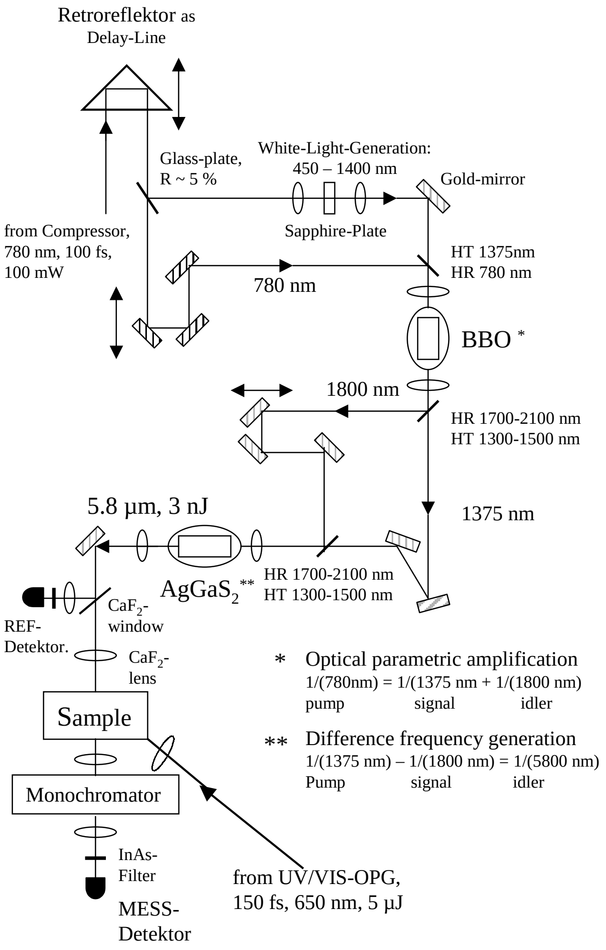

Figure 2.8: Two stage optical parametric IR generation; signal wavelength at 1375 nm and IR output at 5.8 μm (1724 cm^{-1}) used as a calculation example

(OPA, signal wavelength at 1375 nm as an example), thereby producing an idler wavelength at 1800 nm.

Optimal OPA performance could be achieved by recording the signal output with a Ge-detector (Thorlabs, DET 300) after a 1400 nm bandpass filter (Laser components LC-1400 BP10) and monitoring the detector output on an oscilloscope. For wavelengths in the near IR ($\lambda > 1000$ nm) gold coated mirrors (Laser Components, PS 1037C, R > 98.5 % for $\lambda > 1000$ nm) were necessary to guarantee high reflectance.

A dichroic mirror (HR 1700 - 2100 nm/HT 1300 - 1500 nm) splits signal and idler, and the latter is delayed for optimal temporal overlap in the second OPA stage. Signal and idler are combined by another dichroic mirror and are collinearly focused into a $AgGaS_2$-crystal mounted in a rotation stage (2x4x4 mm, cutting angle 35°, Type-I phase-matching). By difference frequency generation a wavelength around 5.8μm (1724 cm^{-1}) was obtained.

The generated IR light had a spectral width of 130 cm^{-1} and an energy of 3 nJ. A spectral resolution of 3 cm^{-1} was obtained by using a 30 cm focal length monochromator (BESTEC Czerny-Turner POC 4M) with a 130 lines/mm grating (blazed for 6 μm) behind the sample. The IR-pulses were detected with liquid nitrogen cooled HgCdTe-detectors (EG&G Judson, MCT J15-D12, with ZnSe-windows) with preamplifiers (EG&G Judson, PA 101).

Lenses and windows were made of calcium flouride (CaF_2), Si-plates (Cut-On 1.2 μm, Transmission approximately 50 % at 6 μm) and InAs-filters (Cut-On 3.55 μm, T approx. 75 % at 6 μm) were used as neutral density filters.

The pump-probe cross-correlation width was estimated to be approximately 200 fs from pump-probe experiments on a thin Si-wafer. For all measurements, the probe polarization was adjusted to be at magic angle (54.7 °) with respect to the pump polarization.

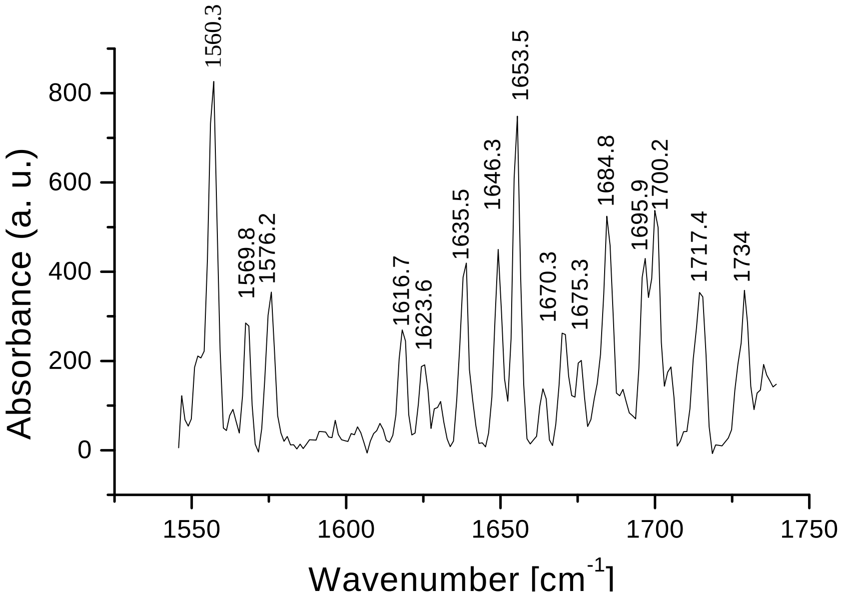

Figure 2.9: Vibration-rotational spectrum of the bending mode of water vapour [2.4] recorded for monochromator calibration

For the monochromator calibration the characteristic vibration-rotational spectrum of the bending mode of water vapour centered at 1595 cm^{-1} (see for example [2.4]) was measured. Figure 2.9 shows their spectral distribution.

Thus, we got a calibration curve of the measured wavenumber versus the monochromator grating angle. In all measurements this background was corrected, and the monochromator was purged with nitrogen.

2.4 Nanosecond Pump-Probe Measurements

Nanosecond time-resolved pump-probe measurements (with an instrument function time resolution of 3.7 ns) are carried out with two independently tunable dye lasers pumped by a Q-switched Nd:YAG laser (excitation) and a nitrogen laser (probe). The pump-probe geometry is sketched in figure 2.4 [2.5]. Time delay between pump and probe pulses is set electronically (described below). The sample resided in a cryostat (for low temperature measurements down to 77 K). With a pair of water cooled Helmholtz coils horizontal or vertical magnetic fields up to 700 G as well as an electric field at the sample location can be generated.

2.4.1 Excitation Beam

A Q-switched Nd:YAG laser (Quanta-Ray 3G, Spectraphysics, 1064 nm, 500 mJ/pulse) with optional second harmonic (SHG, output wavelength 532 nm, 200 mJ/pulse) or third harmonic generation (THG, output wavelength 355 nm, 100 mJ/pulse) is operated in the "short pulse mode".

In the normal mode, a fixed Q-Switch delay would provide a laser pulse with a temporal width of 7 - 9 ns (FWHM). With the help of electronic pre- and post-Q-Switch trigger signals (quasi mode locked Q-Switch) adjustable relative to the optical output pulse, the resulting laser output consists of a main pulse (2.5 ns FWHM) and two stable pre- and post-pulses with approximately 1/3 of the main pulse intensity with a repetition rate of up to 30 Hz.

The desired wavelength is selected by harmonic separators (TecOptics, Harmonic Separators, 45°). A portion of this light is recorded by vacuum photodiodes (ITL TF1850 with S20 and S25 cathode, respectively, 100 ps rise time) to control the energy and the temporal profile of the Nd:YAG output.

Because of the temporal profile of the Nd:YAG pulse with a main pulse and two smaller pre- and post-pulses the dye laser is pumped only slightly above the laser threshold (30 % of the pump beam energy) and is subsequently amplified in a second stage. This reduces the intensity of the side pulses. Polarizers in both beam paths guarantee the right polarization. The direction of the polarization can be adjusted with a $\lambda/2$-plate mounted in the dye laser resonator.

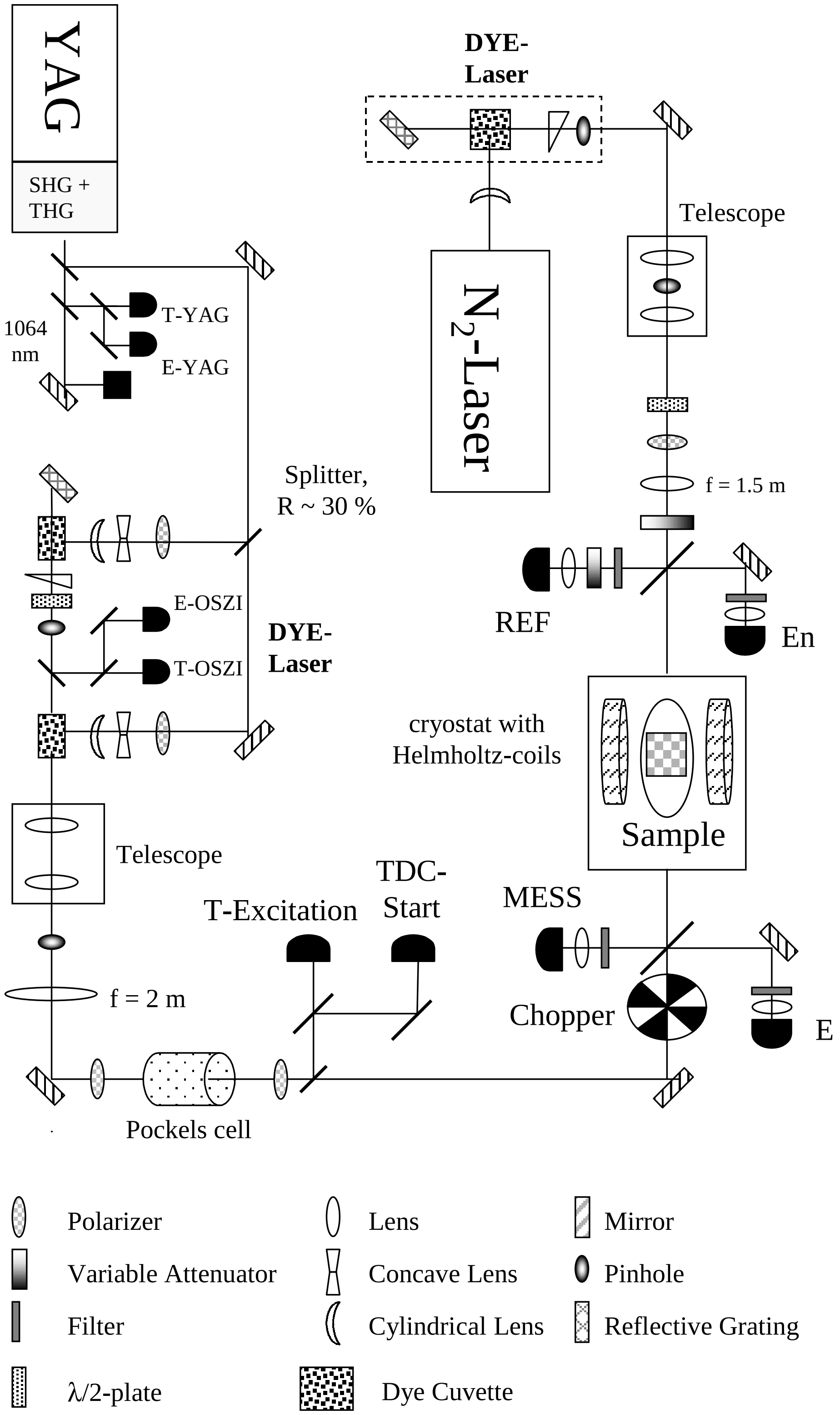

Figure 2.10: Optical set-up for ns time-resolved pump-probe measurements

The YAG pump beam is widened by a negative concave lens and is focused by a cylindrical lens in order to get a focus line uniformely distributed over the hole length of the dye cuvette. To minimize the bleaching due to triplets by the intensive radiation the dye solution is constantly pumped in a closed circuit.

The dye laser is arranged in a Littrow configuration. The resonator consists of a reflective grating and a wedged window. Laser output is achieved by amplifying the first order reflection of the stimulated emission at the reflective grating. The wavelength can be tuned by a rotation stage. To obtain a good approximately gaussian spatial excitation profile a pinhole (0.5 mm) selects a small homogenous portion in the center of the beam. To monitor dye laser performance (energy, temporal profile) a glass plate reflects some percent of the beam to another photodiode.

A confocal telescope (f_1 = 50 mm, f_2 = 120 mm) expands the diameter to approximately 5 mm. Then the beam passes a pinhole (diameter 1.5 mm) before it is focused (f = 2000 mm) into the sample. The final excitation energy (approximately 40 μJ/pulse) can be controlled by a Pockel‘s cell and a polarizer. Without electric field applied the Pockel‘s cell leaves the polarization unchanged. With electric field the polarization is rotated, and the following polarizer attenuates the intensity according to the field strength.

Just in front of and behind the sample a small portion of the light is coupled out and can be monitored. The TDC-start signal is used for synchronizing both the excitation and probe laser (see below). The chopper wheel can be used to permanently block the excitation (for probe beam alignment). Excitation energies in front of (E) and behind the sample (En) are recorded for controlling intensity fluctuations.

2.4.2 Probe Beam

The probe dye laser (also in Littrow configuration) is pumped by a nitrogen laser (MSG 800 TD, LTB Berlin, power output 800 kW) with a wavelength of 337 nm, 0.5 ns pulse length and up to 100 Hz repetition rate.

Beam diameter and spatial profile are adjusted by a confocal telescope with pinhole. The intensity is controlled with a $\lambda/2$-plate in front of a polarizer.

A f = 1500 mm lens focuses the probe beam anti-collinearly relative to the excitation beam into the sample. A pair of mirrors (not shown) is used for vertical and horizontal adjustment of the probe focus to obtain optimal overlap with the excitation focus in the sample and thus a maximal difference absorption signal [2.6]. The probe beam intensity can be controlled by a variable attenuator. To prevent the detectors in front of and after the sample

(REF and MESS in figure 2.4) from saturation, neutral density filters can be added. Scattered excitation light is excluded by cut-on filters (Schottky color filters) or cut-off filters (short pass, Coherent).

2.4.3 Sample chamber

The sample is in a cryostat (Leybold VSK 4-300) connected by a evacuated low temperature line with a liquid nitrogen reservoir (77 K = -196 °C). A PC controls the temperature at the sample cell by setting the nitrogen flow by a electromagnetic valve (Leybold 89021) and by thermoresistive heating (for temperatures up to 323 K (50 °C)).

Temperature measurements are performed with a platin resistor monitored by a digital multimeter (Fluke 8520A). With this program the desired temperature is attained within a few minutes at the chamber walls, but for temperature dependent measurements a waiting time of at least 30 min was necessary to get thermal equilibrium with the sample. Optionally, the cryostat chamber can be flowed with nitrogen gas to exclude measuring artefacts resulting from reactions with oxygen.

2.4.4 Data Acquisition

A HP 9836 computer with GPIB- and GPIO-interfaces controls the measurement electronics ([2.7], figure 2.11). An IEEE-interface is connected by a GPIB cable to a CAMAC crate controller (LeCroy 8901A), which is the control station for the other CAMAC modules: a PDG (Programmable Delay Generator, LeCroy 4222, four channels) for generating up to four pulses with programmable time delays, a TDC (Time-to-Digital Converter, LeCroy 4204) for time difference measurements between two electronic pulses, two pulse-discriminators (LeCroy 821) for generation of a time gate for data integration, and two ADCt's (Analog-to-Digital Converter) for detector read-out (LeCroy 2249A, 10-bit integrator for excitation pulses, LeCroy 2249W, 11-bit integrator for probe pulses).

The first three channels of the PDG trigger the flashlamps and the Q-Switch of the Nd:YAG laser as well as the electric discharge of the nitrogen laser. Each delay can be programmed in 1 ns steps up to a maximum time of 16.7 ms. The fourth channel is used for the Clear signal, which resets the system to be ready for a new cycle.

The output signal of the TDC-START detector is the start pulse for the time measurement by the TDC and the start trigger for the time gate set by pulse discriminator. The output signal of the REF detector serves as TDC-STOP pulse. The time differences can be measured with a resolution from

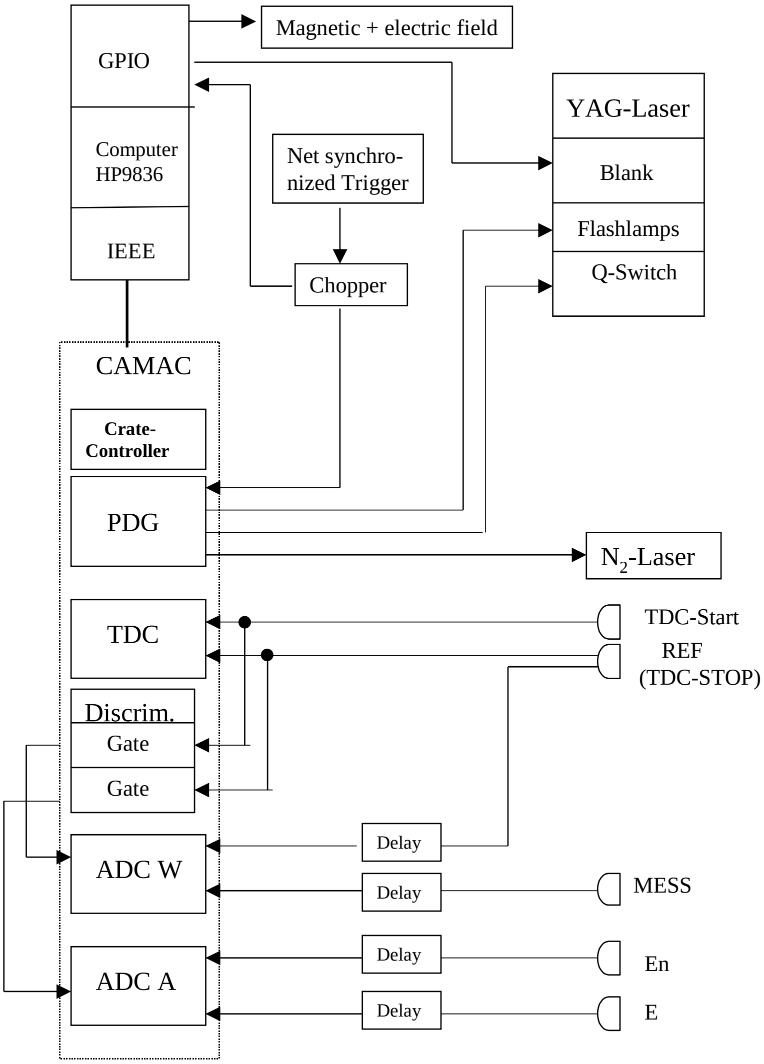

Figure 2.11: Simplified scheme for the measurement control program

0.156 ns (for time delays below 1.3 ms) to 2.5 ns (for maximal time delay of 16.7 ms). An optional offset register is used to measure negative time delays (probe pulse before pump pulse).

A digital GPIO-interface is used to control the magnetic field and to send a periodical BLANK signal to the Nd:YAG laser which blocks the Q-switch for measurement without excitation. Alternatively, the PDG can be programmed in order to permanently block the excitation beam by the spokes of the chopper wheel (necessary for the adjustment of the probe laser).

An external net-synchronized trigger is used to initiate the measurement cycle. The cycle begins with the triggering of the PDG which generates the start signals for the pump and probe pulses at the programmed delay times. The relevant measurement signals are recorded by photodetectors (Si-PIN-diodes, Centronics OSD 60-3T, 2 ns rise time) and are gated into the ADC‘s. ADC- and TDC-signals are then transferred by the GPIB-cable and stored in a memory buffer of the computer where it is available for further data processing. The GPIO-interface also controls the devices for applying electric and magnetic fields.

Because the nitrogen laser shows temporal fluctuations in the pulse generation (jitter), the real delay times can be different from the programmed times. A special drift correction in the program restores the temporal stability. Therefore, the deviations of the TDC-value from the programmed time are recorded and averaged. If the averaged deviation exceeds a determined tolerance, a new trigger time for the nitrogen laser is calculated.

2.5 Steady-State Measurements

Steady-state absorption measurements were performed on a UV/VIS spectrometer (Perkin Elmer, Lambda 2S) with 2 nm resolution. Steady-state emission and excitation spectra were recorded on a spectrofluorometer (SPEX Fluorolog, DM 1680 Series) with 1.7 nm resolution.

Chapter 3

Femtosecond Time-Resolved IR-Spectroscopy

An important class of DNA lesions are pyrimidine-dimers induced by the UV component of sunlight. When there are two neighbouring thymine bases situated at the same strand, UV light with a wavelength below 300 nm can oxidize one of them to form a thymine radical (Thy$^\bullet$).

This radical can further react and form a covalent bond ([2+2]-cycloaddition, [1.6]) to its neighbour (Thy<>Thy, figure 3.1). This entity blocks replication and transcription or can even lead to mutations at the lesion site [3.1]. The cells must eliminate these photoproducts by repair mechanisms as soon as possible.

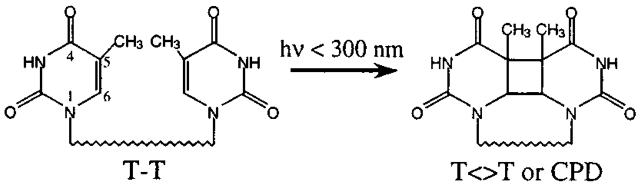

Figure 3.1: Formation of a thymine-dimer by UV light with wavelengths below 300 nm (CPD = Cyclobutyl-Pyrimidine-Dimer).

In the human body this is mainly done by excision repair. Special enzymes cut out a short sequence around the undesired dimer and replace it by a new intact sequence. The old sequence will be degraded and eliminated by metabolic activities.

Another way is photoreactivation by the DNA-photolyase enzyme [1.7]. This enzyme repairs DNA by utilizing the energy of near-UV/visible light to break the cyclobutane ring of the dimer. It is found in members of all three kingdoms of life (bacteria, archaea, eucarya), but is missing in the human body [3.2].

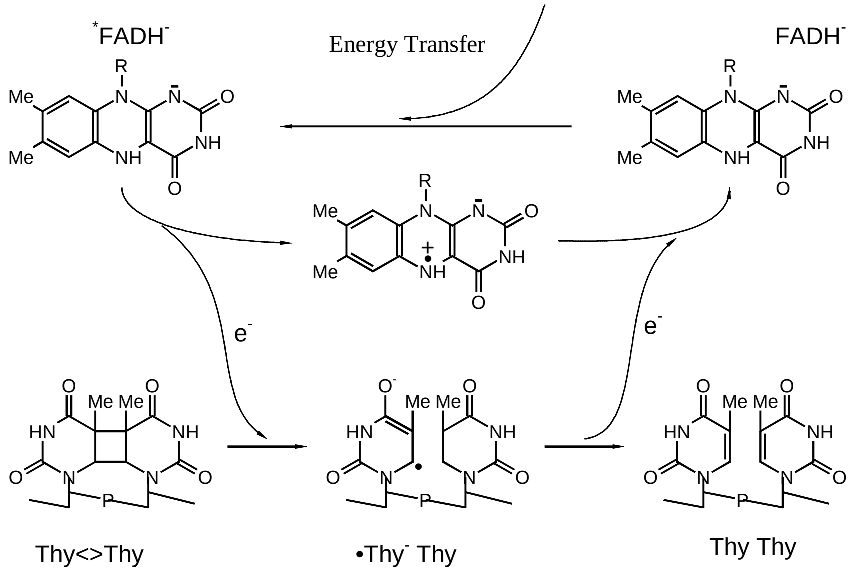

Figure 3.2: Simplified scheme of the DNA-photolyase repair mechanism (photoreactivation).

3.1 The Photolyase Repair Mechanism

This is done in several steps which have to be initiated by absorbing a photon in the near-UV/visible region (300 - 500 nm). A simplified scheme is shown in figure 3.2.

Photolyase is a monomeric flavo-protein of 50 - 60 kDa and contains stochiometric amounts of two chromophores/cofactors. One of them is oxidized flavine-adenine-dinucleotide ($FADH^-$) and the second is either a folate (5,10-MHTF = Methenyltetrahydrofolate) or a deazaflavine (8-HDF = 8-hydroxy-5-Deazariboflavin), depending on the species.

The enzyme binds to the pyrimidine-dimer in a light-independent step. After absorbing the near-UV/visible photon the excited chromophore (flavine or folate) transfers its energy to the other chromophore, which in turn transfers an electron to the Thy<>Thy-dimer. The dimer splits at the 5-5 and 6-6 bonds, and back electron transfer restores the dipyrimidine and the functional form of the flavine-protein ready for a new cycle of catalysis.

Whereas the structure of the involved reaction partners are already known [3.3], theoretical and experimental investigations of the detailed mechanism and dynamics (transfer rates) of the electron transfer process are still under way [3.4].

A first attempt to elucidate the process is to investigate dynamics and mechanism of electron transfer processes leading to Thy<>Thy bond dissociation. This was done using specifically designed intramolecular donor-acceptor-compounds with cyclobutane-bridged pyrimidine-dimers as acceptors (in collaboration with Carell, ETH Zuerich [3.5]). In a first study, the energy transfer in DNA-photolyase from the antenna (deazaflavine) to the electron donor (flavine) was modeled using a hetero-dimer (figure 3.3).

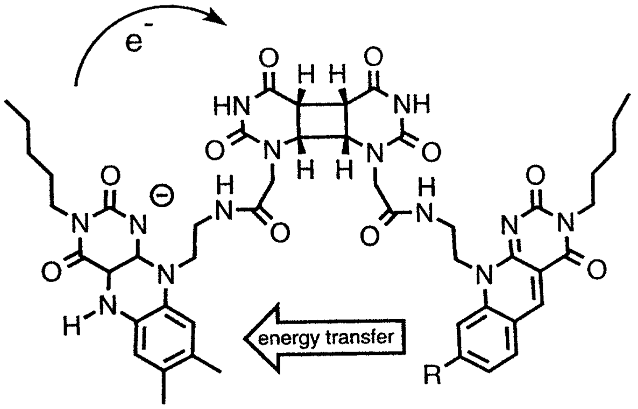

Figure 3.3: Model compound for energy transfer with subsequent electron transfer leading to bond dissociation.

The fluorescence of the antenna, which normally decays with 3 ns, was quenched with time constants of 5 to 60 ps. After excitation of deazaflavine, the fluorescence of the flavine rised with the same time constant. Moreover, the model compound was able to repair the pyrimidine dimer. The dissociation of the compound indicated an electron transfer step after the primary energy transfer.

The next important question is, if the transferred electron will be localized on one ring of the dimer, or if there occurs a further transfer step to the neighbour ring, before it recombines with the cromophore.

To investigate these transfer steps we need model compounds, whose structure match as good as possible with the natural one. Figure 3.4 shows a porphyrine-quinone-triade suitable to study a two step transfer mechanism.

The photoexcited porphyrine acts as the electron donor and the quinones as acceptors. Compound **1** (figure 3.4, left) acts as a reference.

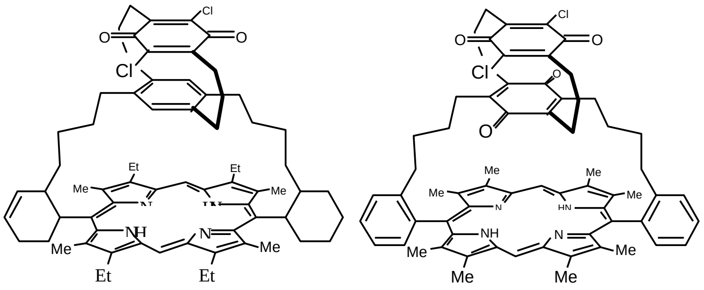

Figure 3.4: Porphyrine-quinone-triades **1** (left) and **2** (right) as model compounds for thymine-thymine-dimers.

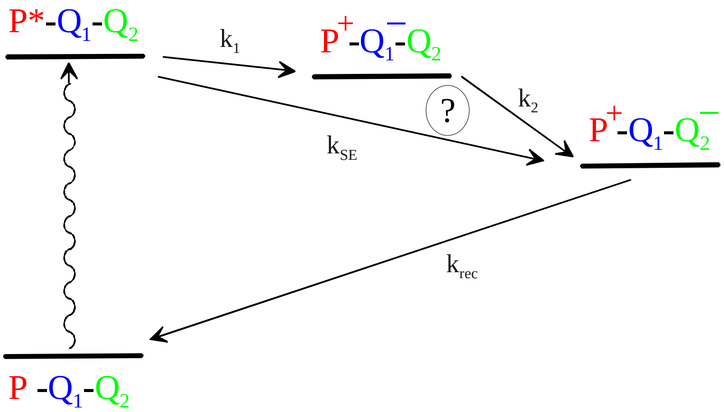

Figure 3.5: Reaction schemes of a superexchange mechanism and a two step transfer from the porphyrine as donor to the quinones as acceptors.

Figure 3.5 shows the principal reaction schemes: Superexchange versus two step transfer. They can be distinguished by transient absorption measurements in the following way:

- The superexchange will exhibit a monoexponential decay curve from the excited porphyrine to the Q_2 anion state. In this scheme the electron will never be localized on Q_1.
- In the two step transfer the two quinone anions will form one after the other giving rise to a two-exponential behavior of the difference absorption.

Because of the lack of suitable electronic transitions of quinones, measurements on porphyrine-quinone-triades in the visible and near IR only yielded information about the oxidation and re-reduction of the donor. As seen in table 3.1 the obtained results are rather ambiguous. A two step behaviour can only be seen in system **2** and **3** (same as **2** but with four CH_2 bridges connecting the quinones) in toluene.

System	Solvent	τ_{cs} [ps]	τ_{cr} [ps]
1	Toluene	180	2500
	MeAc	45	220
	DMF	8	380
2	Toluene	1.5/3.4	145
	MeAc	2.4	12
	DMF	1.9	5.6
3	Toluene	1.2/6.1	390
	MeAc	4.4	34
	DMF	3.3	14

Table 3.1: Charge separation times (τ_{cs}) and charge recombination times (τ_{cr}) for porphyrine-quinone-triades **1, 2** and **3**. In system **3**, four CH_2-bridge elements are connecting the two quinones.

For a more detailed study of the mechanism of charge separation in porphyrine-quinone-triades (two step vs. superexchange) and for the determination of the relevant dynamics (k_1, k_2, k_{SE} and k_{rec}), the redox state of bridge *and* acceptor must be observed.

Using the large shifts of the C=O- and C=C-vibrations of quinones upon reduction, the seperate observation of bridge and donor will be possible with transient absorption measurements in the IR. Vibrational frequency shifts of redox-active sites accompanying a charge transfer reaction are well known. For example in quinones, which have been used widely in electron donor/acceptor compounds [3.7], shifts of the C=O (Carbonyl-Group) and C=C stretching frequencies of more than 100 cm^{-1} occur upon reduction [3.8]. Similarly, upon coordination of CO to metal ions a large shift of the carbonyl frequency is observed, arising from π^*-back-bonding and electrostatic effects [3.9]. This sensitivity of the CO-stretching frequency to the metal charge was used to probe charge transfer reaction in various redox systems involving metal carbonyls down to the picosecond time scale [3.10].

In contrast to these molecular systems, where the electron density at the sensor bond is directly altered by the charge transfer, the vibrational Stark-effect should allow one to monitor changes of the electron density *from a distance.* The sensor group in this case may be either within the molecule under investigation or located in its immediate environment.

3.2 The vibrational Stark-Effect

It is well known that an external electric field affects the vibrational Hamiltonian via its projection on the dipole vector of the vibrational mode, thus altering the frequency and the absorption cross section of the vibrational transition.

Every modification of the charge distribution in a molecule (for example upon charge transfer) not only affects the electronic configuration and thus the properties of the bonds where the charge is localized, but also influences the bonds in its environment by electrostatic effects. The interaction of the electric field with the molecular electron cloud is the origin of a vibrational frequency shift $\delta_{\nu E} = \frac{d\nu}{dE}$ and the modification of the oscillator strength S (a figure of merit for the cross section of the absorption band). In partly charged molecules additional mechanical forces ($\vec{F} = q.\vec{E}$) can cause considerable distortions.

The vibrational Stark-effect deals only with the pure electrostatic interaction by an external electric field $\mathrm{E_{ext}}$. It should be taken into account that the local field $\mathrm{E_{loc}}$ at the bond under study can differ from the external field because of nonlinear polarization effects. Then, the local field in general is not parallel to the external field (i. e. the electrical permeability ϵ is a tensor). Fortunately, we can assume for many practical applications (especially for homogenous fields), that electric field and polarization are parallel. Then the external and local fields are proportional ($E_{lok} = \gamma E_{ext}$) and we have $\delta_{\nu E_{lok}} = \gamma \delta_{\nu E_{ext}}$. In the following this is taken into account and the indices are omitted.

To clarify the physical background a short theoretical description is given. The derivation with the help of time independent perturbation theory follows the notations in [3.11]. Alternative descriptions can be found in reference [3.12] or [3.13].

Without electric field applied the system can be described quantum-mechanically by the time independent Hamilton-operator

$$H(P,Q)\psi = \left[\frac{P^2}{2M} + V(Q)\right]\psi = h\nu\psi \tag{3.1}$$

Solving the Schroedinger equation we get the eigenvalues ($h\nu$) and eigensstates (ψ) of the system.

When the electric field is applied, the Hamilton-operator changes, and we must find a new solution. In the perturbation theory we assume, that the electrostatic interaction is weak compared to the potential energy of the system and should leave the eigenstates unchanged. The problem reduces to the calculation of new eigenvalues.

The perturbation induces a transition between the ground state to the first vibrationally excited state of a mode in which all molecules vibrate in phase. The energy change is the scalar product of the electric dipole with the electric field $\vec{\mu}.\vec{E}$. For simplification we set μ as the component of the dipole in the direction of the electric field. Then the new potential becomes field-dependent: $V(Q,E) = V(Q) - \vec{\mu}.\vec{E}$.

For the C=O group we can assume that their vibration mode is localized on the atom pair, so that we can neglect coupling to other modes. We separate the Hamiltonian into a nuclear and an electronic part (Born-Oppenheimer-approximation).

Then we can write:

$$H = \frac{P^2}{2\mathcal{M}} + V(Q,E) \tag{3.2}$$

Here $\mathcal{M}$ is the effective mass of the system.

We can expand V(Q,E=0) in the absence of the field into a Taylor-series

$$V(Q) = a_{00} + a_{20}Q^2 + a_{30}Q^3 + \dots \tag{3.3}$$

and define Q so, that the potential function has its minimum at Q = 0 (i. e. $a_{10} = 0$).

The coefficients a_{i0} can be obtained from the frequencies of rotational-vibrational transitions [3.14].

Moreover, we can expand the dipole-moment function in the direction of the applied field E:

$$M(Q) = -(a_{01} + a_{11}Q + a_{21}Q^2 + \dots) \tag{3.4}$$

The coefficient a_{i1} can be determined from overtone spectra [3.15].

Now we can write the exact V(Q,E) as a double Taylor-series

$$V(Q,E) = \sum_{j,k} a_{jk}Q^j E^k \tag{3.5}$$

For the calculation of the new eigenvalues we carry out a coordinate transformation of the form $Q'(E) = Q - Q_0(E)$, where Q_0 is the Q at which $V(Q_0, E)$ is a minimum. Note that P is also the conjugate momentum to Q'.

Then we obtain the diagonalized form of the potential function

$$V(Q') = c_0 + c_2(E)Q'^2 + c_3(E)Q'^3 + \dots \tag{3.6}$$

In this form the eigenvalues of the Hamiltonian as a function of the c_i's are known [3.16], [3.17].

When we compare the coefficients of the expansions of V(Q,E) (equation 3.5) and V(Q') (equation 3.6) with the help of the relation

$$\frac{1}{n!}\left[\frac{\partial^n V(Q')}{\partial Q'^n}\right]_{Q'=0} = \frac{1}{n!}\left[\frac{\partial^n V(Q,E)}{\partial Q^n}\right]_{Q=Q_0} \tag{3.7}$$

we get to the first order in E

$$Q_0(E) = -\frac{a_{11}}{2a_{20}}E \tag{3.8}$$

and for i = 2,3,...

$$c_i(E) = a_{i0} + \left[a_{i1} - \frac{(i+1)}{2}\frac{a_{i+1,0}a_{11}}{a_{20}}\right]E \tag{3.9}$$

The eigenvalue ν can then be written in potences of h (Planck's constant):

$$\nu = \frac{1}{2\pi}\left(\frac{2c_2}{\mu}\right)^{1/2} + \frac{h}{(2\pi)^2\mu}\left[(-15/8)\left(\frac{c_3}{c_2}\right)^2 + 3/2\left(\frac{c_4}{c_2}\right)\right] + h^2 \times \dots \tag{3.10}$$

The first term which does not involve Planck's constant, can be obtained classically. The result of successively including $c_2, c_3, ...$ in the calculation of $\delta_{\nu E}$ can be viewed as a series of terms that converge to the exact value.

$$\delta_{\nu E} = \frac{1}{2\pi}\left(\frac{2a_{20}}{\mu}\right)^{1/2}\left[\frac{2a_{20}a_{21} - 3a_{30}a_{11}}{4a_{20}^2}\right] = \nu_0\left[\frac{2a_{20}a_{21} - 3a_{30}a_{11}}{4a_{20}^2}\right] \tag{3.11}$$

where ν_0 is the frequency of the harmonic oscillator.

It can be shown, that higher order terms are smaller than the first order term by at least two orders of magnitude, so that we can neglect them.

The calculation of the interaction of the electrostatic field with the oscillator strength

$$\delta_{SE} = \frac{\partial ln(S)}{\partial E} \tag{3.12}$$

can be made by a similar procedure [3.18].

For a vibrational transition S is proportional to the square of the first derivative of the dipole-moment

$$S \propto \left(\frac{\partial M}{\partial Q}\right)^2 \tag{3.13}$$

Applying another Taylor-series we obtain after diagonalizing the Hamiltonian:

$$\delta_{SE} = 2\left(\frac{2\alpha_1}{a_{11}} - \frac{a_{21}}{a_{20}}\right) \tag{3.14}$$

α_1 is derived from the Taylor expansion for the polarizability α

$$\alpha(Q) = \alpha_0 + \alpha_1 Q + \alpha_2 Q^2 + \dots \tag{3.15}$$

and can be obtained from non-resonant raman-scattering [3.19].

Of particular interest are carbonyl groups with their large IR cross-section around 1700ă cm^{-1}. Ab-initio [3.20] and semiempirical [3.11](b) calculations on formaldehyde predict a tuning rate of the carbonyl vibrational frequency on the order of $5.10^{-7}\text{cm}^{-1}(\text{V/cm})^{-1}$ and a fractional decrease of the absorption cross section by approximately $2.10^{-9}(\text{V/cm})^{-1}$, corresponding to a shift of 45 cm^{-1} and a change of the absorption cross section by 18 % for a carbonyl at a distance of 4 Å from a unit charge and oriented parallel to the electric field. In light of the typical width of carbonyl vibrational bands of 10 - 20 cm^{-1}, these shifts are significant and should be easily detectable. Similar effects were predicted [3.18], [3.21], [3.22] and observed [3.11], [3.23] for free CO and the CO ligand in cytochromes [3.24]. Also changes in the amide-I' band of photosynthetic reaction centres [3.25] and small de novo-peptides [3.26] after charge shifts were in agreement with these predictions

3.3 The Ferrocenophanone/Oxazin-1-System

To show the feasibility of this approach we monitor on the femtosecond time scale the oxidation dynamics of the divalent iron cation in a ferrocenophanone (figure 3.6, [3.27], [3.28]) via the stretch frequency of a spectator carbonyl group, which is located on the bridge connecting the two cyclopentadienyl moieties.

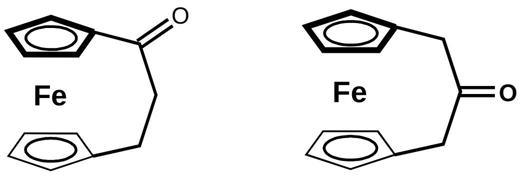

1 **2**

Figure 3.6: Structure of the electron donor ferrocenophanone **1** and ferrocenophanone **2**.

The carbonyl stretching mode of the ferrocenophanones is expected to be affected by changing the charge on the ferrocene unit mainly via the vibrational Stark-effect and thus should provide a good model for the proposed class of electrostatic sensors.

This is true particularly for ferrocenophanone **2**, whose X-ray structural data [3.29] shows the carbonyl π-bonding orbital to be approximately orthogonal to the cyclopentadienyl π-orbitals. With the assumption, that these data referring to the neutral species also are approximately valid for the oxidized species, we can exclude a significant coupling between these orbitals.

3.3.1 Theoretical Calculations

We calculated the electric field changes at the carbonyl group upon oxidation of the ferrocene unit with the help of X-ray structural data. The additional charge was assumed to be evenly distributed over the iron and the cyclopentadienyl rings, [1] as indicated by INDO calculations [3.30] and Moessbauer spectroscopy [3.31].

From the calculated electric field change, a shift of the carbonyl stretching frequency after oxidation of ferrocenophanone **1** by approximately 45 cm^{-1} and a decrease of the cross section on the order of 20 % are predicted [2]. For ferrocenophanone **2**, the carbonyl group is at a slightly larger distance to the ferrocene unit and is oriented at a larger angle to the electric field. Thus, a smaller shift of the carbonyl stretch frequency of 32 cm^{-1} and a decrease of the cross section by 13 % are expected upon oxidation.

These values were compared with chemical oxidation experiments. Oxidation was achieved by treating a deaerated 5 mM solution of **1** or **2** in CH_2Cl_2 with a stoichiometric amount of $AgBF_4$. Formation of the ferrocenium cation was confirmed by its characteristic absorption around 620 nm [3.32] and by the characteristic paramagnetic shifts in the ^{1}H-NMR spectrum.

After this treatment a shift of the carbonyl stretching frequency by 33 cm^{-1} and 27 cm^{-1} was found, respectively (figure 3.7). These values are in reasonable agreement with the expected values. Especially the slightly smaller shift of the carbonyl frequency after oxidation of **2**, as compared to **1**, supports the notion that the shift is dominated by the Stark-effect. In **2** the C=O-bond is oriented at a larger angle to the line connecting iron and carbonyl, thus making it less sensitive to changes of the charge on the iron.

Deviations of the absolute shifts from the predicted values may arise from

---

[1] If all of the charge is assumed to be localized on the iron, the electric field changes at the carbonyl group differ by less than 20 % from those obtained with an even distribution over iron and cyclopentadienyl rings. This uncertainty in the calculated electric field arising form the uncertainty in the exact form of the charge distribution is smaller than the uncertainty arising from the different theoretical methods employed for calculating the tuning rate.

[2] Here the Stark-effect tuning rate and cross section decrease obtained from calculations on formaldehyde were used, since no calculations are available for ferrocene derivatives.

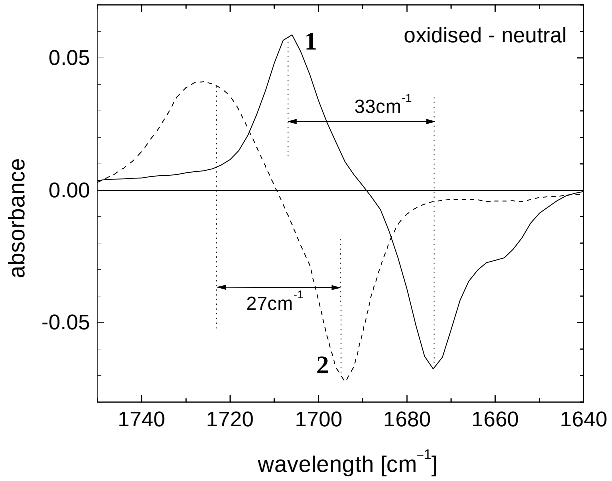

Figure 3.7: Frequency shift of carbonyl bands after chemical oxidation of ferrocenophanone **1** (solid line) and ferrocenophanone **2** (dashed line) in CH_2Cl_2. Infrared spectra were recorded on an FTIR spectrometer (Perkin-Elmer, Series 1600) in a 0.5 mm CaF_2-cuvette. For **2**, the carbonyl band of the neutral and the oxidized form partly overlap, therefore the minimum and maximum of the difference spectrum do not correspond exactly to the positions of the separate bands.

the inadequacy of applying Stark-effect calculations on formaldehyde to observations on more complicated molecules. Further, solvent screening and the fact, that not all of the charge is localized on the iron atom, were neglected. The integrated IR cross section of the carbonyl band is found to be reduced by approx. 20 % for **1** and 15 % for **2** upon oxidation, again in reasonable agreement with the ab-initio predictions.

We can conclude, that the observed changes in the carbonyl stretch vibration upon chemical oxidation of **1** and **2** are dominated by the vibrational Stark-effect, and that the carbonyl stretching frequency is a sensitive sensor for the redox state of **1** and **2**.

3.3.2 Experiments in the Visible

Recently, photoinduced electron transfer from ferrocene derivatives to various acceptor molecules has been observed in fs time-resolved measurements by following transient absorbance changes of the acceptor oxazine-1 in the visible spectral region [3.33] - [3.35]. Because of its small extinction coefficient in the visible region, no spectral response of ferrocene could be detected in these experiments. Thus, the interpretation of the observed signals as arising from electron transfer could be confirmed only indirectly by the observation of an ultrafast magnetic field effect on the recombination dynamics of the photoinduced radical pair due to spin chemical effects [3.34].

The ferrocenophanone **2**, acting as spectator bond in the above sense, should make it possible to directly observe the time dependence of the redox state of the electron donating ferrocene derivative. Then, femtosecond time-resolved IR measurements on the electron donor will complement measurements in the visible spectral region on oxazine-1, the electron acceptor, thus yielding a more comprehensive picture and unambiguously assigning the observed signals to an electron transfer reaction.

The singlet excited state of free oxazine-1 in solution normally decays on the ns time-scale. After excitation of oxazine-1 (10^{-4} M) at 650 nm in the presence of ferrocenophanone **2** at a large concentration (1 M) the following time dependences were measured (figure 3.8, see table 3.2 for fit results):

- Stimulated Emission from the oxazine-1 singlet excited state at 720 nm
- Ground state recovery at 610 nm

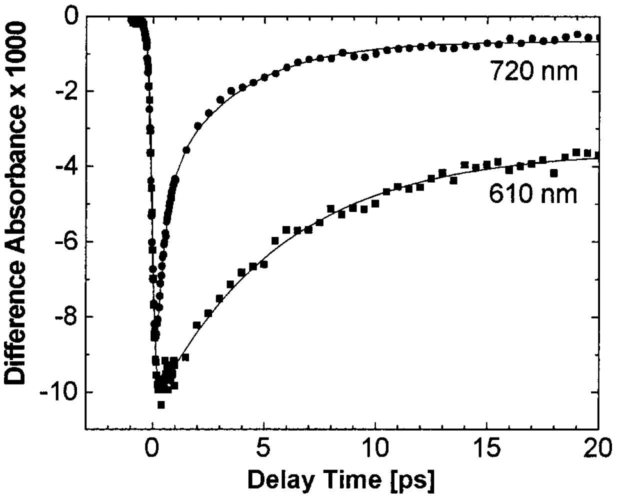

Figure 3.8: Time dependence of the difference absorbance of oxazine-1 (10^{-4} M in CH_2Cl_2) at 720 nm (stimulated emission, circles) and 610 nm (ground state absorbance bleach, squares) after excitation at 650 nm in the presence of ferrocene derivative **2** (1 M). The solid lines are the results of least-squares fits to a multi-exponential decay function with constant background, convoluted with a gaussian instrument response function with a FWHM width of approximately 200 fs. See table 3.2 for fit results.

Wavelength	A_1	τ_1	A_2	τ_2	A_3	τ_3	Offset
720 nm	62 %	370 fs	34 %	3.4 ps	-	-	4 %
610 nm	56 %	5.8 ps	25 %	38 ps	9 %	280 ps	10 %

Table 3.2: Fit results of the least-squares fit in figure 3.8 (solid lines). Data at delay times longer than 20 ps are not shown there, but were included for fitting.

The stimulated emission of oxazine-1 was found to decay with a major fast component with a time constant of 370 fs and a smaller component with 3.4 ps. In a previous study the dependence of the nonexponential quenching dynamics of a photoexcited dye on the concentration of the ferrocene quencher was investigated in detail [3.33].

In accordance with these results, we conclude that the fast component observed here do arise from static quenching in ferrocenophanone/oxazine-1 contact pairs, whereas the slower component reflects quenching of those excited oxazine-1 molecules with no quencher molecule in immediate proximity. The slightly different values for the time constants observed here and in the previous investigation arise from the different ferrocene substituents and solvents used in the two studies.

The ground state recovery of oxazine-1 in the presence of 1 M ferrocene derivative **2** is dominated by a component with a time constant of 5.8 ps, followed by smaller components with 38 and 280 ps. Moreover, the ground state does not recover completely on the accessible time scale of a few ns. The delayed ground state recovery shows that the quenching process leads to the formation of an intermediate state involving oxazine-1 (thus directly ruling out energy transfer as quenching mechanism), which decays in a highly nonexponential way.

Previously, charge transfer from a photoexcited dye to ferrocene has been suggested as the relevant quenching mechanism [3.33]. Compelling evidence for this mechanism was found when a magnetic field effect on the ground state recovery of oxazine-1 was observed on the ps-time scale in the presence of high concentrations of ferrocene [3.34]. The charge transfer yields a singlet-phased radical pair which undergoes (magnetic field dependent) singlet-triplet mixing. The relevant reaction scheme is shown in figure 3.9.

Triplet-phased radical pairs are prevented from recombination to the singlet gorund state, and the nonexponentiality of the oxazine-1 ground state recovery is an immediate consequence of the radical spin dynamics. The recovery is not complete on the picosecond time scale, since some of the radical pairs escape geminate recombination and diffusively recombine on a much

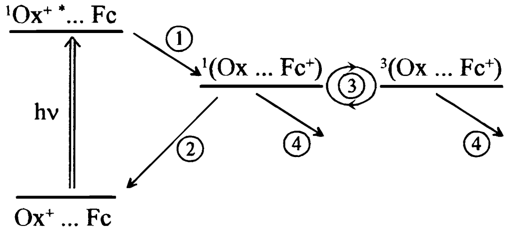

Figure 3.9: Simplified reaction scheme describing the relevant processes occuring after photoexcitation of oxazine-1 (Ox^+) in the prescence of ferrocenophanones (Fc); 1: forward charge transfer; 2: back charge transfer; 3: magnetic field dependent singlet-triplet mixing; 4: cage escape

slower time scale.

3.4 IR Spectroscopy

3.4.1 Steady-state Spectrum

As already mentioned above, the only experimental evidence for charge transfer is the observed magnetic field effect on the ground state recovery of oxazine-1. No direct spectroscopic evidence for charge transfer for the participation of ferrocenophanones in the intermediate state is available from measurements in the visible/near-IR due to its small extinction coefficient. The coefficient lies well below 1000 $M^{-1}cm^{-1}$ and is covered by the much higher extinction coefficient of oxazine-1 of approximately 130 000 $M^{-1}cm^{-1}$. The characteristic vibrational absorption bands in the IR-region now make it possible to directly follow the temporal evolution of ferrocenphanone **2** as electron donor by transient IR spectroscopy.

Figure 3.10 shows the IR spectrum of **2** from 1000 cm^{-1} to 2000 cm^{-1}, recorded on a FTIR-spectrometer (Perkin-Elmer, Series 1600) in a 0.5 mm CaF_2 cuvette.

We can clearly see two broad, intensive bands at 1263 cm^{-1} (= 7.9 μm) and at 1694 cm^{-1} (= 5.9 μm). The former band can be assigned to the carbon bonds (C-C) of the bridge connecting the cyclopentadienyl-rings, whereas the latter is the characteristic feature of the carbonyl group (C=O).

The smaller bands between 1400 and 1500 wavenumbers have their origin in the ring-vibrations of the aromatic cyclopentadienyl-rings, the bands with maxima at 1028 and 1205 wavenumber are contributions of the vibrations of C-H, $C-H_2$ and $C-H_3$.

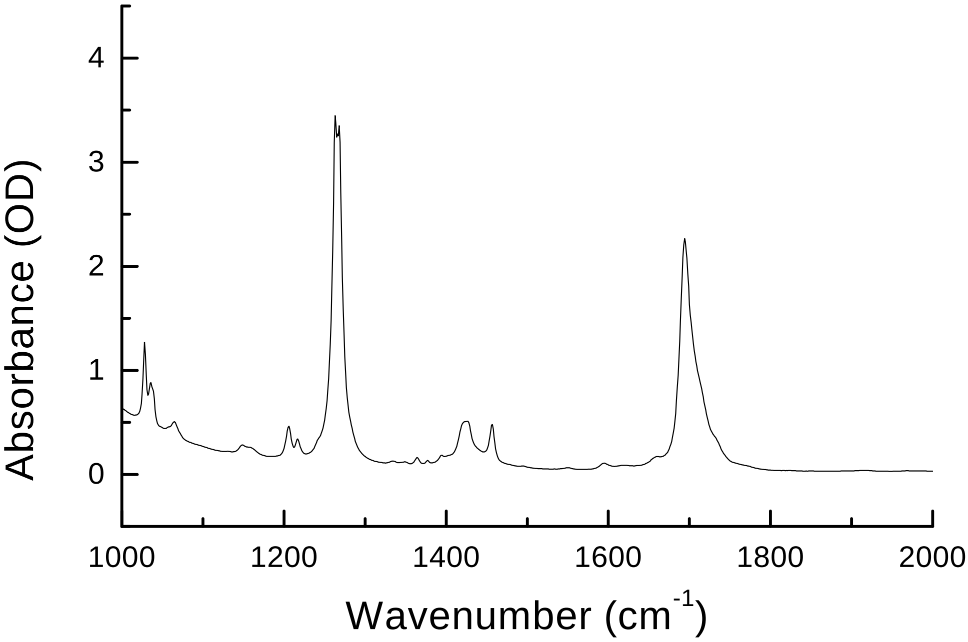

Figure 3.10: IR-spectrum from 1000 to 2000 cm^{-1} of 1 M ferrocenophanone **2** in CH_2Cl_2, optical path length 0.5 mm.

3.4.2 Materials and Methods

Ferrocenophanone **2** was prepared following published methods [3.27], [3.28], oxazine-1 (Lambda Physik) and methylene-chloride (UVASOL, Merck) were used as supplied.

All fs time-resolved absorption measurements were performed on the laser-system described in chapter 2.2. Pump-probe geometry and detection scheme for measuring transient absorption changes in the IR were essentially the same as employed for measurements in the visible. Probe pulses were focused on the excited sample volume under a small angle to the excitation beam.

Excitation wavelength at 650 nm with 150 fs time resolution was generated by collinear three-wave-mixing of the frequency-doubled laser-output in the two-step collinear OPG/OPA setup described in section 2.3.4.

The generation of IR probe pulses tunable in the 1650 - 1750 cm^{-1} range with a spectral resolution of 3 cm^{-1} was achieved by a second two-step OPG/OPA setup illustrated in section 2.3.5.

In all time-resolved measurements, the concentration of ferrocenophanone **2** in methylene-chloride was kept at 1 M to ensure rapid quenching of photoexcited oxazine-1. The concentration of oxazine-1 and the optical path length were 10^{-4} M/1 mm and 2×10^{-3} M /57 μm, respectively.

3.4.3 Transient Spectrum

Transient absorbance changes were measured by chopping the pump light at 500 Hz to block every second excitation pulse. Each transient absorbance value was then normalized to the separately measured excitation pulse energies to eliminate the effects of fluctuating energy. Transient difference absorbance values with a resolution of 0.1 mOD were detectable after averaging over 1000 normalized measurements.

The transient difference absorption spectrum of ferrocene derivative **2** in the carbonyl region measured at a delay time of 1 ps after excitation of oxazine-1 is shown in figure 3.11.

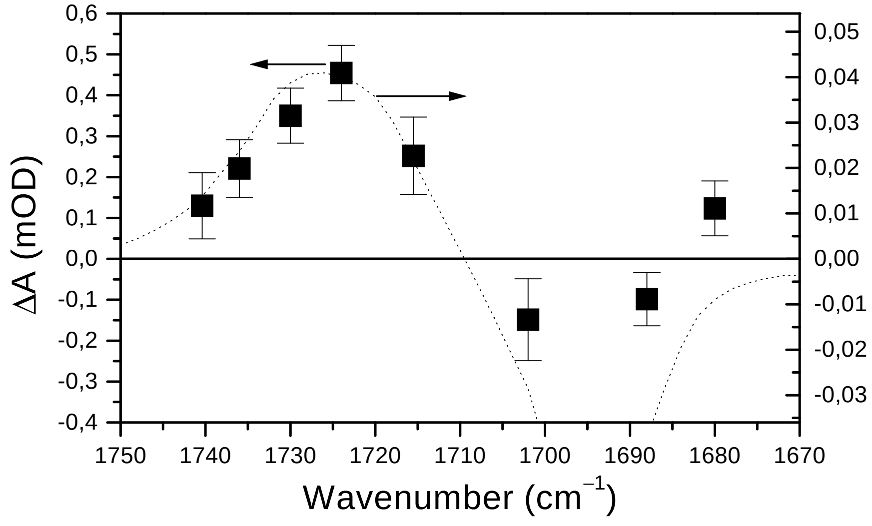

Figure 3.11: Time resolved difference absorption spectrum (squares, left ordinate) of ferrocene derivative **2** (1 M in CH_2Cl_2) at a delay time of 1 ps after excitation of oxazine-1 (2×10^{-3} M) at 650 nm. Also shown is the static difference absorbance spectrum (chemically oxidized - neutral, dashed line, right ordinate)

As shown, the transient absorption spectrum agrees well with the static difference absorbance spectrum between the chemically oxidized and neutral ferrocene derivative **2**. Thus, the intermediate state, which is formed upon quenching of excited oxazine-1 with a dominant time constant of 370 fs and decays with a dominant time constant of 5.8 ps, is shown to involve an oxidized ferrocene moiety. This constitutes the first direct spectral evidence of fast electron transfer from a ferrocene derivative to an excited electron acceptor.

Because of the strong absorbance of the sample around 1695 cm^{-1}, it was not possible to accurately measure the absorbance bleach near the maximum of the vibrational band. However, the minor deviations of the time-resolved and static difference spectra for wavenumbers below 1690 cm^{-1} are significant and reproducible. They may arise from carbonyl groups on neighbouring ferrocenophanone molecules which are not directly involved in the charge transfer but are close enough to the reacting molecules to feel the ensuing electric field changes.

Due to the high concentration of ferrocenophanone, which is needed to ensure ultrafast static quenching of oxazine-1 on the femtosecond time scale, there is a significant probability of several ferrocenophanone molecules being near each oxazine-1 molecule. The random orientation of their carbonyl groups with respect to the reacting molecules should lead to an overall broadening of the carbonyl band upon charge transfer, which could well explain the observed deviations. Alternatively, the deviations may be due to coupling of the electron transfer to the carbonyl stretch, resulting in the excitation of higher vibrationally excited states, whose absorbance is anharmonically shifted to lower frequencies. More detailed measurements are needed to identify the origin of these deviations.

3.4.4 Time-resolved Data

The time dependence of the transient absorbance at 1724 cm^{-1}, figure 3.12, mirrors the concentration of oxidized ferrocene derivative **2**. The observed IR signal is fully compatible with the dynamics observed in the visible region.

This is shown by the solid line in figure 3.12, which represents the results of a nonlinear least-squares fit of the IR data based on the time constants of the fastest components for forward and reverse charge transfer, as determined form the data in the visible region. Here we refrained from including in the fit the minor kinetic components observed in the visible because of the significant noise of the IR data obtained with the current experimental set-up.

Furthermore, a thorough analysis will have to take into account coherent contributions to the observed signal, [3.36], [3.37] since the carbonyl vibrational transition has a dephasing time on the order of 1 ps. Again the significant noise in the present data made such an analysis unfeasible. Further technical improvements, which will allow measurements with significantly improved signal-to-noise ratio, are currently in preparation in our lab.

3.4.5 Discussion

Measurements in the visible allow the determination of forward and backward charge transfer dynamics only from measurements at several wavelengths: Forward charge transfer dynamics are observable in the stimulated emission

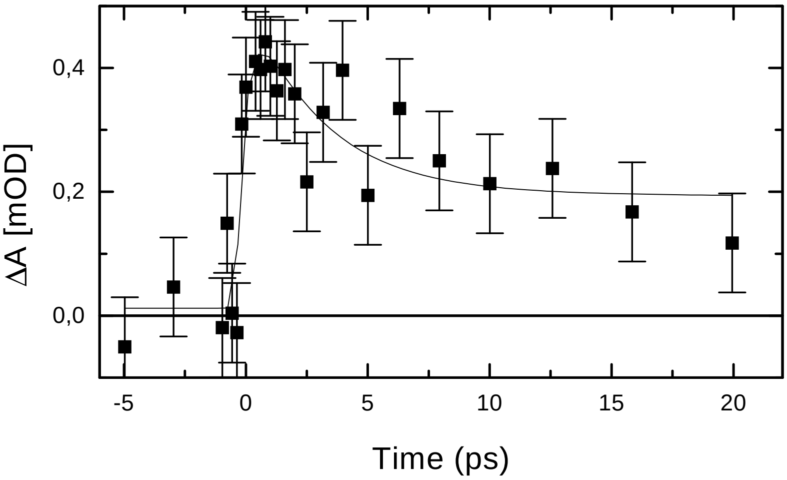

Figure 3.12: Time dependence of the difference absorption of ferrocene derivative **2** (1 M in CH_2Cl_2) at 1724 cm^{-1} after excitation of oxazine-1 (1×10^{-3} M) at 650 nm. The solid line is the result of a least-squares fit with fixed time constant $\tau_1 = 0.37$ ps (rise) and $\tau_2 = 5.8$ ps (decay), as determined from measurements in the visible spectral region, and a constant, representing slower decay components, convoluted with the experimental response function, represented by a gaussian with a width of 200 fs.

of photoexcited oxazine-1, whereas backward charge transfer dynamics can be determined only from measurements of the ground state recovery. The IR signal, on the other hand, is a direct measure of the concentration of ferrocenophanone in the oxidized state and thus has the advantage of allowing the direct observation of both processes in one measurement.

Thus, charge transfer dynamics can be well monitored in the infrared. As shown here, this may allow one to obtain a more comprehensive picture of a redox process by observing both partners separately. However, infrared spectroscopy will be even more useful for the investigation of redox systems where both partners have no suitable absorbance bands in the visible spectral region, in particular, redox systems involving small molecules.

The vibrational Stark effect is sensitive to changes of the electric field alone and allows one to monitor changes of the electron density *from a distance.* Therefore, the sensor group does not need to be part of the molecules involved in the reaction, but may be located in the immediate surroundings.

Measurable Stark shifts can be expected as long as the spectator group is within a maximum distance from the reacting system, which can be estimated from the Stark tuning rate. Typical Stark tuning rates for carbonyls are on the order of 5×10^{-7} $cm^{-1}/(V/cm^{-1})$, implying a maximum distance of 6 - 7

Å, at which the shift becomes comparable to the width of the carbonyl band.

3.5 Conclusions

The feasibility of using the vibrational Stark effect for the observation of charge transfer reactions on a short time scale was demonstrated. The photoinduced oxidation of ferrocenophanone induces a fast shift of the carbonyl stretching frequency which is observable by femtosecond time-resolved IR spectroscopy.

For the redox system investigated here, it was shown unambiguously that electron transfer is the dominating quenching process of photoexcited oxazine-1 in the presence of ferrocenes. The observed shift is in good agreement with the IR spectrum of chemically oxidized ferrocenophanone and with theoretical predictions based on vibrational Stark-effect calculations. The time dependence of the signal mirrors the charge transfer dynamics on the fs to ps time scale, as observed by optical spectroscopy.

The carbonyl frequency shift upon changing the ferrocene charge is dominated by the vibrational Stark effect. Since the carbonyl sensor is sensitive to electric field changes alone, the method can be extended to systems where the spectator bond is not part of one of the participating molecules, but is integrated in the environment of the redox system under investigation.

This might be of particular interest in organized environments and supramolecular structures; for example, one may use the carbonyls already present in proteins or DNA/PNA for following electron or proton transfer reactions in biomolecules.

Chapter 4

Dye Sensitized TiO_2-Colloids

4.1 Dye sensitizer for electrochemical cells

Photovoltaic cells based on silicon are well known and are extensively used for transformation of solar energy in electricity (solar cells). However, the use of existing commercial devices is still expensive and has a rather low efficiency. The search for new techniques for photoconversion devices focuses on photoelectrochemical cells (see for example [4.1]).

In these cells the solar light response of wide band semiconductors such as SnO_2 [4.2], ZnO [4.3] or TiO_2 [4.4] is achieved by dye sensitization. Because of their large band-gap, semiconductors normally have their absorbance bands in the UV ($\lambda < 400$ nm) and are transparent in the visible. When dye molecules are adsorbed on the surface of semiconductor nanoparticles or films, the absorption of solar photons excites the dye in a state above the conduction band edge and triggers interfacial electron transfer [4.5].

The transfer reaction can be the initial step in a photochemical reaction chain, which were already studied for the past two decades (for example, carrier capture by surface states, carrier recombination, carrier transfer to/from adsorbed dye molecules, etc.). However, the study of their *dynamical* properties is relatively new [4.6]. Current investigation in the topic of dye sensitized nanocrystalline semiconductors are also motivated by the large number of other practical applications, such as wastewater treatment [4.7] and nanoelectric devices [4.8].

An important approach in this direction is the "Graetzel-type" photoelectric cell [1.10] and related devices [4.9]. These cells differ from conventional semiconductor solar cells in that they separate the function of light harvesting from charge transport. In the case of TiO_2 nanoparticles (which is a n-type semiconductor) current is generated, when a photon absorbed by a dye molecule (D) gives rise to electron injection into the conduction band of the semiconductor and can migrate to the collecting electrode. Recombination (or back electron transfer) of the electrons with the dye cation D^+ can limit the efficiency of the cell. To minimize these losses and to close the circuit, the dye must be regenerated by electron transfer from a redox species or electrolyte (for example I^-/I_3^-) in the solution, which is further reduced at a counter electrode. The following scheme shows the individual reaction steps:

$$\begin{aligned}
D + TiO_2 &\overset{h\nu}{\longrightarrow} D^* + TiO_2 \\
D^* + TiO_2 &\overset{injection}{\longrightarrow} D^+ + [TiO_2 + e_{cb}] \\
D^+ + [TiO_2 + e_{cb}] &\overset{Recomb.}{\longrightarrow} D + TiO_2 \qquad \textbf{or:} \\
D^+ + I^-/I_3^- + [TiO_2 + e_{cb}] &\overset{Reduction}{\longrightarrow} D + TiO_2 + I^-/I_3^- + I_{cur}
\end{aligned} \tag{4.1}$$

Here, e_{cb} means an electron in the conduction band, I^-/I_3^- is taken as the electrolyte and I_{cur} is the resulting photocurrent at the electrode.

A typical dye monolayer adsorbed on a semiconductor surface can only absorb about 2 % of the incident light. The sponge-like TiO$_2$ colloidal particles offer a much bigger surface for dye adsorption. In fact, the very high surface-to-volume ratio provides a high number of adsorbed dye molecules per unit volume of semiconductor [4.5].

Moreover, because of the large band-gap (approximately 3.2 eV in TiO$_2$ anatase), they are optically transparent in the visible region. Thus, the excitation energy is exclusively absorbed at the dye/semiconductor interface for an efficient electron injection. One obtains an optically thick layer even at low dye concentrations. Figure 4.1 illustrates the reaction scheme.

The efficiency of the electron injection (k_{inj}) from the excited state of the dye (D*) to the continous states of the conduction band of the semiconductor is determinded by the competition of the injection rate with other decay rates. The existence of these loss channels (for example internal conversion (k_{IC}) to the ground state or fluorescence (k_F)) requires electron injection times on the sub-nanosecond time scale [4.10], [4.11]. Indeed, suitable sensitizer dyes show injection time constants down to the femtosecond time scale (see for example [4.6](c),(d), [4.11](b),(c), [4.12]), due to the very strong electronic coupling to the conduction band states of the semiconductor.

Because of the high surface-to-volume ratio, the surface trap states play an important role in the injection process which was explicitely shown by investigations on alizarin adsorbed on the high band-gap material ZrO$_2$ [4.13].

The high density of acceptor states (conduction band and lower lying surface trap states) ensures an optimal nuclear overlap as long as the ex-

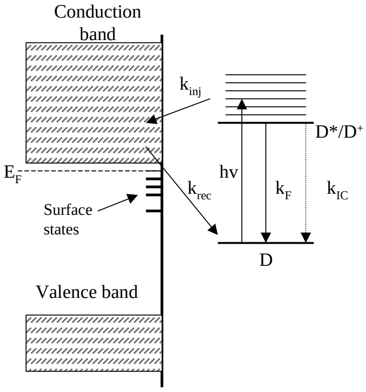

Figure 4.1: Reaction scheme for dye sensitized TiO_2-colloids. The sensitizer dye D is photoexcited (D*). Then an electron is injected (k_{inj}; thereby oxidising the dye D^+) with a transfer rate faster than the rates of competing processes like fluorescence (k_F) or non-radiative internal conversions (k_{IC})). The recombination (k_{rec}) occurs on a slower time scale.

cited sensitizer state lies above the conduction band edge by more than the reorganization energy.

Back electron transfer to the sensitizer dye in these systems is not well understood yet. The recombination dynamics of the cation and the injected electron has been shown to range from picoseconds [4.13], [4.14], [4.15], [4.16] and nanoseconds [4.10](c), [4.14], [4.17] up to microseconds and even milliseconds [4.18], depending on the dye/semiconductor system. This is up to 10 orders of magnitude slower than the injection process.

Such a big difference between both processes cannot be explained by the large band-gap alone. It is widely assumed that the surface states also play an important role both as electron traps and intermediate states for the interfacial charge transfer (see for example [4.19]).

In the following, some photophysical and recombination properties of the dye molecule merocyanine-3 (Mc3) will be investigated, which might be interesting for its use as photosensitizer of TiO_2 in photoelectrochemical cells.

Merocyanines are used in photography as efficient photosensitizers [4.20], especially on silver halide films [4.21]. They have been thoroughly studied in the field of the dye multilayer photovolatic cells based on a Schottky-type barrier at the metal/dye film contact [4.22], but the efficiency is very low, because charge separation mainly takes place only at the metal/dye interface and the charge transfer through the dye multilayer is not efficient.

Evaporated merocyanine dye layers have attracted much attention in the field of solar energy conversion [4.23]. Until now, merocynanines have been rarely investigated as sensitizers for the Graetzel-type cells, but recent studies with benzothiazole types seem promising [4.24].

As it should be clear from the introduction given above, the conversion efficiency of the dye sensitized cell depends strongly on the rates of both the charge injection and the recombination. A fast charge injection will reduce the undesired influences of competing processes (like energy transfer or other dye-dye interactions), whereas the recombination rate should be as slow as possible. In this case, back electron transfer (which will reduce efficiency) can be prevented by reducing the dye cations by a suitable electrolyte (for example I^-/I_3^-).

As we are mainly interested in the latter process, we performed nanosecond time resolved pump probe measurements on the recombination kinetics.

Another aim of this work is the search for possible triplet signals and magnetic field effects on the recombination signal. The electron transfer from the dye molecule (donor) to semiconductor nanoparticle (acceptor) generates a radical pair, this means both reaction partners have an unpaired electron. Such a system is expected to undergo spin dependent recombination dynamics including a magnetic field dependent singlet-triplet mixing in particular when the time scale of recombination is slower than S-T mixing and when T_2-type spin-spin relaxation is slow. Therefore low temperature conditions may be useful.

4.2 Materials and Methods

All laser dye solutions (Lambdachrome, Lambda Physik GmbH, Goettingen or Radiant Dyes GmbH, Wermelskirchen) were prepared according to specifications of the supplier [4.25]. Solvents (Sigma Aldrich, spectrophotometric grade or Merck, UVASOL for spectroscopy) were used as supplied without further purification.

Excitation wavelengths between 530 nm and 550 nm are generated with Coumarin 307 (0.4 g/l in Methanol). Excitation wavelengths between 560 nm and 580 nm are generated with Rhodamine 19 (0.22 g/l in Methanol) or Rhodamine 6G (0.12 g/l in Methanol) pumped with the second harmonic of the Nd:YAG laser.

Probe wavelengths between 510 nm and 580 nm are produced by pumping Coumarin 153 (3.1 g/l in Methanol) with the nitrogen laser.

Merocyanine-3 (Mc3, figure 4.2, violet, crystalline powder) and TiO$_2$-colloids (10 g/l, anatase crystals with typical Ti-Ti distances of ≈ 3 Å [4.26]) in aqueous solution were supplied by Moser, J. E. (Swiss Federal Institute of Technology, Lausanne, CH) and stored in a refrigerator (3 - 5 °C).

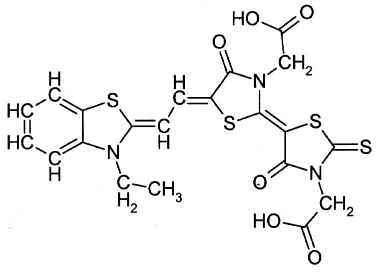

Figure 4.2: Molecular structure of Merocyanine-3, synthesized especially for its use as photosensitizer of TiO_2 nanoparticles.

This dye molecule was synthesized for the use in photoelectrochemical cells. In order to shift the typical absorption of merocyanines further to the red, a second benzothiazol ring is added.

In a first step the optical properties of the pure dye in solution at both room temperature and low temperatures (down to 100 K) are investigated. These results will serve as a reference when we go to the more complex case where the dye is adsorbed on the TiO_2-nanoparticles.

4.3 Pure Dye in Solution

Mc3 is neutral and soluble in ethanol up to ca. 10^{-4} M, but not well soluble in pure water. In order to improve adsorption of the dye onto the TiO_2 nanoparticles, TiO_2 colloids based on water/ethanol mixtures with high water content were used.

Because it was reported that similar dye molecules can form aggregates (for example dimers) in such mixed solvents [4.27], we first studied the effect of different water/ethanol ratios on the pure dye in solution.

Therefore, we first recorded steady-state absorbance spectra for different water/ethanol ratios (figure 4.3, dye concentration 1.2×10^{-5}).

The absorbance maximum is red shifted from 561 nm in pure ethanol to 592 nm in the 4:1 water/ethanol mixture because of the increasing polarity of the solvent (bathochromic shift or positive solvatochromism). In pure water the band shape changes and two peaks at 558 nm and 592 appear. The new blue shifted band in the spectrum can result from dimer formation.

The emission maximum also shifts to the red from 604 nm in pure ethanol to 620 nm in 4:1 water/ethanol (not shown).

Employing second order perturbation theory [4.28], one can get a relation between the dipole moments of the ground state and the excited state by the

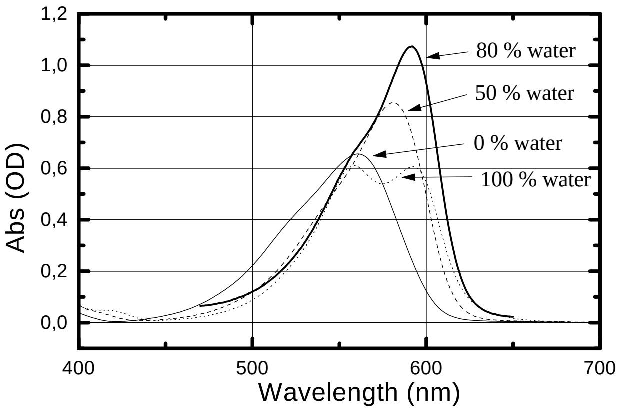

Figure 4.3: Steady-state absorption spectra of Mc3 (1.2×10^{-5} mol/l) in different water/ethanol solvents. Thin solid line: pure ethanol; dashed line: water/ethanol = 1:1; thick solid line: water/ethanol = 4:1; dotted line: pure water

following equation:

$$\Delta\nu = \text{dispersion term} + B\frac{n^2-1}{2n^2+1} + C\left(\frac{\epsilon-1}{\epsilon+2} - \frac{n^2-1}{n^2+2}\right) + \text{Stark effect} \quad (4.2)$$

where ϵ and n is the dielectric permittivity and the refractive index of the solvent, respectively, and B and C involve the molecular volume of the solute molecule and its dipole moment in the electronic ground and excited state.

The first term due to dispersion effects accounts for the effect of non-polar solvents on non-polar solutes. The second term represents the contribution from the interaction of the solute permanent dipoles with the solute induced solvent dipoles. The third term represents the interaction between permanent solute and solvent dipoles.

Assuming the Stark effect term to be negligible, equation can be simplified to study the effect of ϵ alone for two polar solvents of nearly the same refractive index [4.29] which is the case for water (n = 1.333) and ethanol (n = 1.361).

The wavelength of the band maximum is plotted versus $\frac{\epsilon-1}{\epsilon+2}$ taking ϵ as the arithmetic average of water ($\epsilon = 78.3$) and ethanol ($\epsilon = 24.55$). From the slope of a linear fit (with pure water as solvent excluded because of dimers), the constant C can be derived

$$C = (2\pi\epsilon_0 hc)^{-1}(\mu_g\mu_e cos\phi - \mu_g^2)/a_w^3 \quad (4.3)$$

μ_g and μ_e is the permanent dipole moment of the ground state and excited state, respectively, ϕ the angle between the dipole of the ground state and excited state and a_w is the cavity radius of the solute in the solvent.

C is negative ($\mu_e > \mu_g$) and we obtain

$$(\mu_g \mu_e cos\phi - \mu_g^2) = (0.97 \pm 0.18) a_w^3 \quad D^2 \tag{4.4}$$

with a_w in [Å] and 1 D = 1 Debye = 3.336×10^{-30} Cm

Using the same assumptions as before, a similar expression for the shift of the emission wavelength can be derived [4.30].

$$\nu_A - \nu_E = (2\pi\epsilon_0 hc)^{-1}(\mu_e^2 - \mu_g^2)/a_w^3 \left(\frac{\epsilon - 1)}{2\epsilon + 1} - \frac{n^2 - 1}{2n^2 + 1}\right) \tag{4.5}$$

where ν_A and ν_E are the band maxima of the absorption and emission bands. Application of a linear fit to the $\nu_A - \nu_E$ versus $\frac{\epsilon-1}{2\epsilon+1}$ plot gives:

$$(\mu_e^2 - \mu_g^2) = (1.81 \pm 0.38) a_w^3 \quad D^2 \tag{4.6}$$

These equation are far from being exact. Nevertheless, they are a rough estimate for the four parameters (μ_g, μ_e, ϕ, a_w) which are solute dependent but not available at present.

From the absence of the second band at low water concentrations we can assume, that the vast majority of the dye molecules are still in the monomeric form. To check the aggregation hypothesis, we investigated the concentration dependence of the spectra.

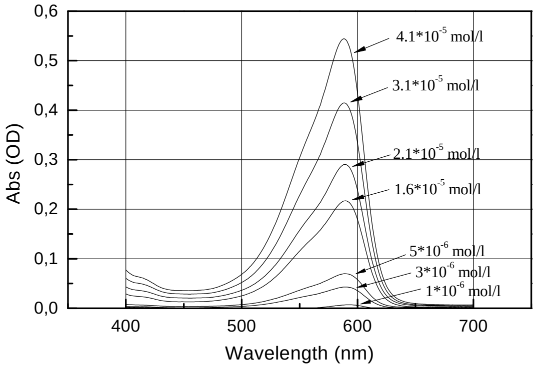

Figure 4.4: Steady-state absorption spectra of different Mc3 concentrations in a water/ethanol = 4:1 solvent. The concentration is increased from 1×10^{-6} mol/l to 4.1×10^{-5} mol/l. When normalized to the spectrum for 4.1×10^{-5} mol/l (taken as reference) the curves are identical.

The dye concentration was increased from 1×10^{-6} mol/l to 4.1×10^{-5} mol/l. No significant concentration dependence of the band shape was observed (figure 4.4). At dye concentrations higher than 5×10^{-5} mol/l a blue shifted shoulder at 558 nm began to develop.

We used the water/ethanol = 80 %/20 % mixture as solvent. In this solvent the steady-state fluorescence (excitation at 590, not shown) is the mirror image of the absorption with the maximum at 620 nm and a shoulder around 650 nm. The excitation scan (emission wavelength 620 nm) has the same shape as the absorption spectrum.

Because the pH value will be changed by addition of TiO_2 particles and glycerol (added as glass maker in low temperature measurements), we investigated the pH-dependence in absence of TiO_2. Figure 4.5 shows a steady-state absorption measurement for 1×10^{-5} mol/l Mc3 in the 80 % water/20 % ethanol solvent for pH values of 2.35, 3.5 and 6.6, respectively.

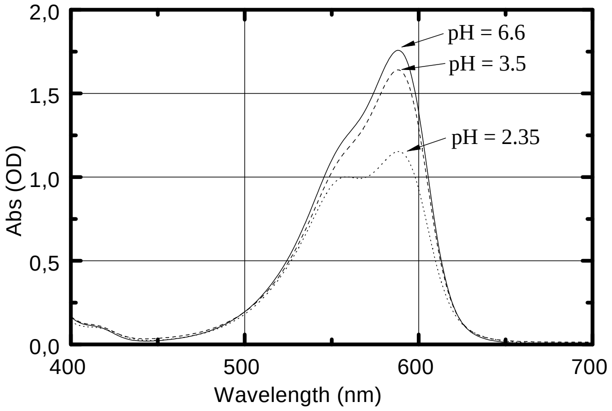

Figure 4.5: Steady-state absorption spectra of Mc3 (1×10^{-5} mol/l) in water/ethanol = 4:1 solvent at different pH-values. Solid line: pH = 6.6, dashed line: pH = 3.5, dotted line: pH = 2.35

While the absorbance band did not change significantly between pH 3.5 and pH 6.6, the blue shifted band at low pH seems to indicate an increased aggregation.

When glycerol is added (solvent composition water/ethanol/glycerol = 32 %/8 %/60 %), the absorption maximum of the Mc3 dye is only slightly blue shifted by 4 nm to 588 nm without change of the band shape. This is a consequence of the lower polarity of glycerol, and is consistent with figure 4.3, where we observed a blue shift with decreasing polarity of the solvent.

When the temperature was lowered (down to 100 K), the formation of dimers was observed. Figure 4.6 illustrates the simultanous growing of the dimeric band (peak at 558 nm at 100 K) and decreasing of the monomeric band (peak at 591 nm at 100 K) with decreasing temperature from 280 K to 220 K. Spectra below 220 K were identical to the spectrum recorded at 100 K, whereas spectra above 280 K showed the monomeric peak only. An

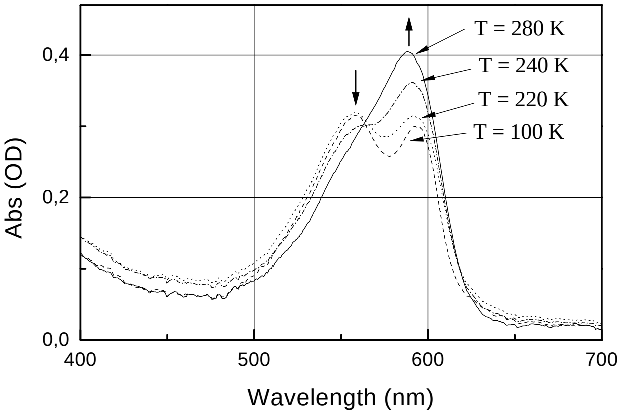

Figure 4.6: Steady-state absorption spectra of 4×10^{-5} mol/l Mc3 in a 32 % water/8 % ethanol/60 % glycerol solvent at different temperatures: Dashed line: at 100 K; dotted line: at 220 K; dash dotted line: at 240 K; Solid line: at 280 K.

isosbestic point is clearly seen at 564 nm.

Moreover, the amplitude of the blue shifted band is concentration dependent which further supports the assignment of dimers. This points to a situation where the frozen dye molecules below 240 K arrange in a mixture of monomers and dimers. Aggregates with more than two molecules involved would lead to an even bigger band shift and can be ruled out for the free dye in solution.

To get an estimate for the reaction enthalphy we fitted the absorption spectra with a least-squares fit with two gaussians functions. The amplitudes obtained for the dimeric band A_D and for the monomeric band A_M are proportional to the concentration of monomers and dimers, respectively. The equilibrium constant K_{eq} (the ratio of concentrations of monomer and dimer) has an Arrhenius type temperature dependence.

$$K_{eq} = \frac{[Dimer]}{[Monomer]} = \frac{A_D}{A_M} = Aexp(-\Delta G_{reaction}/RT) \tag{4.7}$$

A linear fit of the natural logarithm $ln\left[\frac{A_D}{A_M}\right]$ versus 1/T gives a reaction enthalpy of 4.56 ± 0.55 kJ/mol and a pre-exponential factor A = 0.125 ± 0.033.

In this respect a light induced effect should be mentioned. When freezing the dye under additional illumination (luminescence lamp, 10 W), the steady-state absorption spectra at low temperature slightly changed (see figure 4.7 for T = 100 K). In addition to a small decrease in intensity, the spectrum shifted to the red by 4 nm and the dimer band decreased with respect to the monomeric band.

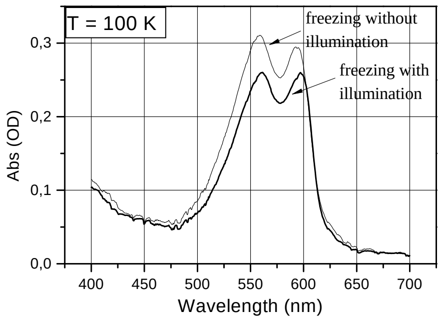

Figure 4.7: Steady-state absorption spectra of 4×10^{-5} mol/l Mc3 in a 32 % water/8 %ethanol/60 % glycerol solvent at 100 K. Thin solid line: Absorption spectrum after freezing without illumination; Thick solid line: Absorption spectrum after freezing with illumination.

All spectra above 220 K were identical to the spectra obtained without illumination. As a consequence the isosbestic point at 564 nm disappeared. This indicates that a part of the dimers are dissociated just by illumination.

Before starting with the $Mc3/TiO_2$ system, steady-state emission and excitation spectra for T = 100 K are given for completeness.

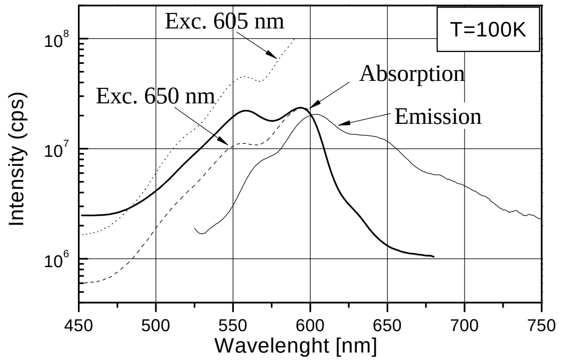

Figure 4.8: Steady-state absorption spectra of 5×10^{-6} mol/l Mc3 in a 32 % water/8 %ethanol/60 % glycerol solvent at 100 K. Thick solid line: Absorption spectrum normalized to emission; Thin solid line: Emission spectrum with excitation at 500 nm; Dotted line: Excitation spectrum of the emission at 605 nm; Dashed line; Excitation spectrum of the emission at 650 nm

Figure 4.8 shows the emission (thin solid line, excitation at 500 nm) and excitation spectra of the emission at 605 nm (dotted line) and at 650 nm (dashed line) at 100 K.

The excitation spectra of the emission at 605 nm and 650 nm shows two distinct bands at the same wavelength as the absorption spectrum, but the blue band has a somehow lower peak at 558 nm indicating a less efficient fluorescence yield which is commonly observed for dimers.

4.4 Mc3 adsorbed on TiO$_2$

Mc3/TiO$_2$ solutions were prepared by mixing the aqueous TiO$_2$ colloidal solution with the required amount of the ethanolic dye solution in a 2 mm plastic cuvette under nitrogen atmosphere in a glove box. In order for the dye to be quantitatively adsorbed onto the oxide surface, its concentration did not exceed 5 μmol per g TiO$_2$. With a mean TiO$_2$-particle radius of 7.5 nm [4.31] this corresponds to approximately 20.7 dye molecules per solid particle and a 6 % surface coverage.

The dye/colliod system was studied for dye concentration effects, because acidic aqueous media and high dye concentrations ($> 10^{-5}$ mol/l for 1 g/l TiO$_2$) can lead to higher order aggregations on the colloid surface with more than two dye molecules involved (see [4.32] for investigations on a similar dye, Mc2).

Such aggregations are formed mainly in water mixtures by hydrophobic interactions and are characterized by close packing of the chromophores and strong electronic coupling [4.33]. These interactions result in a exciton band splitting mostly with one allowed and one forbidden transition depending on the molecular orientation [4.34]. In principle, two types of aggregates are possible:

H-aggregates have their transition dipole moments parallel to each other. In this geometry optical transitions are only allowed to the upper excited singlet state produced by exciton coupling [4.34]. This leads to a band which is blue shifted with respect to the monomeric spectrum. The decay to the lower excited singlet state is normally much faster than fluorescence to the ground state. Subsequent emission from the lower state is very weak due to the forbidden transition.

The other type of aggregate is J-aggregation [4.35] (named after one of its discoverers Jelly [4.35](a)), where transition is only allowed to the lower excited singlet state which results in an intense band with a red shift (up to 50 - 100 nm in cyanine dyes [4.36]). Generally, emission occurs at almost the same wavelength as the absorption (resonant flouresence, [4.37]). Such aggregates can be regarded as two-dimensional crystals with a brickstone arrangement of the chromophores [4.38].

The shift in the absorption spectrum is dependent on the coupling but only weakly proportional to the aggregate dimension. This is due to the fact that every dye molecule mainly interacts with its two nearest neighbours whereas interactions with more distant dye molecules are not important.

4.4.1 Steady-State Absorption

When TiO_2 is added (8 g/l), the absorption spectrum changed dramatically with respect to the pure dye in solution (see figure 4.9).

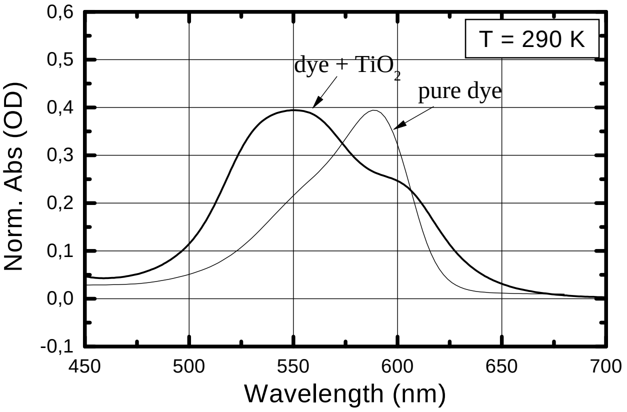

Figure 4.9: Normalized steady-state absorption spectra of 4×10^{-5} mol/l Mc3 in a 4:1 water/ethanol solvent (thin solid line) and in presence of 8 g/l TiO_2 nanoparticles (thick solid line) at room temperature (290 K).

We see a broad band with a peak at 550 nm and a shoulder around 600 nm slightly red shifted compared to the absorption maximum of the monomer in absence of TiO_2.

Obviously, the presence of TiO_2 particles gives rise to a aggregation of the dye molecules.

To check this assumption, we investigated the concentration dependence of the absorption spectrum. Figure 4.10 shows the steady-state absorption spectrum of 8 g/l TiO_2 nanoparticles in a 4:1 water/ethanol solvent with increasing Mc3 concentration.

At *low dye concentrations* (1.5×10^{-6} mol/l (a) to 3×10^{-6} mol/l (b)) we can see two bands with peaks at 570 nm and 603 nm. The monomeric band matches the spectrum of the pure dye at low temperatures (see thick solid line in figure 4.8) except for a red shift of 11 nm. Such a red shift is

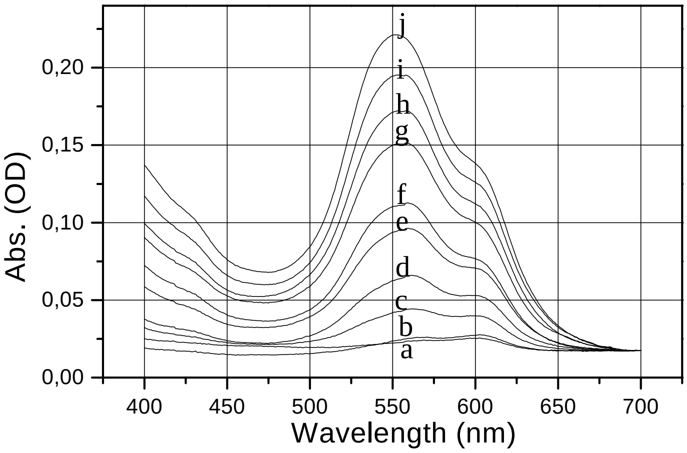

Figure 4.10: Steady-state absorption spectra of 8 g/l TiO$_2$ nanoparticles in a 4:1 water/ethanol solvent with different Mc3 concentrations. (a) 1.5×10^{-6} mol/l (b) 3×10^{-6} mol/l (c) 6×10^{-6} mol/l (d) 12×10^{-6} mol/l (e) 18×10^{-6} mol/l (f) 24×10^{-6} mol/l (g) 30×10^{-6} mol/l (h) 36×10^{-6} mol/l. (i) 42×10^{-6} mol/l (h) 54×10^{-6} mol/l.

commonly observed for sensitizer dyes on surfaces [4.39] and is due due to an interaction with the TiO$_2$ surface.

At *higher dye concentrations* an additional blue band grows with the dye concentration with its maximum shifting down to 550 nm (54×10^{-6} mol/l (j)).

In another steady-state measurement at lower TiO$_2$ concentration (1 g/l TiO$_2$) we observed similar spectra for similar Mc3 to TiO$_2$ ratios (not shown). The two peaks at 570 nm and 603 nm already were present at a concentration of 0.2×10^{-6} mol Mc3 per g TiO$_2$. This is approximately the same ratio as the previous 1.5×10^{-6} mol Mc3 per 8 g TiO$_2$ ratio. H-aggregation again developed with increasing dye concentration.

Since aggregation was not observed in absence of TiO$_2$ at room temperature, the presence of such a high amount of aggregates rather points to a cooperative effect of dye-dye and dye-surface interactions allowing for aggregation. One can imagine that ordering or alignement effects of the surface may be crucial for aggregation.

4.4.2 Steady-State Fluorescence

The steady-state fluorescence in presence of TiO$_2$ is strongly quenched (thick solid line in figure 4.11, magnified by 100; thin solid line is dye without TiO$_2$

as reference), as expected if fast injection to TiO_2 occurs. The remaining fluorescence shows the same maximum around 620 nm as the free dye in solution. Moreover, the shape of the emission band was the same for different excitation wavelengths (500, 590, 605, 610 and 650 nm, not shown).

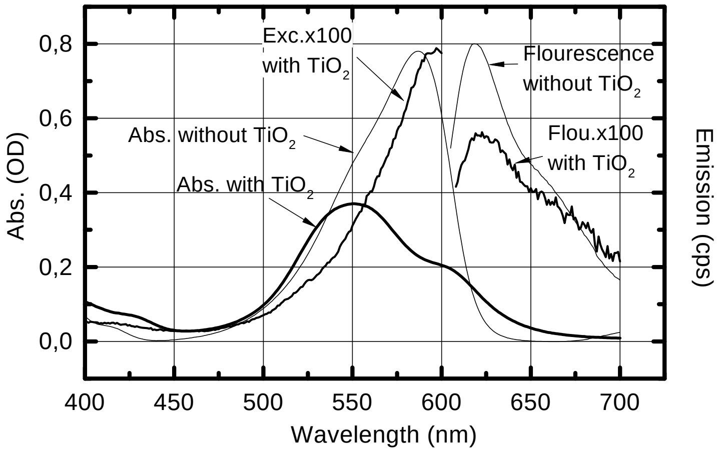

Figure 4.11: Steady-state spectra of 4×10^{-5} mol/l Mc3 in a 4:1 water/ethanol solvent. Thin solid lines: Absorption and fluorescence spectra without TiO_2. Thick solid line: Absorption spectrum in presence of 8 g/l TiO_2. Thick solid lines magnified by 100: Excitation (fluorescence at 620 nm) and emission spectra (excitation at 590 nm) in the presence of 8 g/l TiO_2

The shape of the excitation spectrum (emisssion at 620 nm, magnified by 100) is different from the absorption spectrum of the dye/colloid system, but closely resembles the absorption spectrum of the monomeric species of the free dye in solution with the peak at 597 nm.

We therefore assign the emission to a small fraction of dye not adsorbed on TiO_2. From its intensity we conclude, that the amount of free dye in solution is less than one percent.

We can calculate the amount of dye molecules per TiO_2 nanoparticles at the lowest concentration in figure 4.10 (1.5×10^{-6} mol/l Mc3 and 8 g/l nanoparticles) to be 0.8 dye molecules per TiO_2 nanoparticle on an average. At higher concentrations the dye starts to form H-aggregates.

Such an enhancement of aggregates when adsorbed on the surface of TiO_2 was also observed for the very similar dye merocyanine-2 [4.27].

4.4.3 Glycerol addition

In order to obtain a good optical quality glass for low temperature measurements down to 100 K, glycerol was added (spectrophotometric grade, Sigma Aldrich). After cooling we obtained a transparent glass without significant scattering loss.

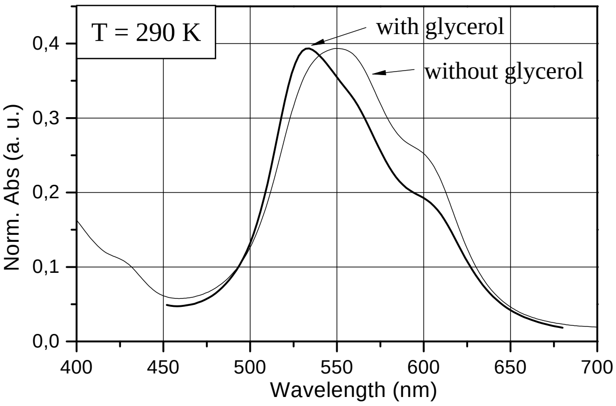

Figure 4.12: Steady-state absorption spectrum of 4×10^{-5} mol/l Mc3 and 8 g/l TiO_2 nanoparticles in a 4:1 water/ethanol solvent(thin solid line) and the spectrum after glycerol addition (1.6×10^{-5} mol/l Mc3 and 3.2 g/l TiO_2 nanoparticles in 32 % water/8 % ethanol/60 % glycerol, thick solid line) normalized to the blue peak without glycerol

The treatment of the dye/TiO_2 solution with glycerol resulted in a blue shift of the absorption maximum to 534 nm (see figure 4.12) with a small shoulder around 560 nm. This is near the wavelength of the dimer peak in the low temperature spectrum of the free dye. The red shoulder near 600 nm (at the monomer peak) decreased from 0.3 OD to 0.2 OD.

At low temperatures (figure 4.13,bottom), a sharpening of the absorption band and a slight increase in amplitude was observed .

Again, the emission spectrum at 290 K (not shown) with excitation at 500 nm was quenched by two orders of magnitudes with a peak at 623 nm. This is almost identical to the emission spectrum of the dye/colloid in solution without glycerol (figure 4.11).

The excitation spectrum for the emission at 620 nm (dashed line in figure 4.13, top) was similar to the absorption spectrum of the free dye with the maximum at 594 nm.

The lower figure in 4.13 shows the absorption spectrum and excitation spectrum of the emission at 597 nm at 100 K.

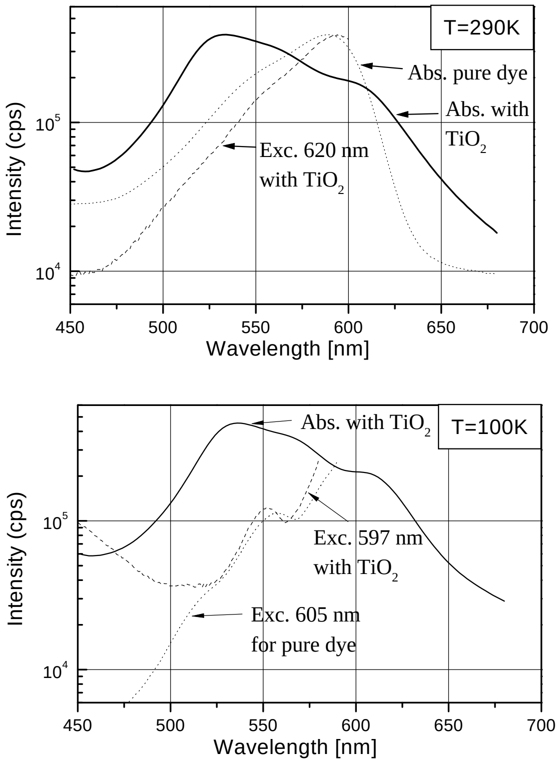

Figure 4.13: Steady-state spectra of 1.6×10^{-5} mol/l Mc3 and 3.2 g/l TiO_2 nanoparticles in a 32 % water/8 %ethanol/60 % glycerol solvent. **Top**: At room temperature (290 K). Thick solid line: Absorption spectrum normalized to excitation spectra; Dashed line: Excitation spectrum for emission at 620 nm. Dotted line: Absorption spectrum of pure dye as comparison. **Bottom**: At low temperature (100 K). Thick solid line: Absorption spectrum with the same scale as in the upper figure; dashed line: Excitation spectrum of the emission at 597 nm; dotted line: Excitation spectrum of the emission at 605 nm in the pure dye as comparison.

The excitation spectrum of the emission at 597 nm now has a peak at 552 nm and is slightly red shifted with respect to the excitation spectrum of the emission at 605 nm at 100 K in the pure dye (dotted line in figure 4.13, bottom).

From these measurements we can see, that the properties of the dye/TiO_2-colloid system are not changed after glycerol addition except for a blue shift of the aggregation band which is due to the polarity change after glycerol addition.

The broadening of the absorption spectrum by the aggregate species could be an advantage for the sensitization property of the dye, because an additional wavelength region for the excitation and subsequent photoinduced charge injection is available as long as the high injection efficiency for aggregates is maintained.

Indeed, high effficiency was reported for aggregates of cyanine dyes [4.40] and pinacyanol dye adsorbed on SnO_2 [4.41]. Moreover, the use of other dye aggregates in artificial photosynthetic systems [4.42] and in photoelectrochemical cells [4.43] was demonstrated recently.

4.4.4 Spectrum Analysis

From the concentration dependent steady-state absorption measurements (figure 4.10) we know, that the absorption signal of the Mc3/TiO_2-colloid system consists of a H-aggregate and monomer species.

In order to identify the contributions of the different species to the transient signals, we fitted the absorption spectrum of the dye/colloid system at 100 K with three gaussian functions (figure 4.14) representing the monomer, dimer and H-aggregate bands, respectively. The fit parameters are summarized in table 4.1.

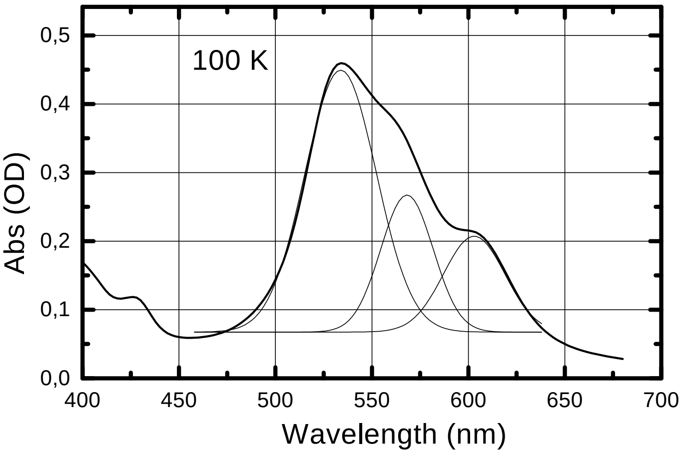

Figure 4.14: Least-squares fit with three gaussians (thin solid lines) to the steady-state absorption spectrum (thick solid line) of 1.6×10^{-5} mol/l Mc3 and 3.2 g/l TiO_2 in a 32 % water/8 % ethanol/60 % glycerol solvent at 100 K.

The main part with its maximum at 534 nm can clearly be attributed to higher order aggregates. This was proven by the measurements in figure 4.10, where we saw a concentration dependence of the signal and the blue shift of the H-aggregation band.

The two bands in the red part of the spectrum have their peaks at 568 nm and 603 nm. These bands are assumed to be the contribution of the

species	λ_{max} (nm)	FWHM (nm)	Amplitude (OD)
monomer	603	40.7	0.13
dimer	568	33.5	0.14
H-aggregate	534	47.5	0.33

Table 4.1: Fit results of a least-squares fit with three gaussians of the steady-state absorption spectrum (thick solid line) in figure 4.14.

adsorbed but not higher aggregated dye molecules consisting of a mixture of monomers and dimers. In the following, we will consider this mixture as one species, called the ”monomer species”.

4.4.5 Light Induced Effects

According to the observation of an illumination effect on pure dye at low temperatures, we investigated similar effects on the Mc3/TiO_2 system.

When the Mc3/TiO_2 colloid solution was prepared in the dark (except for a very weak red light) and protected from illumination until measurement, the steady-state absorption spectra at all temperatures were different than the spectra obtained under previous conditions (prepared in daylight).

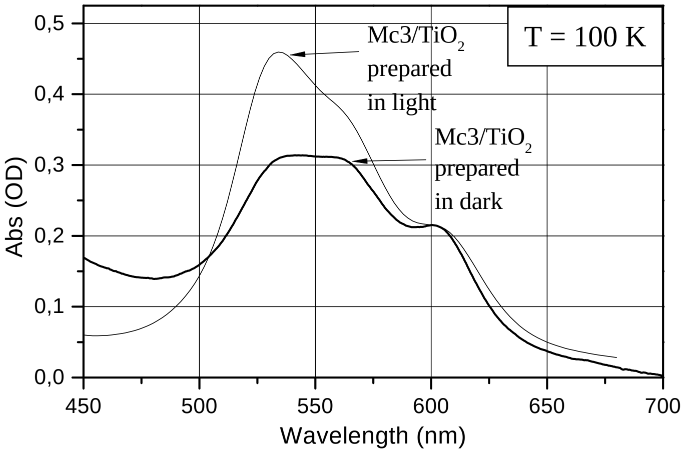

Figure 4.15: Steady-state absorption spectrum of 1.6×10^{-5} mol/l Mc3 and 3.2 g/l TiO_2 in a 32 % water/8 % ethanol/60 % glycerol solvent at 100 K. Thin solid line: Absorption spectrum of Mc3/TiO_2 prepared in daylight; Thick solid line: Absorption spectrum of Mc3/TiO_2 prepared in the dark. The spectra are normalized to the monomeric band at 603 nm.

Figure 4.15 is the steady-state absorption spectrum recorded at 100 K and normalized to absorption signal at 603 nm (monomer). We can clearly see, that the blue band is smaller relative to the monomeric shoulder and has an almost constant absorption over a spectral range of 20 nm (from 540 nm to 560 nm).

This means that at least a part of the higher order aggregates on the surface are only formed after illumination. On could imagine, that the dye molecules first adsorb on arbitrary surface sites as monomers due to the our low dye concentration. For higher order aggregation they have to detach and adsorb again on the surface, probably several times.

For this rearrangement energy is necessary. In the dark less energy is available, so that the formation of H-aggregates is less favorable.

4.5 Time-Resolved Measurements

Time resolved fluorescence data in the nanosecond regime were obtained by time-correlated single photon counting (TCSPC) [4.44] with a time resolution of 40 ps. The experimental set-up is described elsewhere [4.45]. With this system a fluorescence decay time of 2.3 ns was measured for the free dye. This lifetime did not change after adding of glycerol.

All transient absorption measurements on the ns to ms time-scale were performed on the system described in section 2.4. Since injection is expected to be very fast [4.11](a), [4.15](d),(e), all signals were developed within our temporal resolution.

Figure 4.16 shows the transient difference absorption spectrum of 1.6×10^{-5} mol/l Mc3 and 3.2g/l TiO_2 in a 32 % water/8 % ethanol/60 % glycerol solvent after excitation at 575 nm recorded at 5 ns delay time. The spectrum is similar to the related dye Mc2 [4.32] except for a blue shift by 20 nm.

Negative absorption changes above 525 nm can be attributed to the ground state bleaching, whereas the wavelength region below 525 nm illustrates the absorption of the dye cation $Mc3^+$ created by electron injection. For the pure dye in solution, we observed no difference absorption signal in the cation spectral region.

We can conclude, that the observed decay was solely due to the recombination dynamics of the injected electron with the dye cation $Mc3^+$.

For low temperature measurements glycerol was added. Amplitude and decay times were the same before and after glycerol addition.

When we compare the transient difference absorption signals (see figure 4.16) with the steady-state absorption spectrum (figure 4.14) we can see, that the transient signals are lower than expected. This is an indication that recombination times faster than our time resolution can occur.

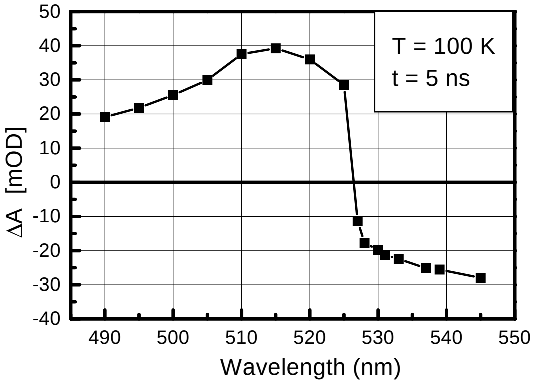

Figure 4.16: Transient difference absorption spectrum after excitation at 575 nm at 5 ns delay time. The sample contains 1.6×10^{-5} mol/l Mc3 and 3.2 g/l TiO_2 in a 32 % water/8 % ethanol/60 % glycerol solvent.

In the following we want to analyse the observed kinetics at different excitation and probe wavelengths. In chapter 4.4.4 we could attribute the three bands of the steady-state absorption spectrum to a monomer species and to a H-aggregate species. Under these circumstances we have to take in account different kinetics for these species.

One should also keep in mind, that the contributions of these species to the recombination signal cannot be strictly separated, because when probing one species at a certain wavelength, there is also a small contribution of the other species. However, we can assume that these contributions should be negligible at given wavelengths.

4.5.1 Excitation Wavelengths

All transient signals were multi-exponential and had to be fitted by a least-squares fit with at least three exponential decay functions. [1]

Excitation at 575 nm

After exciting the sample at wavelengths around 575 nm we probed the ground state bleaching of the aggregation band (around 540 nm) and the cation absorption signal (around 515 nm).

---

[1] In these fits, the results with a convolution of a gaussian peak representing the instrument function and a multiexponential decay were identical with the result of the multiexponential decay alone. This is most likely due to the long time constants. Here, we only show the results of the multiexponential decay.

As can be seen in figure 4.17, the cation decay probed at 515 nm (filled squares) and the ground state bleaching probed at 545 nm (filled triangles) were not identical. For better comparison the open circles represent the bleaching signal normalized to the positive cation signal (open circles).

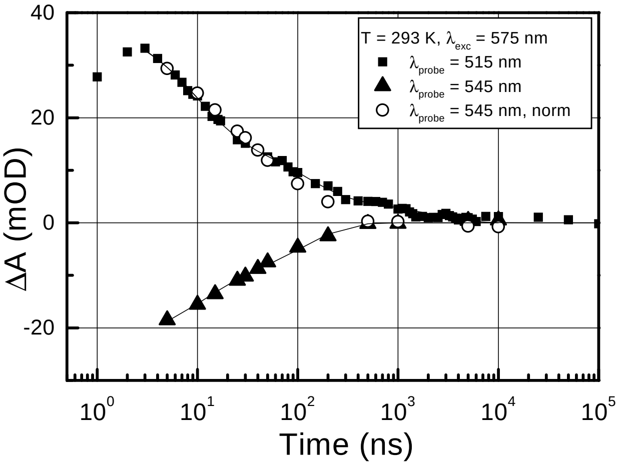

Figure 4.17: Transient difference absorption of cation (515 nm, squares) and ground state (545 nm, up triangles) after excitation at 575 nm. The solid lines represent global least-squares fits with three exponential functions (see text and table 4.2 for fit results). For comparison, the open circles are the ground state signals normalized to the cation signal. The sample contains 1.6×10^{-5} mol/l Mc3 and 3.2g/l TiO_2 in a 32 % water/8 % ethanol/60 % glycerol solvent.

The time constants resulting from the least-squares fits with three exponential functions were almost identical to each other with a major component (40 % - 50 %) between 10 and 20 ns and smaller components at 100 ns and 1000 ns.

The difference in kinetics became more obvious at low temperature (100 K, figure 4.18), The fastest component obtained from the fit procedure decreased to approximately 30 %. We had to add a fourth exponential function to the least-squares fit and an additional time component around 50 μs was extracted from the fit curve.

To further investigate the apparent difference in the two kinetics, we applied a global fit to the data. This means, we fitted the transients with the same time constants for ground state bleaching and cation decay (usually called the shared parameter), but let all other parameters free. The results are summarized in table 4.2.

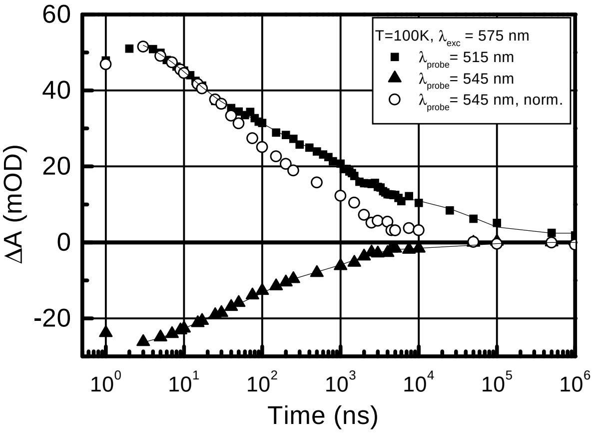

Figure 4.18: Transient difference absorption at 100 K of cation (515 nm, filled squares) and ground state (545 nm, filled up triangles) after excitation at 575 nm. For comparison the open circles are the ground state signals normalized to the cation signal. The solid lines represent global least squares fits with four exponential functions (see table 4.2 for fit results). The sample contains 1.6×10^{-5} mol/l Mc3 and 3.2 g/l TiO_2 in a 32 % water/8 % ethanol/60 % glycerol solvent.

T	λ_{exc}	λ_{pr}	A_1	τ_1	A_2	τ_2	A_3	τ_3 (μs)	A_4	τ_4 (μs)	$\langle\tau\rangle$	$\Delta\tau$
293	575	545	48 %	13.5	47 %	106	5 %	1.1	-	-	111	231
293	570	515	54 %	13.5	30 %	106	16 %	1.1	-	-	215	388
100	575	545	39 %	28.5	26 %	174	25 %	1.4	10 %	43.5	4756	12927
100	575	515	31 %	28.5	7 %	174	37 %	1.4	24 %	43.5	10979	18252

Table 4.2: Fit results of a global least-squares fit with shared time constants (in ns, except stated otherwise) of the transient curves after excitation at 575 nm (figure 4.17 and 4.18). The two last columns are the weighted average $\langle\tau\rangle = \sum A_i\tau_i$ and the variance $\Delta\tau = \sqrt{\sum A_i(\tau_i - \langle\tau\rangle)^2}$.

Excitation at 540 nm

After excitation of the sample with wavelengths around 540 nm, the decay kinetics of the ground state bleaching of the monomer species (around 580 nm) and that of the cation decay were approximately the same for 273 K (figure 4.19). A least-squares fit with three exponential functions was sufficient.

At low temperatures (100 K, not shown) the recombination kinetics slowed down and a fourth time component for the fit was necessary. Ground state bleaching and cation decay kinetics still were similar like at 273 K.

Table 4.3 summarizes the results of a global fit with shared time constants.

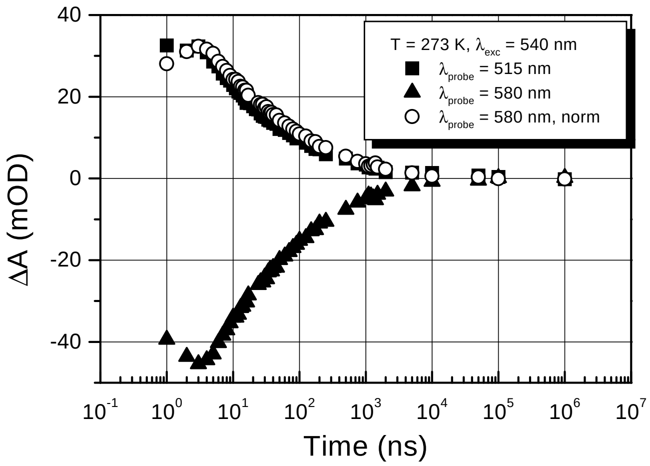

Figure 4.19: Transient difference absorption of cation (515 nm, filled squares) and ground state (580 nm, filled up triangles) after excitation at 540 nm. For comparison the open circles are the ground state signals normalized to the cation signal. The sample contains 1.6×10^{-5} mol/l Mc3 and 3.2g/l TiO_2 in a 32 % water/8 % ethanol/60 % glycerol solvent. For fit results see table 4.3.

T	λ_{exc}	λ_{pr}	A_1	τ_1	A_2	τ_2	A_3	τ_3 (μs)	A_4	τ_4 (μs)	$\langle\tau\rangle$	$\Delta\tau$
273	540	580	51 %	8.5	31 %	98	19 %	1.3	-	-	282	496
273	540	510	55 %	8.5	31 %	98	15 %	1.3	-	-	230	452
100	540	580	27 %	11	26 %	107	29 %	1.5	10 %	65	6966	19255
100	540	510	36 %	11	23 %	107	28 %	1.5	24 %	65	16049	28046

Table 4.3: Fit results of a global least-squares fit with shared time constants (in ns, except stated otherwise) of the transient curves after excitation at 540 nm (figure 4.19). The two last columns are defined as in the previous table 4.2.

Ground State Bleaching

As we have seen, the ground state recovery has a different decay curve for different probe wavelengths. Figure 4.20 illustrates this fact in one graph for better comparison (signals are normalized to 100). The ground state bleaching of the H-aggregate band (probe at 545 nm, filled squares) recovers faster than the ground state bleaching of the monomer band (probe at 580 nm, open circles). As shown, both curves can be fitted to similar time constants even though with different amplitudes (see tables 4.2 and 4.3).

When we compare the initial amplitudes of the ground state bleaching in figure 4.17 and 4.19 (filled up triangles), we see, that the absolute values when probing the aggregates is more than two times lower than that of the monomer species (-18.5 mOD at 545 nm versus -44.5 at 580 nm, t = 5 ns).

From the steady-state absorption spectrum (figure 4.14) we would expect

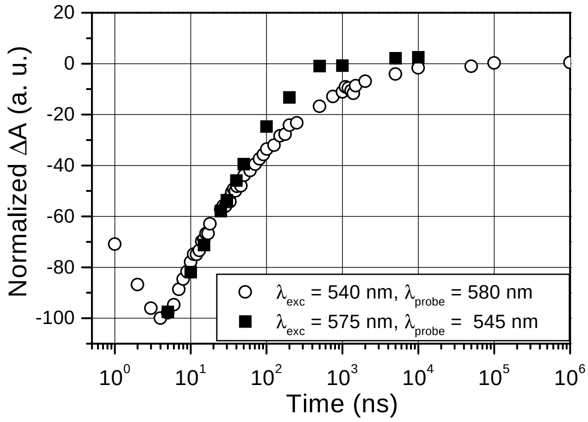

Figure 4.20: Transient difference absorption signals of the ground state recovery after excitation at 540 nm (filled squares) and 575 nm (open circles) at room temperature. Both signals are normalized to 100. The sample contains 1.6×10^{-5} mol/l Mc3 and 3.2g/l TiO_2 in a 32 % water/8 % ethanol/60 % glycerol solvent.

that the difference absorption signal for the blue part of the spectrum should be higher, when there are no competitive processes or kinetics faster than our time resolution.

Cation Decay

The transients for cation decay (probe at 510 nm) after excitation at wavelengths between 530 nm and 580 nm did not show these differences. The absolute amplitudes of the difference absorption signal differed only slightly at different excitation wavelength (filled squares in figure 4.17 and 4.19).

Figure 4.21 is an example for the transient kinetics of the cation decay at 100 K after excitation at 570 nm (filled squares) and 540 nm (open circles) normalized to 100. The slightly faster decay after excitation at 540 nm could be explained by the assumption that we mainly excited the H-aggregates at this wavelength. The faster recombination was already observed in the ground state recovery data. However, both curves seem to become identical at very long times.

Table 4.4 summarizes the parameters of a global fit with shared time constants of the transient cation signal after excitation of the monomer species (570 nm) and the aggregated species (540 nm) at 273 K and 100 K, respectively.

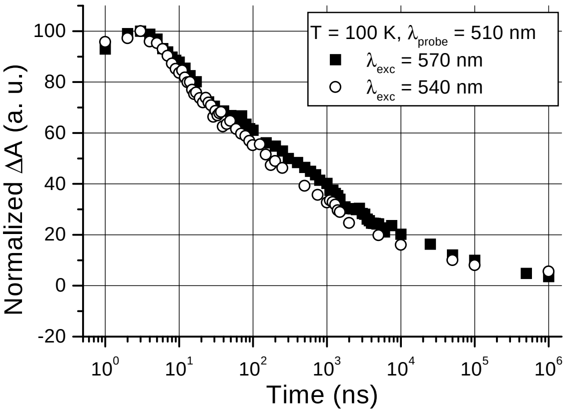

Figure 4.21: Transient difference absorption signals of the cation decay after excitation of aggregates (540 nm, open circles) and monomers (570 nm, filled squares) at 100 K. Both signals are normalized to 100. The sample contains 1.6×10^{-5} mol/l Mc3 and 3.2g/l TiO_2 in a 32 % water/8 % ethanol/60 % glycerol solvent.

T	λ_{exc}	λ_{pr}	A_1	τ_1	A_2	τ_2	A_3	τ_3 (μs)	A_4	τ_4 (μs)	$\langle\tau\rangle$	$\Delta\tau$
273	540	510	47 %	8.2	34 %	80.4	19 %	1.05	-	-	231	398
273	570	510	47 %	8.2	36 %	80.4	17 %	1.05	-	-	211	381
100	540	510	34 %	14.3	28 %	216	27 %	2.7	11 %	106	12454	32906
100	570	510	30 %	14.3	25 %	216	29 %	2.7	16 %	106	17801	38510

Table 4.4: Fit results of a global least-squares fit with shared time constants (in ns, except stated otherwise) of the transient cation decay signal after excitation of aggregates (540 nm) and monomer species (570 nm). The two last columns are defined as before.

Summary

In a final comparison the ground state recovery and cation decay of both the monomer and the aggregated species are shown in figure 4.22. It illustrates the described features of ground state recovery (different decay times, large difference in amplitudes) and cation decay (identical kinetics, comparable amplitudes).

From the observed data it is apparent, that there is a difference in the decay times of the ground state bleaching at different wavelengths. Since for the ground state bleaching only the probe wavelength is relevant, the bleaching signal after excitation at 575 nm and probing at 545 nm is assigned to the H-aggregate species whereas the bleaching signal after excitation at 540 nm and probing at 580 nm is assigned to the monomer species.

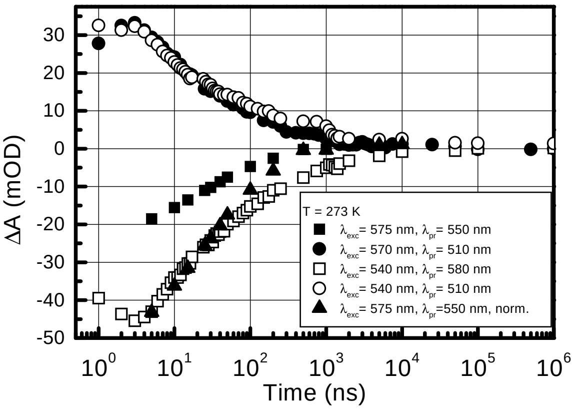

Figure 4.22: Transient difference absorption signals of the ground state recovery (squares) and cation decay (circles) of the different species. Filled squares: Excitation at 575 nm, probe at 550 nm; Open squares: Excitation at 540 nm, probe at 580 nm; Filled circles: Excitation at 570 nm, probe at 510 nm; Open circles: Excitation at 540 nm, probe at 510 nm; Filled triangles: Same as filled squares, but normalized to ground state recovery with excitation at 540 nm and probe at 580 nm (open squares). The sample contains 1.6×10^{-5} mol/l Mc3 and 3.2g/l TiO_2 in a 32 % water/8 % ethanol/60 % glycerol solvent.

The kinetics of the cation decay transients are not significantly different when exciting aggregates and monomers, respectively. The findings of this chapter are summarized in table 4.5 and will be discussed in chapter 4.5.3.

λ_{exc}	λ_{pr}	observed signal	notes
575 nm	545 nm	H-aggregate ground state bleaching	fast recovery
575 nm	510 nm	Cation decay signal	slow decay
540 nm	580 nm	Monomer ground state bleaching	slow recovery
540 nm	510 nm	Cation decay signal	slow decay

Table 4.5: Summary of the observed kinetics of the different species.

4.5.2 Magnetic Field Effect (MFE)

When radicals are created, they are generated in pairs (here the dye cation as donor and the TiO_2 particle as acceptor). The unpaired electron of this pair will have total spin 0 when created in the singlet state. For large enough distances between the radicals (this means negligible spin-spin interactions), triplet and singlet states are almost degenerate, and the wave function of the spin pair may be written as a superposition of both singlet and triplet contributions. The spin vector sum of the radical pair becomes time dependent due to the differences in the hyperfine interactions and in the electronic gyromagnetic ratios for the spin wave functions of the radicals. As a result, the probability for recombination to the triplet state depends on time.

When a magnetic field is applied, the magnetic spin moments of both radicals precess around the resultant of external and internal magnetic fields.

Moreover, the triplet state splits up in three sublevels with different spin quantum numbers ($m_s = -1, 0, 1$) separated by the Zeeman energy. When the magnetic field is high enough, only the singlet level and the triplet level with $m_s = 0$ are close in energy. The two other triplet states with $m_s = -1, 1$ are energetically to far away from the singlet level and are not able to mix with the singlet state.

This means that in high magnetic fields the overall yield of triplet states will be lower than in zero field. This is the so-called MARY effect (Magnetic Field Effect on Reaction Yield) which can be measured by monitoring the transient difference absorption of a reaction product as a function of applied magnetic field.

More detailed information about radical pair mechanism and the MARY method can be found in [4.46] and references therein.

Up to now there are no studies about magnetic field effects on the recombination kinetics in a sensitizer/semiconductor system.

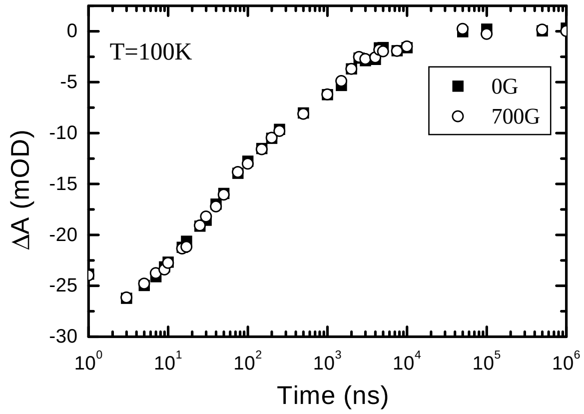

Figure 4.23: Transient difference absorption signal of 1.6×10^{-5} mol/l Mc3 and 3.2 g/l TiO_2 in a 32 % water/8 % ethanol/60 % glycerol solvent at 100 K without magnetic field (solid squares) and with a magnetic field of 700 G applied (open circles). Excitation wavelength 575 nm, probe wavelength 540 nm

We did not observe any signals which could be attributed to triplets. This was checked at probe wavelengths around 650 nm both with and without a magnetic field of 700 G. Thus, triplets can be excluded in our system.

Transient ground state bleaching signals with an applied magnetic field of 700 G at both high temperatures and low temperatures also showed no significant effect on the recombination kinetics. Figure 4.23 is an example of these experiments and shows that both curves without (solid sqares) and with magnetic field (700 G, open circles) are not distinguishable.

This is probably due to a fast spin-lattice relaxation in TiO_2. In EPR studies of trapped electrons in UV-irradiated colloidal TiO_2 a large line width broadening in the EPR spectrum above 77 K was observed [4.47]. Since no Ti^{3+} signals at room temperature could be detected, it was concluded, that spin-lattice relaxation evidently causes line broadening above 77 K.

4.5.3 Discussion

Monomers and aggregates

From the observed data it is apparent, that there is a difference in the decay times of the ground state recovery at different wavelenghts. The concentration dependent steady-state absorption spectrum of the dye absorbed on TiO_2 particles (figure 4.10) clearly proves the existence of a higher order aggregation (H-aggregates) additional to a mixed monomer/dimer species which were exclusively found for the free dye in solution at low temperatures. This finding suggests, that the difference in kinetics can be attributed to differences in the recombination of the H-aggregates and the monomer species.

Comparison of the ground state bleaching (figure 4.22) shows, that the signal amplitude of the H-aggregates is significantly smaller than that of the monomer species though according to the steady-state spectrum (figure 4.14) the steady-state absorption is considerably larger. There are two possible explanations.

a) Aggregation is assumed to enhance the probability of other processes like energy transfer. The time scale of these processes is expected to lie in the sub-nanosecond range and can compete with charge injection.

   As pointed out in chapter 4.4, in H-aggregates efficient quenching of the upper exited state to the lower excited state may occur. This may lead to a reduction of injection efficiency and correspondingly to a smaller transient signal.

b) The recombination of the aggregates is faster than our time resolution and we can only see a part of the initial amplitude of the ground state

> bleaching signal. The faster recombination time of the H-aggregates could be the consequence of a stronger binding at the surface which means a stronger coupling. In general, recombination times depend strongly on the nature and geometry of the binding site of the dye, which is not obvious for the given structure and is even more complicated for the higher order aggregates. Sub-nanosecond recombination times of higher order aggregates were already observed for H-aggregates of cresyl violet adsorbed on SnO_2 [4.48].

We also cannot exclude sub-nanosecond recombination for the monomer species because of the obvious (even though not so significant) difference in amplitudes in the transient and steady-state spectra, respectively. Picosecond recombination times were already reported in other systems, for example for monomeric alizarin adsorbed on TiO_2 [4.13].

The transients of the cation decay signal are not significant different when exciting aggregates and monomers, respectively. The decay time is approximately the same as the recovery time of the monomer ground state bleaching.

This may be an indication, that our probe wavelengths (510 nm and 515 nm) lie near the isosbestic point of the transient spectrum of the H-aggregates. Because a part of the monomer species is also excited at wavelengths near 540 nm, the amplitude of the cation decay signal due to the recombination with monomers may be higher than that due to recombination with H-aggregates. In this case, the contribution of the H-aggregates to the cation decay signal is negligible.

Dispersive Kinetics

Slow, non-exponential transients in the micro- and millisecond time scale were also reported for investigations on photocurrent and recombination kinetics in nanocrystalline TiO_2 films and electrodes [4.49] where the response times were found to depend on the intensity of the incident light [4.50], [4.51] and on an applied voltage across the cell [4.52].

Such dispersive kinetics could point to a spatial and/or energetic distribution of electrons trapped in the surface states of the nanoparticles.

In general, the trap states are presumed to be on the surface of the particles because of the large surface-to-volume ratio. However, there is no definite proof for this expectation. In principle, it is also possible that the electrons are randomly distributed within the volume of the particles. In this case, recombination occurs via the conduction band.

Models

Appplication of conventional semiconductor transport theory based on the diffusion equation [4.53] to recombination from the bulk, however, could not explain the observed transients. Several attempts to include trapping and detrapping terms into the diffusional model [4.50](b), [4.54], [4.55] did not lead to improvements.

Other theoretical studies attribute the observed kinetics to a high density of surface trap states and utilize random walk [4.56] or random flight [4.57] approaches where electrons can undergo multiple trapping and detrapping events to the conduction band before recombination occurs. These trap states are assumed to have an exponential distribution of energies [4.58] called Urbach tails, which have been detected in absorption and photothermal deflection spectra. In these experiments, two kinds of tails with low energy (0.11 - 0.17 eV) and high energy (0.20 - 0.34 eV), respectively, were observed [4.59].

Because of the high number of trap sites the electron is multiply trapped on the surface before it can recombine with the dye cation. When the number of walking electrons is sufficiently high, recombination is assumed to be mainly an intraparticle process and is not considered as the rate limiting step.

To simplify the calculation, it is assumed that the electron density in the conduction band is negligible and the capture cross section is the same for all traps and cations. The main difference in both models concerns the detrapping process. The random walk model proposes, that any electron which is thermally detrapped into the conduction band can only be retrapped by its neighbouring trap state. In the random flight model it can recombine with the cation or can be recaptured by any empty trap with equal probability.

a) **Random walk model:** The recombination transients predicted by this model behave in its simplest forms like strechted exponentials

$$\Delta A(t) = \Delta A(0) exp(-k_w t^{\alpha}) \tag{4.8}$$

where k_w is proportional to the number of walking electrons provided that they greatly outnumber the cation targets. The dispersive parameter α (with $0 < \alpha < 1$) defines the shape of the energy distribution of the trap states and depends linearly on temperature:

$$\alpha = \frac{k_B T}{E_0} \tag{4.9}$$

where E_0 is the characteristic energy of the trap states.

b) **Random flight model:** The transients are proportional to an algebraic expression

$$\Delta A(t) = \Delta A(0)(1 + k_f t^{\alpha})^{-1} \tag{4.10}$$

Here, $k_f = (n_0/N)c$, where n_0/N is the ratio between photogenerated electrons and trap sites (usually $\ll 1$) and c contains all information about the migration mechanism (allowing for some contribution of nearest neighbour random walk), spatial configuration and density of trap sites.

It should be noted however, that the physical information one can extract from these models is limited. The main reason for their application was to demonstrate, that stretched exponentials can satisfactorily reproduce transient photocurrent and recombination kinetics observed in practise with only a few fitting parameters.

When applying least-squares fits with these fit functions to our data we obtained fit curves which matched our data as good as fits with three or four exponential functions, and the χ^2 values were of the same order.

Application to Experimental Data

Random walk model The initial amplitude ($\Delta A(0)$) is a critical parameter here, since due to our limited time resolution, we might miss a part of the fast recombination. This amplitude is proportional to

$$\Delta A(0) \propto \epsilon_{probe}(1 - exp(-\epsilon_{exc}\sigma_{abs}n)) \tag{4.11}$$

where ϵ_{probe} and ϵ_{exc} are the absorption coefficients at the probe and excitation wavelength, respectively, σ_{abs} is the absorption cross section and n is the photon density in photons per cm^2. The product $\sigma_{abs}n$ depends on excitation energy. This has been monitored and was taken equal at low and high temperatures.

With the assumption that the exponent is small ($1 - exp(-\epsilon_{exc}\sigma_{abs}n) \approx \epsilon_{probe}\epsilon_{exc}\sigma_{abs}n$), we can get an approximate ratio between the amplitudes at low temperature (LT) and high temperature (HT).

$$\frac{\Delta A(HT)}{\Delta A(LT)} = \frac{\epsilon_{probe}(HT)\epsilon_{exc}(HT)}{\epsilon_{probe}(LT)\epsilon_{exc}(LT)} \tag{4.12}$$

The absorption coefficients were taken from our gaussian fit in figure 4.14 (see table 4.1). The results (corrected for some offset) were taken as a constraint for the fit:
$\Delta A(HT)_{545nm} = 1.032 * \Delta A(LT)_{545nm}$ and
$\Delta A(HT)_{580nm} = 1.1567 * \Delta A(LT)_{580nm}$

As shown above, the temperature dependence is included in the parameter α, while k_w is according to the random walk model proportional to the walking (photoexcited) electrons and should be the same for the same excitation wavelength. Therefore, we set k_w as a shared parameter for low and high temperature.

It should be noted however, that k_w is a proportionality factor and has no real physical meaning. It is used as fit parameter with the dimension ($\mathrm{ns}^{-\alpha}$) to obtain a dimensionless exponent. The fit results are shown in table 4.6.

T	λ_{exc}	λ_{probe}	$\Delta A(0)$	k_w	α
273 K	540 nm	580 nm	-105.1	0.54	0.284
100 K	540 nm	580 nm	-90.8	0.54	0.157
293 K	575 nm	545 nm	-66.9	0.694	0.3
100 K	575 nm	545 nm	-65.6	0.694	0.189

Table 4.6: Fit results of a global least-squares fit with a stretched exponential function (equation 4.8) with shared parameter k_w of the ground state recovery after probing at 580 nm (monomer) and at 545 nm (H-aggregate). Same data as in table 4.2 and 4.3. As a constraint, the ratios of the initial amplitudes $\Delta A(0)$ at room temperature and at 100 K were fixed (see text).

The parameter k_w (proportional to walking electrons) increased from 0.54 for monomers to 0.694 for H-aggregates. The fitted amplitudes $\Delta A(0)$ were always higher than in our multiexponential fits, again indicating evidence for sub-nanosecond decay times.

At room temperature we obtained α values of 0.284 and 0.3, respectively. This is not far away from $0.35 < \alpha < 0.43$ in reference [4.56] which was obtained from voltage dependent measurements on a ruthenium-complex/$\mathrm{TiO_2}$ system [4.52]. Application of equation 4.9 leads to a characteristic trap site energy of approximately 0.08 eV This is not so far away from the low-energy Urbach-tails (0.11 - 0.17 eV) in reference [4.59].

The temperature dependence of the α parameter did not match with the predictions of the theory. α should have a linear dependence on temperature (equation 4.9, and should therefore increase approximately threefold from 100 K to room temperature (293 K and 273 K, respectively). But our fitted values increased not more than by a factor of two.

When fitting the low temperature data with the α parameter fixed to the expected value, the fit curve did not match at all.

As an example, figure 4.24 illustrates the obvious mismatch for the aggregate ground state bleaching (excitation at 575 nm, probe at 545 nm) for 293 K (figure 4.17) and for 100 K (figure 4.18) with the same fit parameters as in table 4.6 except for the constraint $\alpha(100K) = \alpha(293)/2.93$.

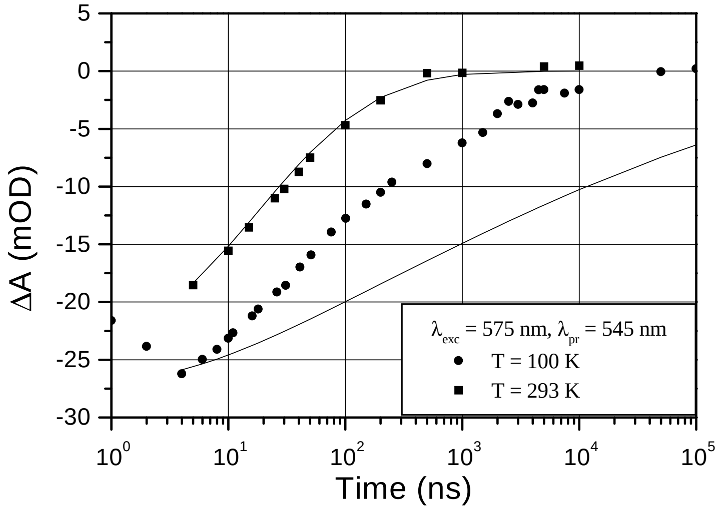

Figure 4.24: Mismatch of the fit curves for transient ground state bleaching signal of the aggregate species (excitation at 575 nm, probe at 545 nm) at T = 293 K (squares, see up triangles in figure 4.17) and at T = 100 K (circles, see up triangles in figure 4.18).

Such a temperature dependence reflects the freezing of trapped electrons which no longer can access the conduction band.

Random flight model Application of the random flight model with the same constraints for the initial amplitudes and setting k_f as a shared parameter as in the random walk model gave the fit results compiled in table 4.7.

T	λ_{exc}	λ_{probe}	$\Delta A(0)$	k_f	α
273 K	540 nm	580 nm	-82.99	0.336	0.557
100 K	540 nm	580 nm	-71.75	0.336	0.278
293 K	575 nm	545 nm	-32.78	0.11	0.92
100 K	575 nm	545 nm	-31.76	0.11	0.56

Table 4.7: Fit results of a global least-squares fit to the random flight model (equation 4.10) with shared parameter A of the ground state recovery after probing at 580 nm (monomers) and at 545 nm (H-aggregates). Same data as in table 4.2 and 4.3. As a constraint, the ratios of the initial amplitudes $\Delta A(0)$ at room temperature and at 100 K were fixed (see text).

Once again, the α values increased approximately twofold from 100 K to high temperatures. Furthermore, their absolute values were remarkably different for monomers and aggregates. Application of the random flight model to the experimental data in reference [4.52] gave $0.39 < \alpha < 0.46$ [4.57] which is smaller than our results. The resulting characteristic energy was 0.042 eV for monomers and 0.027 eV for H-aggregates respectively

The parameter k_f for the H-aggregates decreased by a factor of three with respect to the monomer species. The differences in the initial amplitudes $\Delta A(0)$ of monomers and aggregates, respectively, point to differences in the injection quantum yields.

It should again be emphasized that these models were developed for situations given in photoelectrochemical cells, in particular to study the effect of an applied electric field across the cell. It must be taken into account that one ore more assumptions in these rather complex models do not hold in our simple dye/colloid system, for example the assumption of a high number of walking electrons (critical for application of the random walk model) since at our excitation energy (around 40 μJ) approximately 25 % of the molecules (corresponding to 5 molecules per nanoparticle) were excited.

Further complication seems to result from H-aggregates as evident from the significant differences in α (random flight). One can imagine, that the positive charge becomes delocalized over the aggregate or can migrate within the aggregate. This could result in a speeding up of the recombination. The same effect can be expected, when two or more electrons are injected by the same H-aggregate. In this situation a higher density of both electrons and cations are available for recombination.

Another explanation for the discrepancy of the models, especially with respect to the temperature dependence of the α parameter, may be the neglect of tunneling effects. At low temperatures the electrons do not have enough energy to escape the trap states by thermal activation. In this situation temperature independent tunneling effects become significant.

Although the kinetic traces could satisfactorily be fitted by both models, better theoretical models explaining charge transport and recombination in such dye/TiO$_2$ systems remain to be developed.

Chapter 5

Activated Hole Transfer in Acridine-Modified DNA

5.1 Structure and Function

DNA is probably the most thoroughly studied molecule today. Nevertheless, a very brief description of its basic properties is given.

In 1953, Watson and Crick could discover the structure in detail [5.1]. Every DNA-sequence consists of two strands: Each strand is built up by sugar molecules (2'-desoxy-ribose) connected by 3',5'-phosphodiester bonds (phosphate-backbone). The DNA-bases (purines and pyrimidines in figure 5.1) are covalently linked to the sugars. Sugar-base compounds are called nucleosides, phosphate-sugar compounds are nucleotides.

The strands are connected by hydrogen bonds, which are formed between the bases. Because of conformation considerations a purine (G or A) can

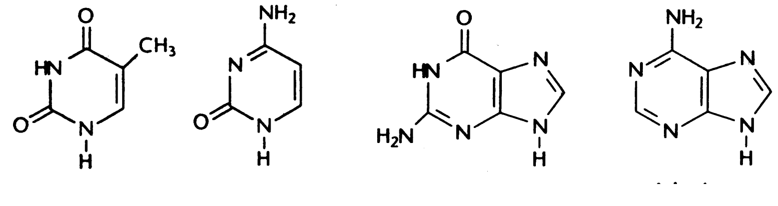

Thymine **Cytosine** **Guanine** **Adenine**

(T) **(C)** **(G)** **(A)**

Figure 5.1: Chemical structure of pyrimidine- and purine-bases in DNA

only bind to a pyrimidine (C or T). There exist only two possible base-pairs: (G,C) forming three hydrogen bonds and (A,T) forming two hydrogen bonds (Watson-Crick-Pairing). Thus, the bases are complementary, so that a base at the first strand determines the base on the opposite strand. The strands are situated antiparallel to each other, i. e. one strand runs in the 3' ⇒ 5'-direction, the other in the 5' ⇒ 3'-direction. (opposite polarity).

The bases represent the letters of a code which stores the genetic information of the cell. A sequence of three base-pairs represent one gene which is the fundamental unit of this code.

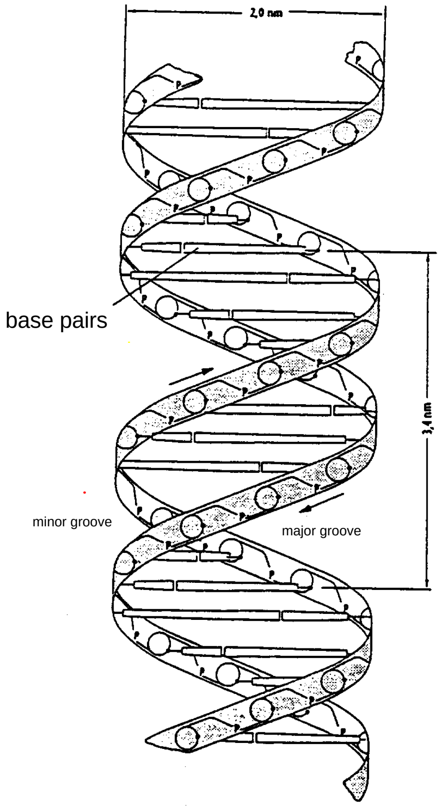

Figure 5.2: The Watson-Crick-Model of the DNA double helix (B-DNA)

The most astonishing property of DNA is the unique secondary structure of the double strand. The two single strands wind in a helical structure forming a spiral staircase (double helix, figure 5.2). The distance between two base-pairs is 3.4 Å, and every base-pair is rotated by 36° to each other. Every 10 base-pairs the double helix performs one clockwise rotation resulting in a distance of 3.4 nm per turn, whereas the width is 2 nm. Because the

DNA strand can extend its length in macroscopic dimensions (some μm), it is often folded in a tertiary structure for stability.

5.2 Charge Transfer Theory

At the first glance, one would conclude, that DNA is a typical insulator. For example, the bases are not arranged in a periodical crystalline structure. The conformation and flexibility of the strand rather depend on the local base sequence and on the concentration of water and ions in the surrounding.

However, even before the discovery of DNA structure it was suggested, that charge transfer interactions involving nucleotide bases could play a critical role in biology [5.2]. Nevertheless, there does exist a somehow repetitive structure considering the unoccupied π*-orbitals of the stacked base-pairs. Like in a conduction band, $\pi - \pi$ interactions could form a conduction band analogy [5.3] which could provide a fast one-dimensional charge separation confined to the base-pair core. In spite of subsequent theoretical and experimental effort, evidence for such a ”molecular wire” type conduction remained elusive [5.4].

This mechanism seems to play a critical role in the study of oxidative damage in DNA (for recent reviews, see [1.5]) induced mainly by ionizing radiation [5.5] and strong oxditans (chemical ionization, [5.6]). It is known from electrochemical [5.7], theoretical [5.8] and chemical investigations [5.9], that guanine is the base with the lowest oxidation potential of the four natural bases (with $G < A < C \simeq T$). Therefore, the major oxidation product is a guanine radical cation ($\mathrm{G}^{+\bullet}$ [5.10]), that can react further with water or oxygen [5.11] leading to mutations [5.12].

In recent studies Barton et al. [5.13] and Schuster et al. [5.14] have observed, that oxidation damage can occur at guanine bases that are far away form the oxidant. Their investigations indicated the possibility of long range charge separation (hole migration) in DNA, which is almost distance independent. Analyses of DNA strand cleavage patterns showed that distances of about 200 Å can be spanned [5.15]. This ”chemistry at a distance” [1.11] lead to the conclusion, that DNA could be considered as a ”molecular wire”. This kind of charge migration cannot be explained by a superexchange mechanism.

5.2.1 Superexchange

In a simplified picture we can describe the DNA-lesion/DNA-sequence/guanin system as a donor/bridge/acceptor system ($\mathrm{D} - \mathrm{B} - \mathrm{A}$). In the superexchange picture the charge is transferred to the acceptor via the overlapping

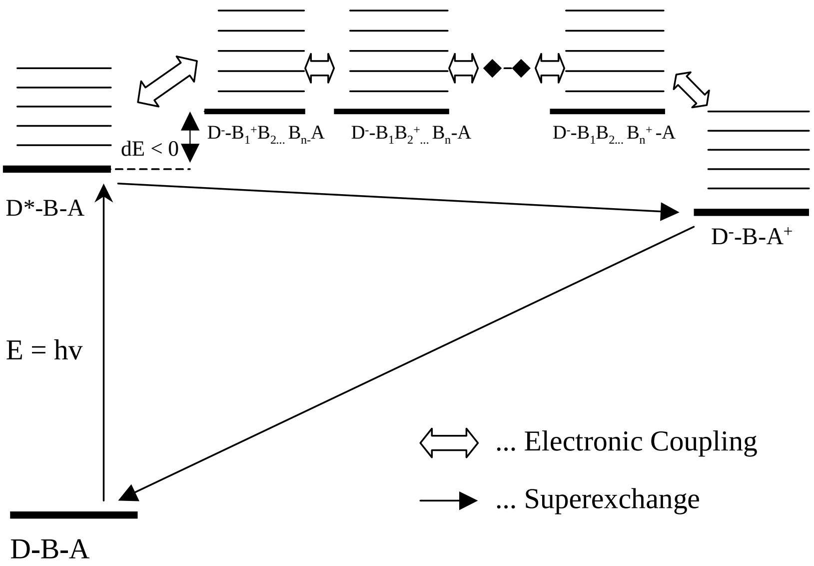

Figure 5.3: Superexchange mechanism for a donor/bridge/acceptor system as a simplified model for hole migration in DNA

orbitals of the bridge, without forming kinetic intermediates ($\mathrm{D}^- - \mathrm{B}^+ - \mathrm{A}$). Instead, the bridge states increase the electronic coupling between donor and acceptor through the superexchange interaction (figure 5.3).

An important condition for this kind of transfer is, that the free Gibbs enthalpy ΔG of the bridge states lies well above the enthalpy of the ground state and the low lying vibronic states of the donor (around $\sim k_B T$). In this off-resonance condition ($d\Delta G = \Delta G_B - \Delta G_D \gg 0$) the dependence of the electron transfer rate k (in s^{-1}) on the donor/acceptor distance R (in Å) is described by the Marcus-Levich-Jortner equation [5.16]:

$$k_{ET} = (2\pi/\hbar)V^2 FC \tag{5.1}$$

The term $V = V_0 exp[-(\beta/2)R]$ is (approximately) the electronic coupling for the transfer process, and it is characterized by the electronic coupling at donor/acceptor closest contact, V_0, and the attenuation parameter β, which depends on the electronic coupling of both donor and acceptor to the bridge and the vertical energy gap between the donor and the bridge states.

The FC term (Franck-Condon factor) comprises the thermally averaged nuclear Franck-Condon density of states involving high-frequency intramolecular vibrations and a nuclear reorganization energy λ_i, the low-frequency reorganization energy λ_s, which is (mostly) related to the response of the medium to changes in the charge distribution, as well as the change in Gibbs free energy ΔG driving the electron transfer reaction (driving force).

The quantum mechanical formulation of the FC factor is of special importance for highly exoergic reactions since it provides for the explanation of experimental electron transfer rates, which are larger than the ones given by the classical Marcus expression [1.1].

$$FC = \frac{1}{\sqrt{4\pi\lambda_s k_B T}} exp\left[\frac{-(\Delta G + \lambda_s)^2}{4\lambda_s k_B T}\right] \tag{5.2}$$

where k_B is the Boltzmann constant and T the temperature.

5.2.2 Hopping Mechanism

In contrast to this simple model, the description of long-range hole transport in duplex DNA is complicated by the different energetics of the nucleobases, i. e. the different oxidation potentials [5.9]. Experiments and theory led to the conclusion that in a duplex constructed of (G,C) base-pairs separated by short (A,T) sequences (up to four base-pairs, [5.17]) holes propagate by hopping between the nucleobases with the lowest oxidation potential, that is, the guanines.

This mechanism will prevail, when three energetic conditions are satisfied simultaneously (figure 5.4, [1.12], [5.18]):

- Resonant coupling between the electronic origin and low vibronic levels of the initial $D^* - B_1 B_2 \cdots B_N - A$ state with the vibronic manifold of the primary ion pair $D^- - B_1^+ B_2 \cdots B_N - A$, i. e. $\delta\Delta G < 0$.
- Near degeneracy of the origins of the vibronic manifolds of the ion pair states $D^- - B_1^+ B_2 \cdots B_N - A$, $D^- - B_1 B_2^+ \cdots B_N - A$, ... , $D^- - B_1 B_2 \cdots B_N^+ - A$
- Degeneracy of the vibronic manifolds of the last bridge ion pair state $D^- - B_1 B_2 \cdots B_N^+ - A$ and the final ion pair state $D^- - B_1 B_2 \cdots B_N - A^+$.

The resonant coupling results in the injection of the charge into the appropriate B_1 base of DNA. The near degeneracy then will induce charge hopping between the bases B_j (j = 1, ..., N) while the degeneracy of the last bridge state with the final state will result in charge trapping at the acceptor center.

For calculating the transfer rate k, the contributions of injection, transport and trapping depend on the individual electronic coupling and the FC factors of the ground and vibronic states of all the $\mathrm{D} - \mathrm{B} - \mathrm{A}$ states. A

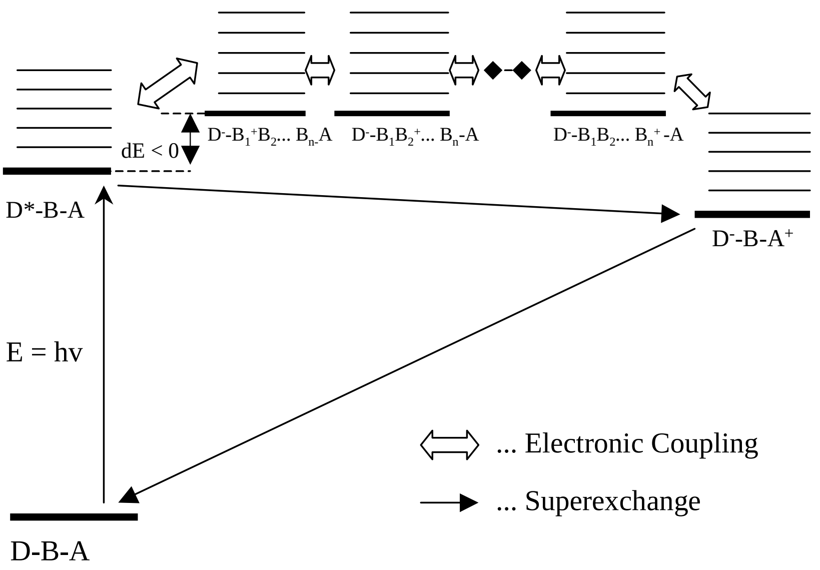

Figure 5.4: Hopping mechanism for a donor/bridge/acceptor system with different energetics of the bridge states as a model for DNA hole migration

microscopic description uses an extension of the theoretical models for the dynamics in multiple Franck-Condon quasicontinua [5.19].

Electron transfer theory gives the thermally averaged Franck-Condon density FC, which incorporates both medium and intramolecular vibrational modes [5.16](b),(c), [5.20]

$$FC = \frac{1}{\sqrt{4\pi\lambda_s k_B T}} exp(-S) \sum_{n=1}^{\infty} \frac{S^n}{n!} exp\left[\frac{-(\Delta E + \lambda_s + n\hbar\omega)^2}{4\lambda_s k_B T}\right] \tag{5.3}$$

where λ is the medium reorganization energy involving the contribution of low frequency vibrational modes, while the high frequency intramolecular vibrational modes are characterized by the (mean) vibrational frequency ω and coupling $S = \frac{\lambda_i}{\hbar\omega}$, and ΔE is the free energy gap.

A lenghty theoretical calculation [1.12] gives a weakly distance dependent hopping rate which is controlled by the number of the hopping steps N:

$$k \simeq \frac{k_{HOP}}{N^\eta} \tag{5.4}$$

where $k_{HOP} = (2\pi/\hbar)t^2 F_{HOP}$ and t^2 is the square of the overlap integral of the bridge states. The power parameter η depends on the exact conditions of the charge hopping process. For unbiased diffusive hopping it is 2, whereas $1 \leq \eta \leq 2$ for acceptor direction-biased random walk. For donor direction-biased random walk $\eta \geq 2$.

5.2.3 The Parameter β

The parameter β in equation 5.1 for hole transfer is heavily discussed in the DNA charge transfer literature. The first estimates of the Barton group came from experiments utilizing DNA duplexes with hole injectors and acceptors tethered to the 5' termini with relatively long linkers, allowing for multiple intercalation sites. Without monitoring the charge transfer intermediates, it was concluded that DNA must have a small β value ($\beta < 0.2$ Å^{-1}, [1.11](a)).

In other experiments, Brun and Harriman extracted β from noncovalently attached, intercalated donors and acceptors and obtained a value in the range of 0.2 Å^{-1} [5.21]. While these values reported from these two different experiments are in sharp disagreement, a reconciliaton between them is not possible due to poor structural definition of these charge transfer systems.

A more precise definition of the donor/acceptor distance has become possible in oligonucleotides, where the hole injector is either a specific ribose cation [1.13], a covalently attached hole-injecting chromophore [1.16], [5.22] or a nucleobase analogue [5.23] which is capable of acting as a hole-donating species. These newer assays have allowed studies on the dependence of both thermal and photoinduced hole transfer processes on the number of (A,T) pairs separating the donor species and the native guanine base as acceptor.

Table 5.1 summarizes the used donors, acceptors and the monitored measurands.

Donor	Acceptor	Measurand
Ribose cation	GGG	cleavage product yield [1.13]
Acridine-derivate	G	transient fluorescence of excited state [1.16]
Stilbene-derivate	G	transient absorption of intermediates [5.22]
2-aminopurine	G	transient absorption of $G^{\cdot +}$[5.23]

Table 5.1: DNA charge transfer experiments with precise donor-acceptor distances

Despite the different nature of these experiments, both the yield of strand-cleavage products as well as the directly measured hole-injection rate decrease exponentially with the number of (A,T) base-pairs between the hole donor and guanine. As for the value of β, all transfer processes except for the second (acridine-derivate as donor) have yielded $\beta \approx 0.6 - 1$ Å^{-1}.

This β range is larger than that observed for donor/acceptor systems connected by π-conjugated bridges [5.24] and significantly smaller than that for nonspecific electron transfer pathways in proteins [5.25] and rigid aliphatic bridges [5.26] which range between 1 and 1.4 Å^{-1}.

The only exception to this range of β values in DNA arises in the experiments involving DNA duplexes with protonated 9-alkyl-amino-6-chloro-2-methoxy-acridine (ACMA) [5.27] as the intercalated hole donor, where a much steeper distance dependence of 1.5 $\mathring{A}^{-1}$ was observed. In order to utilize this system for charge transfer studies, a detailed investigation of the underlying mechanism is essential.

The large β value reported for ACMA modified DNA duplexes may be system-inherent, and differences in attenuation factors could originate from weak electronic couplings between the hole donor and one or more bridging (A,T) pairs. Moreover, the electronic couplings may be affected by large-amplitude motions of this modified duplex and therefore may be time-dependent.

In addition, some of the energy parameters which govern the hole-transfer rate, such as ΔG and λ_s, may have a distance dependence of their own [1.1], [5.28]. This last hypothesis addresses an inherent problem of electron-transfer theory which, in relation to DNA, has been approached in an explicit way [5.29].

5.3 ACMA-modified Oligonucleotides

Oligonucleotides covalently linked with functional molecules are used in biology as antisense [5.30] and DNA probes [5.31]. These techniques are strongly dependent on intercalating agents which allow specific recognition of a particular base sequence in RNA (single stranded) or DNA. Care must be taken on the stable and well defined intercalation in the oligonucleotide base stacks.

ACMA is of interest as intercalating agent because its fluorescence is quenched when stacked with guanine bases, whereas the other bases have no effect or even enhance the fluorescence quantum yield (for studies on acridine derivatives see for example [5.32]). Figure 5.5 illustrates the schematic structure of the ACMA/oligonucleotides used in this work.

The chromophore is attached to the 3'-phosphate of an abasic site in the oligonucleotide by a proprioamide linker, which is long enough to obtain an optimum interaction with the double stranded structure formed by the oligonucleotide and its complementary sequence [5.33].

It must be kept in mind that ACMA and its derivatives displays complicated photophysics [5.34]. Using steady-state and nanosecond time-resolved fluorescence measurements a pronounced wavelength dependence of the fluorescence decay is reported [5.34](a), that is, a dynamic Stokes shift, which has been assigned to an evironmentally sensitive excited-state ralaxation. The relaxation time scale was solvent- and temperature-dependent, ranging

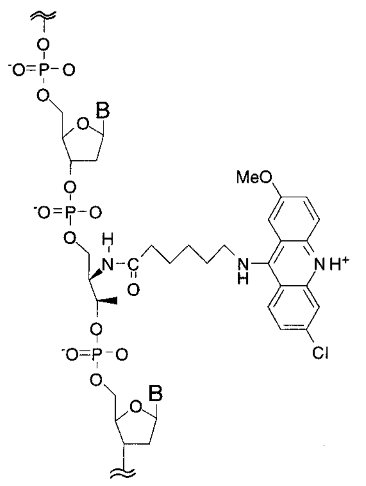

Figure 5.5: Protonated 9-alkyl-amino-6-chloro-2-methoxy-acridine (ACMA) covalently linked to a DNA single strand.

from ≈ 100 ps in glycerol at 10 °C up to 2.5 ns in aqueous solution at room temperature.

The relaxation mechanism was ascribed to the response of the polar solvent cage to an inferred 13 D increase of the moleculest's dipole moment upon excitation [5.34](a). Since in this work excited-state relaxation has been claimed to depend in a specific way on the microenvironment of the chromophore, intercalation of ACMA in the DNA duplex may influence the time scale of this relaxation process.

In the following, the intercalated DNA strands are symbolized by acronyme $\mathbf{X}^+$ and the base sequence in the 5' direction on the strand of the intercalator, for example 3'-$\mathbf{X}^+$-A-G-5' is the symbol for the sequence 3'-...-ACMA-A-G-...-5'.

In figure 5.6 the characteristic absorption and fluorescence spectra of the ACMA/DNA system are shown, which are representative examples for all duplexes studied. The absorption spectrum shows $S_0 \rightarrow S_1$ absorption vibronic bands at 452, 428 and 405 nm, and $S_0 \rightarrow S_2$ vibronic bands at 344 and 328 nm [5.35].

The fluorescence spectrum of ACMA in all duplexes was obtained using excitation at 390 nm, and the spectrum for ACMA intercalated in an all (A,T) base-pair strand (= $\mathbf{X}^+$-(AT)) is shown in figure 5.6(a) as an example. The fluorescence spectrum in all duplexes shows a main peak at 499 nm, and two sidebands at 471 and 530 nm. These sidebands are indicative of intercalation of ACMA into the DNA base stack [5.27].

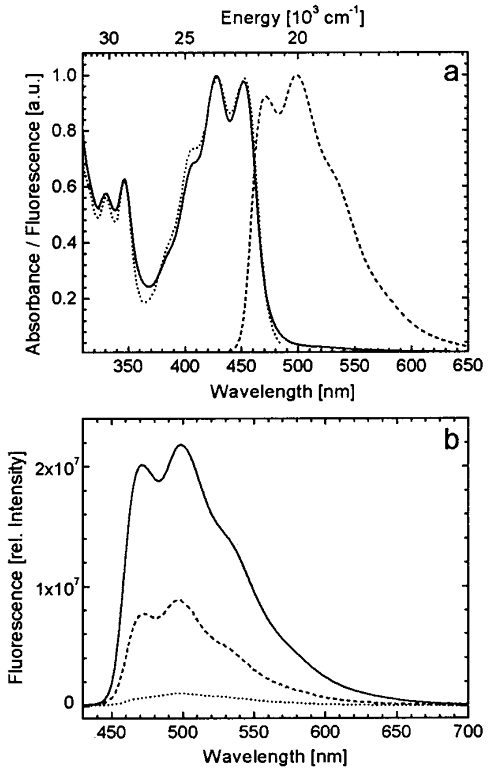

Figure 5.6: (a) Normalized Absorption (solid line), fluorescence emission (dashed line), and fluorescence excitation (dotted line, emission at 500 nm) spectra of ACMA in duplex $\mathbf{X}^+$-(AT) at 283 K. (b) Relative fluorescence intensity measured in duplexes $\mathbf{X}^+$-(AT) (solid line), $\mathbf{X}^+$-G (dotted line) and $\mathbf{X}^+$-A-G (dashed line).

The steady-state fluorescence yield from ACMA was found to be highly dependent upon the nucleobase sequence flanking the chromophore (figure 5.6(b)). Independent of direction along the helix (3' or 5'), almost complete quenching of fluorescence was found for duplex $\mathbf{X}^+$-G, wheras $\mathbf{X}^+$-A-G showed significant fluorescence yields.

In all duplexes, the fluorescence excitation spectra, at both 470 and 500 nm emission wavelengths, closely follow the ACMA absorption spectrum as shown for $\mathbf{X}^+$-(AT).

The CD spectra of all duplexes investigated display a positive band at 280 nm and a negative band at 250 nm, indicative of an overall B-form DNA structure [5.36]. Figure 5.7 shows the duplexes $\mathbf{X}^+$-(AT) (solid line), 5'-$\mathbf{X}^+$-A-G-3' (dotted line), 5'-$\mathbf{X}^+$-A-G-G-3' (dashed line) and 5'-$\mathbf{X}^+$-A-G-G-G-3' (dash-dotted line) as examples, which will be investigated in chapter 5.5.

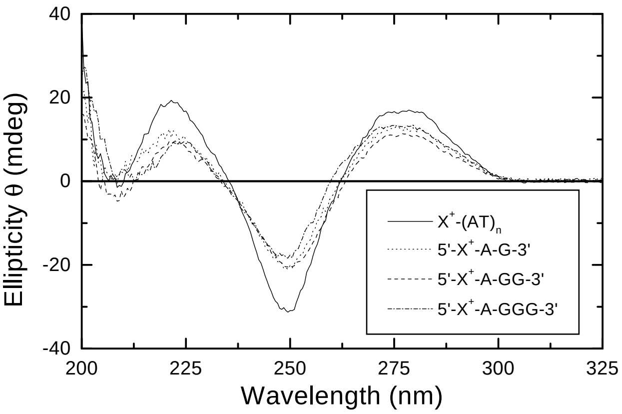

Figure 5.7: Circular dichroism spectra of the duplexes **X**$^+$-(AT) (solid line), 5'-**X**$^+$-A-G-3' (dotted line), 5'-**X**$^+$-A-G-G-3' (dashed line), 5'-**X**$^+$-A-G-G-G-3' (dash-dotted line).

In the visible and near UV, all duplexes have a strong, negative CD band (which is a mirror image to the ACMA $S_0 \rightarrow S_1$ absorption band) and a positive CD band at 350 nm where the $S_0 \rightarrow S_2$ band of ACMA absorbs. Thes features are indicative of a well defined rigid ACMA environment in these duplexes.

5.4 Materials and Methods

5.4.1 Laser Dyes

The laser system and the pump-probe geometry were the same as in the previous chapter. For excitation of DNA samples (at 450 nm) the output of the third harmonic of the Nd:YAG Laser (355 nm) was used to pump the dye laser (filled with Coumarin 120, 0.3 g/l in methanol).

For the probe beam the different wavelengths were generated with the following dyes pumped by the nitrogen laser (337 nm):
Stilbene 3 (0.22 g/l in methanol) for ground-state bleaching at 420 - 430 nm
DCM (0.5 g/l in dimethyl sulfoxide (DMSO)) for excited state absorption between 650 nm and 670 nm

5.4.2 Oligonucleotides

All DNA strands used were obtained from Eurogentec Koeln (Germany), delivered lysophilized after polyacrylamide gel electrophoresis (PAGE) purification. They were stored at -10 °C under the exclusion of light until shortly before use. Stock solutions of complementary single strands were made by dissolving each strand in a 10 mM Na_2HPO_4/NaH_2PO_4, 100 mM NaCl, pH 7.2 buffer solution. These stock solutions were mixed in a 1×10 mm quartz cuvette with a 10 % excess of non-ACMA-modified counter strands present to help ensure that all ACMA chromophores would be located in a DNA duplex.

Hybridization was performed by heating the mixed single strands to 80 °C, followed by slow cooling to room temperature over 2 h. All samples had an adenine base opposite to ACMA on the counter strand. The hybridized spectroscopic samples were stored at 4 °C prior to their characterization.

The samples had optical densities of about 0.3 at 450 nm in a 1-mm-path-length quartz cuvette (concentration 0.3 mM). Steady-state absorption spectra were taken before and after time-resolved measurements to check for sample degradation. Deoxygenation of the samples by purging with argon had no effect on the measured kinetics.

5.5 Hole Trapping by G, GG and GGG

Strand cleavage reactions, induced for instance by piperidine treatment [5.11] (d), (e), [5.37], have shown consistently that multiple guanine tracts in DNA are more susceptible to oxidative damage than isolated guanine bases. This feature has been utilized in long-range hole transport studies [5.38], [5.39] which are based on GGG being a better trap than a single G.

In addition, an orientational dependence of the oxidation site which leads to strand cleavage is observed because the energetics of guanine are dependent upon their immediate environment. In a GG trap, the 5'-guanine is the preferred site for cleavage [5.9](a), [5.10](b),(d),(e), [5.40], [5.41] and in GGG either the 5'- or central guanine is the preferred site of cleavage depending upon the nucleobases immediately neighboring the trap [5.10](b), [5.13](a), [5.37], [5.42], [5.43].

This view of preferred sites of charge localization in GG and GGG traps is supported independently by the quantum mechanical calculations of Voityuk, et al. [5.44]. The interesting question is now whether a distant hole donor populates the preferred cleavage site(s) in either GG or GGG in a direct unistep reaction, or whether a sequential kinetic scheme must be envisioned in which the nearest G is oxidized first, and trapping of the charge at the preferred G occurs in a subsequent step (two step mechanism).

5.5.1 Duplexes under Study

Seven ACMA-modified duplexes with 21 base-pairs were studied with one, two and three guanines separated by an (A,T) base-pair in the 5' and the 3' direction, respectively (table 5.2).

Duplexes $\mathbf{X}^+$-(AT) and 5'-$\mathbf{X}^+$-A-X-Y-Z-3':
5'-GCG TTA TAT A($\mathbf{X}^+$)A **XYZ** TAT GCG-3'

Duplexes 3'-$\mathbf{X}^+$-A-X-Y-Z-5':
5'-GCG TTA **XYZ** A($\mathbf{X}^+$)A TAA TAT GCG-3'

Sequence
$\mathbf{X}^+$-(AT)
5'-$\mathbf{X}^+$-A-G-3'
5'-$\mathbf{X}^+$-A-G-G-3'
5'-$\mathbf{X}^+$-A-G-G-G-3'
3'-$\mathbf{X}^+$-A-G-5'
3'-$\mathbf{X}^+$-A-G-G-5'
3'-$\mathbf{X}^+$-A-G-G-G-5'

Table 5.2: Structure of the $\mathbf{X}^+$ chromophore in a single stranded 21-mer and the studied DNA sequences. An adenine base was placed opposite $\mathbf{X}^+$ in all duplexes similar to those in the studies of Tanaka et al. and all other bases were paired with their normal Watson-Crick complements.

All duplexes were characterized by their steady-state absorption and fluorescence spectra (see figure 5.6) and their CD-spectra (see figure 5.7 for 5'- $\mathbf{X}^+$-A-...-3' duplexes). No significant differences were seen for different directions (5' or 3', respectively).

Photoexcitation of $\mathbf{X}^+$ in all seven duplexes at a wavelength of 450 nm, results in two transient kinetic features. The first feature is the decay of the excited state absorption probed in the spectral region from 570 → 800 nm, characteristic for the absorption of $\mathbf{X}^+$. The second feature is the ground state recovery probed at 425 nm.

In all measurements, both the $\mathbf{X}^+$ absorption and the ground state recovery kinetics were monoexponential with only a small fraction of long lived background signal (< 10 %)

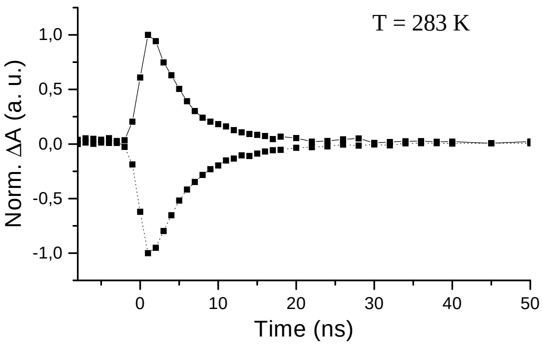

Figure 5.8: Transient absorption kinetics of duplex 3'-$\mathbf{X}^{+}$-A-G-G-5' at 283 K monitoring ground state recovery at 425 nm (dotted line) and excited state decay at 660 nm (solid line) after excitation at 450 nm. Both states evolve on the same time scale and there is no evidence for a long-lived ground state recovery due to trapping by GG. The signals are normalized to $\Delta A_{max} = 1$.

As a representative for all duplexes under study, the transient features of 3'-$\mathbf{X}^{+}$-A-G-G-5' are shown in figure 5.8. The equivalence of the two kinetic traces indicates that the rate determining step in the kinetic scheme (figure 5.9) is the forward hole transfer rate and that charge recombination cannot be resolved.

This phenomenon is a necessary consequence of the high thermal activation of the forward rate and zero or small activation energy for the back transfer [5.46] [1].

Monoexponential rates obtained from least-squares fitting of these data are compiled in table 5.3. The hole transfer rate τ_{HT} was calculated from the formula $1/\tau_{HT} = 1/\tau_{ES} - 1/\tau_0$, where τ_0 is the excited state lifetime of the model duplex $\mathbf{X}^{+}$-(AT). The monoexponentiality together with the structural characterization of Tanaka points to the fact that the acridine must be intercalated in a well defined site.

5.5.2 Hole Transfer in different Directions

If we compare the sequence 5'-$\mathbf{X}^{+}$-A-G-3' with 5'-$\mathbf{X}^{+}$-A-G-G-3' and 5'-$\mathbf{X}^{+}$-A-G-G-G-3' in table 5.3, we observe that the oxidation rates in all cases are similar within a factor of two. In fact, the oxidation of both GG and GGG occurs slightly faster (figure 5.10).

---

[1] In the inverted region, electron transfer reactions usually display small activation energies due to vibronic coupling. See for example [1.1](b), [5.45]

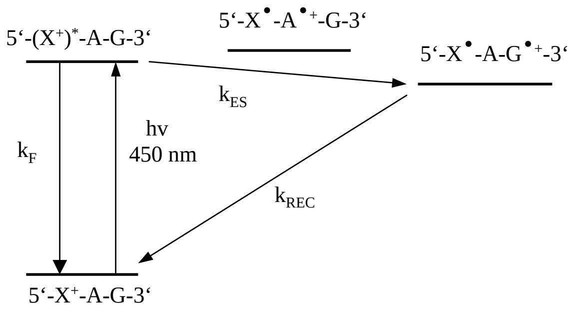

Figure 5.9: Kinetic scheme for the photoinduced hole-transfer reaction in all six duplexes using 5'-**X**$^+$-A-G-3' as an example. k_F is the fluorescence lifetime of the excited chromophore, k_{ES} is the rate of the forward charge-shift reaction, and k_{REC} is the rate of charge recombination. k_{ES} is a highly activated reaction in this duplex leading to $k_{REC} > k_{ES}$, therefore there are no observable intermediate features in the transient absorption data (figure 5.8).

The small variance of two in rates is in line with recent calculations of the energetics of guanines in such combinations [5.44]. Because we do not expect different electronic couplings between **X**$^+$ and the closest guanine, this result indicates that it is this closest guanine which is in all cases the initially oxidized site.

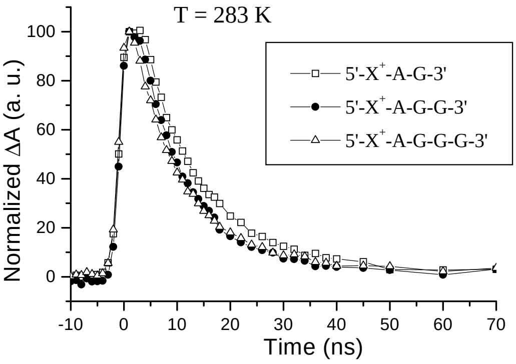

Figure 5.10: Transient absorption kinetics of the duplexes 5'-**X**$^+$-A-G-3' (open squares), 5'-**X**$^+$-A-G-G-3' (filled circles) and 5'-**X**$^+$-A-G-G-G-3' (open triangles) at 283 K monitoring excited state decay at 660 nm after excitation at 450 nm. The signals are normalized to $\Delta A_{max} = 100$.

If we now change the directionality of the hole transfer and compare the sequences 3'-**X**$^+$-A-G-5', 3'-**X**$^+$-A-G-G-5', and 3'-**X**$^+$-A-G-G-G-5' (table 5.3), we observe again that the hole transfer rates are similar, with the oxi-

Duplex	τ_{ES} (ns)	τ_{HT} (ns)
$\mathbf{X}^+$-(AT)	18.0	-
5'-$\mathbf{X}^+$-A-G-3'	12.0 (12.7)	36.0
5'-$\mathbf{X}^+$-A-G-G-3'	8.9 (9.6)	17.6
5'-$\mathbf{X}^+$-A-G-G-G-3'	9.0 (9.4)	18.0
3'-$\mathbf{X}^+$-A-G-5'	6.9 (7.4)	11.2
3'-$\mathbf{X}^+$-A-G-G-5'	4.5 (4.2)	6.0
3'-$\mathbf{X}^+$-A-G-G-G-5'	5.7 (5.3)	8.3

Table 5.3: Measured decay lifetimes of the excited-state decay (τ_{ES}, solid line in figure 5.8) and the calculated hole-transfer lifetimes (τ_{HT}) for all seven duplexes at 283 K. The numbers in parentheses are the measured rates of ground state recovery (dashed line in figure 5.8).

dation rates of GG and GGG being slightly faster. The similarity of the hole transfer rates points to the fact that also in this case the hole accepting site is the proximate G.

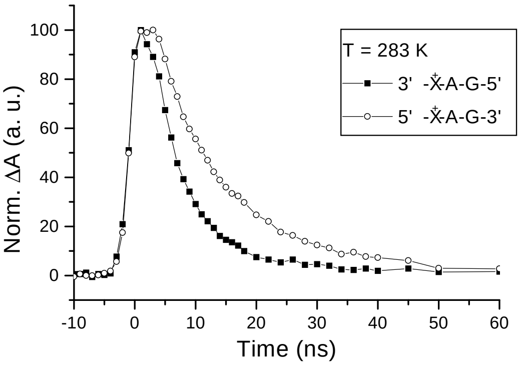

Figure 5.11: Transient difference absorption spectra of the duplexes 5'-$\mathbf{X}^+$-A-G-3' (open circles) and 3'-$\mathbf{X}^+$-A-G-5' (filled squares) at 283 K monitoring excited state decay at 660 nm after excitation at 450 nm. The signals are normalized to $\Delta A_{max} = 100$.

As a final comparison, we look at the differences in rates between 5'-$\mathbf{X}^+$-A-G-3' and 3'-$\mathbf{X}^+$-A-G-5' (figure 5.11) and between their GG and GGG counterparts. What we conclude from the data compiled in table 5.3 is a systematic factor of 3 difference in rates, with transfer in the 3'-$\mathbf{X}^+$-A-...-5' sequences consistently faster.

This result can be rationalized by the difference in electronic coupling between G and A in the two directions of the helix, because 5'-G-A-3' coupling (valid for 3'-**X**$^+$-A-...-5' duplexes) is predicted to be slightly stronger than 3'-G-A-5' coupling (valid for 5'-**X**$^+$-A-...-3' duplexes) [5.47].

However, one caveat on the validity of the theoretical argument is that the difference in rates between the two helical directions could also arise from asymmetrical electronic coupling of the acridine chromophore with the neighboring adenine bases.

5.5.3 Activation Energy

In a second investigation temperature dependent measurements of the forward charge shift rates were performed to derive directly the activation energies of these duplexes. The temperature range studied in pump-probe measurements was 245 - 305 K. Succrose (3.5 M) was added as both a cryoprotector and freezing point depression agent (the samples remained in the liquid phase over the entire temperature range studied).

It should be noted, that in the temperature dependent measurements the buffer solution contained 500 mM NaCl. Mixing buffer and succrose together led to a decrease of the duplex melting points by approximately 6 °C.

However, as can be judged by the invariance of the CD spectra (not shown) and only minor changes of the hole transfer times at 283 K (from 6.9 ns in buffer to 7.9 ns with succrose for 3'-**X**$^+$-A-G-5', figure 5.12) adding succrose to the DNA buffer solutions has no substantial effects on either the binding of the chromophore or on the overall B-form structure of the DNA duplex.

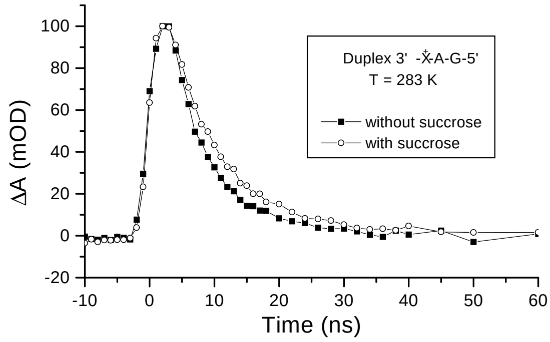

Figure 5.12: Transient difference absorption spectra of the duplex 3'-**X**$^+$-A-G-5' in normal buffer (filled squares, t = 6.9 ns) and with succrose added (3.5 M, open circles, t = 7.9 ns) at 283 K monitoring excited state decay at 660 nm after excitation at 450 nm. The signals are normalized to $\Delta A_{max} = 100$.

Figure 5.13 illustrates the temperature dependence of the excited state decay of 3'-$\mathbf{X}^+$-A-G-5', 3'-$\mathbf{X}^+$-A-G-G-5' and 3'-$\mathbf{X}^+$-A-G-G-G-5' between 255 K and 300 K.

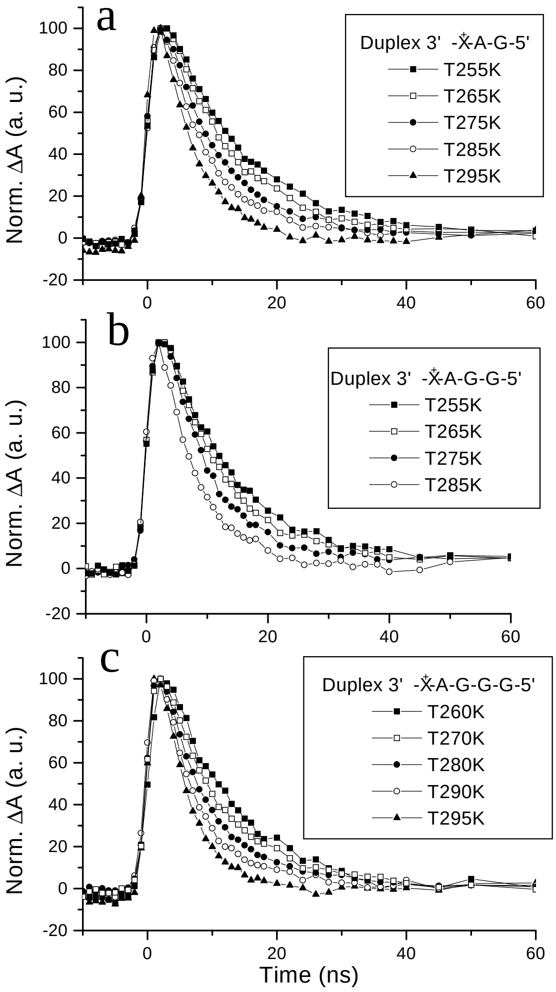

Figure 5.13: Normalized transient difference absorption spectra of the excited state decay of the duplexes 3'-$\mathbf{X}^+$-A-G-5' **(a)**, 3'-$\mathbf{X}^+$-A-G-G-5' **(b)** and 3'-$\mathbf{X}^+$-A-G-G-G-5' **(c)**.

The activation energies E_a are defined in terms of the Marcus equation (equation 5.5).

$$k_{ET}\sqrt{T} = Aexp\left[-\frac{E_a}{k_B T}\right] \tag{5.5}$$

and can be derived from the slope of a linear fit to the natural logarithm of $k_{ET}\sqrt{T}$ (figure 5.14).

We can clearly see a slowing down of the charge transfer process with decreasing temperature. As a consequence the fluorescence recovers at lower

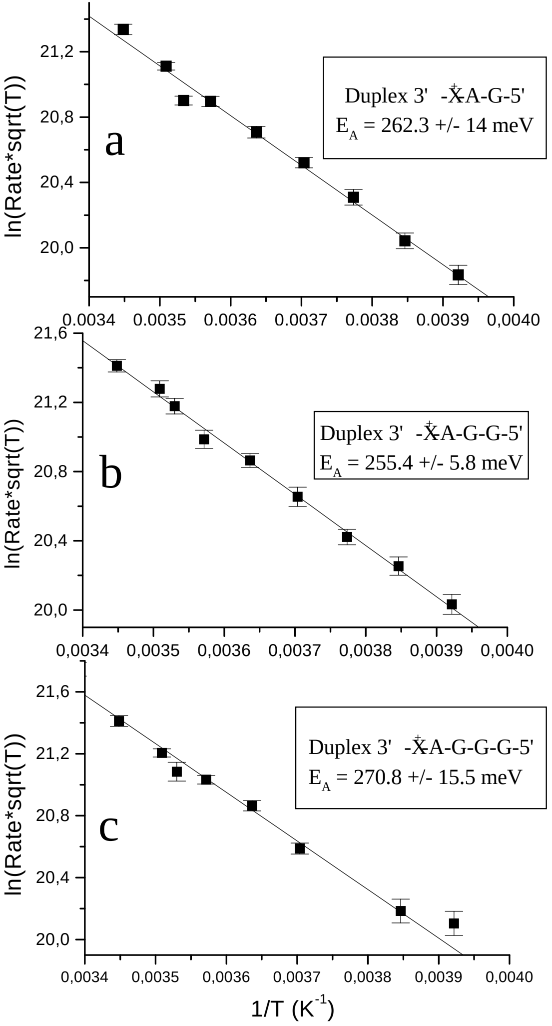

Figure 5.14: Natural logarithm of $k_{ET}\sqrt{T}$ derived from temperature dependent measurements on the duplexes under study.

temperature. As an example, figure 5.15 shows the steady-state fluorescence spectra (excitation wavelength at 410 nm) of the duplex 3'-$\mathbf{X}^{+}$-A-G-5' showing no quenching at 240 K (no charge transfer) and significant quenching at higher temperatures (charge transfer).

The sharpening of the fluorescence spectrum, in particular of the shoulders around 471 nm and 530 nm is a characteristic feature for all ACMA-modified duplexes in a buffer/succrose solvent below freezing point.

The important outcome is, that the activation energies of all three duplexes differ only sligthly. Taking the arithmetic average of the three activation energies, we obtain the result **262.8 ± 23.5 meV**, where 23.5 meV is the value of the highest deviation from the arithmetic average.

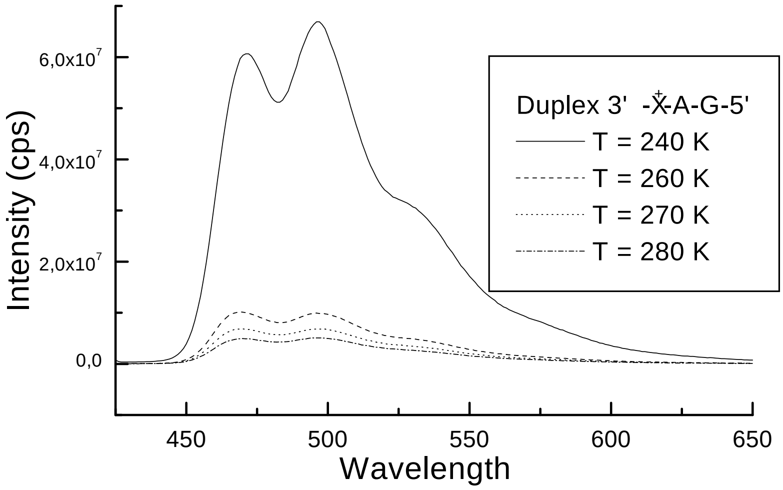

Figure 5.15: Steady-state fluorescence spectra of the duplex 3'-$\mathbf{X}^+$-A-G-5' at different temperatures with excitation at 410 nm

5.5.4 Conclusions

Since the G proximal to a hole injection site in GGG tracts is initially populated, there must be a subsequent process which leads to long-lived hole trapping in GGG. This process is expected to involve charge transfer as a consequence of structural and energetic relaxation. This entire process is what we refer to as the trapping reaction in GGG.

The lifetime data reported in table 5.3 are in excellent agreement with the yield data of a reduced hole donor described recently [1.13]. In these experiments the donor species is the enolether radical cation.

The results of our study may add an important detail to the understanding of this trapping reaction. We postulate that the lower energetics, characteristic of GG, are the result of an intraguanine tract-relaxation process subsequent to the primary oxidation kinetics.

The order of magnitude similarity between other hopping rates (see for example Lewis et al. [5.48]) to that extracted from a detailed model [5.49] of the chemical yield experiments [1.13], [5.38] confirms the validity of the chemical yield approach to measuring charge transfer rates in DNA. In addition, it is rewarding to see that direct kinetic measurements and the dynamics modeled from chemical yield data support each other.

5.6 Distance dependent Activation Energies

In a recent publication the distance dependence of charge transfer rates was studied by femtosecond time-resolved pump-probe spectroscopy [5.46]. The kinetics of photoinduced charge transfer was monitored in duplexes with a guanine directly neighbouring the chromophore and when $\mathbf{X}^+$ was separated by one and two (A,T) pairs in both directions.

The relevant kinetic parameters could be derived from the observation of (i) the decay of the photoexcited chromophore $^1(\mathbf{X}^+)^*$, (ii) the formation of the intermediate radical state $\mathbf{X}^\bullet$ and (iii) the recovery of the ground state. As in the previous investigation all spectral features were identical for the 3'- and 5'-direction, respectively. The lifetimes of the excited state and the radical state are of the same order of magnitude with rates in the 3'-$\mathbf{X}^+$-duplexes consistently larger than those in the 5'-$\mathbf{X}^+$-duplexes.

In the case of nearest neighbours, the intermediate radical state $\mathbf{X}^\bullet$ is formed within 4 ps and decays in 30 ps. In $\mathbf{X}^+$-A-G with one (A,T) base-pair between the $\mathbf{X}^+$ and guanine slows down the forward transfer rate by 2900. If the β value is extracted from these two data points where one of them applies to direct contact an the other one to superexchange mediated transfer, an unphysically large β of 2.3 Å^{-1} would result which is even higher than the 1.5 Å^{-1} value reported by Fukui et al.

This fact is also supported by the observation of no fluorescence quenching in $\mathbf{X}^+$-A-A-G, which indicates that the hole transfer rate must be much slower than the 18 ns excited lifetime of $\mathbf{X}^+$ in $\mathbf{X}^+$-(AT).

This cannot be solely due to the electronic coupling V in the $\mathbf{X}^+$ labeled DNA duplexes. Rather, it is a fingerprint of two superimposed effects: a decrease of the superexchange-mediated electronic coupling V which is accompanied by a growing-in of the activation energy with increasing $\mathbf{X}^+$-G distance.

This explanation is consistent with the finding, that in the system $\mathbf{X}^+$-A-G the product state $\mathbf{X}^\bullet$ is not observed, which is indicative of a fast (less activated) back transfer rate (recombination k_{REC}) as compared to the forward rate (excited state decay k_{ES}). It was concluded, that there are two hole-transfer regimes which differ with respect to the activation energy of the forward rate: for the direct contact system k_{REC} exceeds k_{ES}, while the opposite is true for the duplex $\mathbf{X}^+$-A-G.

To test this hypothesis of distance-dependent activation energy, in a first step guanine has been replaced by its easier to oxidize purine analogue 7-deaza-guanine (Z, see figure 5.16 for structure).

In these duplexes, a similar change of charge transfer mechanism is found. However, this change occurs at a larger donor/acceptor distance than in the

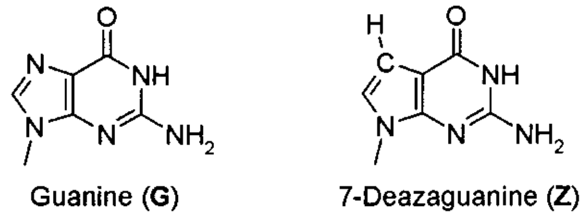

Figure 5.16: Structures of guanine (G) and its easier to oxidize purine analogue 7-deaza-guanine (Z)

system with guanines, which is consistent with an a priori larger driving force.

5.6.1 Results

In all following investigations we restrict ourselves to 3'-...-$\mathbf{X}^+$-...-5' duplexes, so that direction indices can be ommitted. All measurements were carried out with the same conditions as in chapter 5.5. As before, the steady-state properties (absorption, fluorescence and CD spectra) of all duplexes under study remained unchanged after succrose addition with only slightly increase of the hole transfer times. All curves were monoexponential with only a small fraction of longer lived offset (< 10 %).

To illustrate the temperature dependences of the duplexes $\mathbf{X}^+$-Z, $\mathbf{X}^+$-A-Z and $\mathbf{X}^+$-A-A-Z, figure 5.17 shows their transient kinetics on both the sub-nanosecond and the nanosecond time scale.

For the duplexes $\mathbf{X}^+$-Z, $\mathbf{X}^+$-A-Z and $\mathbf{X}^+$-G the formation and decay of the intermediate radical $\mathbf{X}^\bullet$ could be monitored in the wavelength region from 500 nm to 530 nm [5.50]. The radical formation and decay after excitation at 450 nm and probing at 500 nm is shown in figure 5.17 **(a)** for the duplex $\mathbf{X}^+$-Z.

Figure 5.18 illustrates the temperature dependence of the forward charge shift rate constants of the duplexes $\mathbf{X}^+$-Z, $\mathbf{X}^+$-A-Z and $\mathbf{X}^+$-A-A-Z.

Forward and backward charge shift rates and the corresponding activation energies for duplexes with the bases Z and G (transient kinetics not shown) are compiled in table 5.4.

Each successive insertion of an (A,T) pair between $\mathbf{X}^+$ and G or Z leads to an increase in the activation energy for forward charge shift of about 0.1 eV (table 5.4). [2]

---

[2] In the absence of hole injection (duplex $\mathbf{X}^+$-(AT)), the $\mathbf{X}^+$ excited state lifetime of 18 ns was observed to be independent of temperature over the range studied.

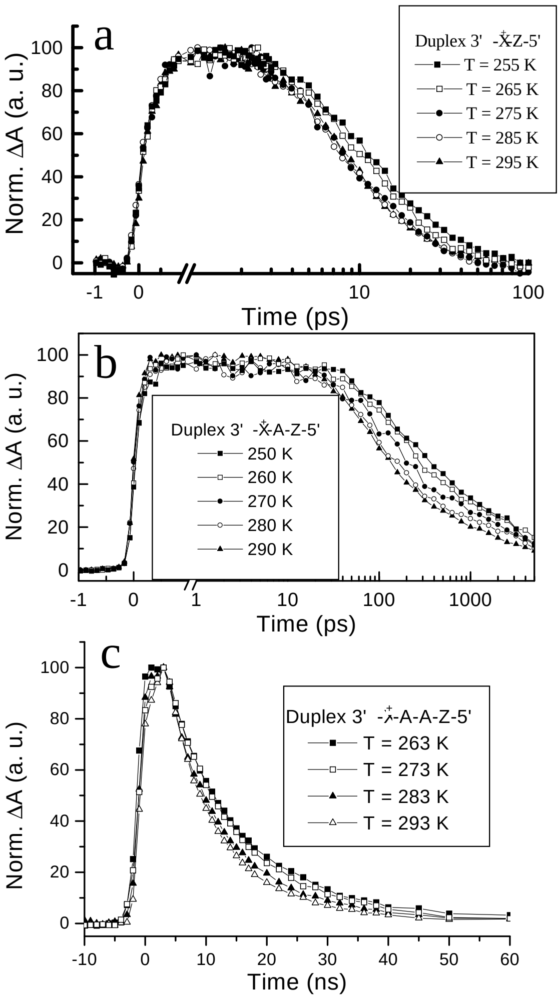

Figure 5.17: Normalized transient difference absorption spectrum of the duplexes $\mathbf{X}^+$-Z **(a)** (excitation at 450 nm, probe at 500 nm), $\mathbf{X}^+$-A-Z **(b)** and $\mathbf{X}^+$-A-A-Z **(c)** (excitation at 450 nm, probe at 660 nm).

The small difference in activation energy for $\mathbf{X}^+$-A-G compared to the measurements in chapter 5.6 could be due to some noise and the different NaCl-concentration (100 mM) The difference will neither change the results of the discussion below nor will it affect our conclusions.

In contrast, the activation energies for backward charge shift (recombination) show a somewhat weaker distance dependence which explains why in $\mathbf{X}^+$-A-G and $\mathbf{X}^+$-A-A-Z only the forward charge shift is observable.

We thus conclude that the anomalously steep distance-dependence of hole injection rates in $\mathbf{X}^+$/DNA duplexes carrying zero, one or two (A,T) pairs between $\mathbf{X}^+$ and G or Z, is dominated by distance-dependent activation energies.

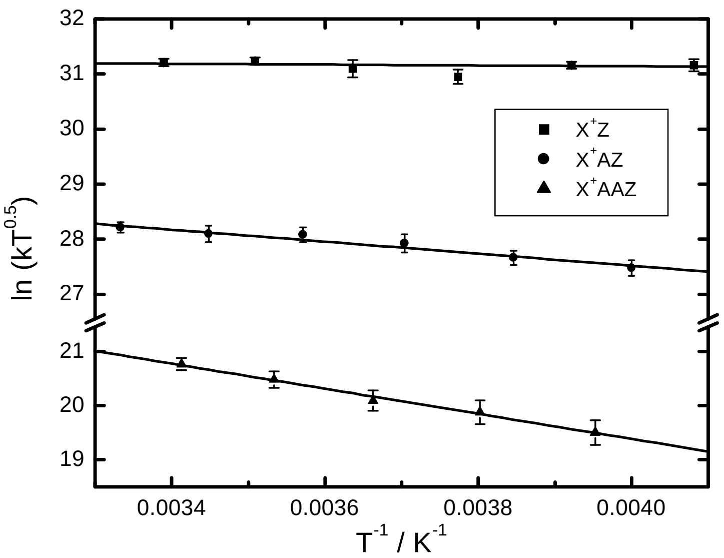

Figure 5.18: Effect of temperature on the natural logarithm of $k_{ET}\sqrt{T}$ for the forward charge shift in **X**$^+$-Z, **X**$^+$-A-Z and **X**$^+$-A-A-Z (see legend)

Duplex	$k_{ES}[s^{-1}]$	E_a [eV]	$k_{REC}[s^{-1}]$	E_a [eV]
X$^+$-G	2.0×10^{11}	0.08 ± 0.04	1.9×10^{10}	0.14 ± 0.02
X$^+$-A-G	6.5×10^{7}	0.20 ± 0.04	-	-
X$^+$-Z	2.0×10^{12}	< 0.015	1.0×10^{11}	0.08 ± 0.01
X$^+$-A-Z	9.3×10^{10}	0.09 ± 0.01	6.9×10^{9}	0.13 ± 0.02
X$^+$-A-A-Z	4.6×10^{7}	0.20 ± 0.02	-	-

Table 5.4: Forward and backward hole transfer rates k_{ES} and k_{REC} at 283 K and the corresponding activation energies.

5.6.2 Discussion

We restrict our analysis to the activated hole injection reactions and employ the classical Marcus expression [1.1]:

$$E_a = \frac{(\Delta G + \lambda)^2}{4\lambda} \tag{5.6}$$

This relates E_a to the thermodynamic driving force ΔG and the reorganization energy λ, which in the present situation is due primarily to the medium contribution λ_s (see below). Equation 5.6 is a useful starting point since quantum effects are expected to be small in the Marcus normal region

($-\Delta G < \lambda$) near room temperature. [3]

This behavior is in contrast to the back transfer reactions, which occur under strongly exergonic conditions in the inverted regime. For these latter reactions, a quantum mechanical treatment of the vibrational degrees of freedom is essential. It is well known that distance-dependent activation energies can arise from the distance-dependence of both on purely electrostatic grounds [1.1], [5.28].

An important simplification in the present situation is that for charge shift reactions ΔG is expected to have little or no distance-dependence, in contrast to the situation for charge separation reactions. Therefore, E_a for charge shift reactions should normally be distance-dependent due solely to λ_s.

Recent measurements of the temporal evolution of the fluorescence spectrum in a ACMA-labeled duplex on the 100 fs to 50 ps time scale allow us to exclude a distance-dependent change of ΔG [5.51], in contrast to $\mathbf{X}^+$ analogs in free solution which can display picosecond to nanosecond excited state relaxation [5.34]. Thus, we attribute the present distance-dependent activation energy solely to the reorganization energy.

In the absence of absolute values for ΔG, the present analysis will start from a comparison of E_a values for the systems $\mathbf{X}^+$-A-G and $\mathbf{X}^+$-A-Z, assuming the oxidation potential of the easier-to-oxidize Z to be separated from G by $\Delta\Delta G = \Delta G_{X-A-G} - \Delta G_{X-A-Z} \approx 0.3$ eV. This estimate has been previously reported for isolated DNA bases in solution [5.52].

Utilizing ΔG_{X-A-G} = -0.15 eV and ΔG_{X-A-Z} = -0.45 eV, a fit of equation 5.6 to the corresponding E_a values in table 5.4 provides a range of permissible values: $0.85 \text{ eV} \leq \lambda \leq 1.20$ eV [4]. Importantly, the calculated reorganization energy seems to be mainly dependent on the donor acceptor distance and almost independent of the nature of the hole acceptor, G or Z.

Applying the above values of ΔG to $\mathbf{X}^+$-G and to $\mathbf{X}^+$-A-A-Z yields, respectively, $\lambda = 0.6 \pm 0.1$ and $\lambda = 1.6 \pm 0.1$ eV. Extending this procedure to $\mathbf{X}^+$-Z is problematic, since the (almost) zero activation energy does not allow one to discriminate between an activationless or (slightly) inverted charge shift reaction.

However, assuming that hole injection in $\mathbf{X}^+$-Z can be treated within the classical Marcus formalism (equation 5.6), one obtains $\lambda = 0.6 \pm 0.1$ eV, in good agreement with $\mathbf{X}^+$-G. In view of the uncertainties associated with the experimental estimate of ΔΔG = 0.3 eV, it should be explicitly stated that

---

[3] Entropy contributions to ΔG and λ are assumed to be negligible.

[4] A variation of $\pm\delta$ in the ΔG values, maintaining $\Delta\Delta G = 0.3$ eV, yields a variation of $\pm 2\delta$ in the fitted λ values

only a small range of ΔΔG values, 0.15 - 0.3 eV, leads to self consistent fits of the type cited above.

The λ values estimated above contain, of course, a contribution from molecular (λ_v) as well as medium (λ_s) modes. Since λ_v is not expected to depend appreciably on donor-acceptor separation, and since the overall λ for the "contact" cases studied here ($\mathbf{X}^+$-G and $\mathbf{X}^+$-Z) is estimated to be rather small (≈ 0.5 eV), we conclude that λ_v is also likely to be quite small (a few tenths of eV), a result consistent with previous work showing that for an organic donor-acceptor pair, λ_v can be as small as 0.1 eV [5.53].

We also considered the extent to which the full quantum mechanical λ_v is likely to contribute to the activation energy. Calculations using the semiclassical electron transfer model of Bixon and Jortner [5.54] indicate that this contribution is small [5], and the λ estimates cited above can be taken as being dominated by λ_s.

The magnitude of λ_s, as well as the degree of distance-dependence, relies on a number of factors including the effective size of the donor and acceptor sites, their effective separation distance, and the effective polarity of their environment [1.1].

5.6.3 Conclusions

It was shown by direct temperature dependent measurements of the activation energies for a series of ACMA-modified DNA duplexes with donor-acceptor separations from 4 to 11 Å, that the charge transfer in these duplexes can be explained within the framework of a distance dependent reorganization energy. The increase in activation energy is a result of distance-dependent changes in the energetics, predominately of the medium reorganization energy on purely electrostatic grounds.

With increasing donor-acceptor distance the charge transfer mechanism changes from a nearly activationless to a thermally activated regime. The forward transfer becomes slower than the back transfer due to the increase in activation energy and the decrease in electronic coupling. Because of this combined effect the radical intermediate $\mathbf{X}^\bullet$ can no longer be detected.

---

[5] Even in the normal region there is some degree of nuclear tunneling associated with the high frequency modes. This means the term λ in equation 5.6 may be viewed as an effective λ corresponding to the sum of λ_s and some fraction α of λ_v: $\lambda_{eff} = \lambda_s + \alpha\lambda_v$. Model semiclassical calculations, based on the method of ref [5.53] (effective vibrational frequency of 1500 cm^{-1} and λ_v values ranging from 0.1 - 0.4 eV) only require α values of $\sim$ 5 - 20 % for the systems in the normal region ($\mathbf{X}^+$-G, $\mathbf{X}^+$-A-G, $\mathbf{X}^+$-A-Z and $\mathbf{X}^+$-A-A-Z to obtain equivalence between the semiclassical E_a values and their classical counterparts (equation 5.6).

The increase of ∼1 eV as the donor-acceptor distance changes from ∼4 Å(contact) to ∼11 Å(two intervening (A,T) base-pairs) is consistent with recent model calculations of λ_s in duplex DNA based on considerations of the dielectric heterogeneity of the surrounding medium [5.29]. The results specifically referred to there were for an unmodified DNA duplex in which two of the DNA bases served as donor and acceptor sites.

Quantitative modeling of λ_s for the present DNA duplexes would require detailed information about the structure of the $\mathbf{X}^+$-chromophore in its binding site, including also any specific perturbations of the DNA structure.

It is still an open question as to the contribution of distance-dependent activation energies to the hole-transfer kinetics measured for other DNA-based systems [5.23], [5.55]. In general, distance-dependent activation energies for ET in molecular donor/acceptor systems may be expected if the medium reorganization energy λ_s is appreciable, if the charge-transfer step is relatively short-range (i. e., occurring over $\leq$ 10 - 15 Å) and if the driving force is in the normal region ($-\Delta G < \lambda$) of the Marcus expression, equation 5.6 (for related effects in the inverted region, see for example [5.56]).

Chapter 6

Summary

6.1 Electron Transfer in the Ferrocenophanone-Oxazine-1 System

Small aromatic molecules like pyrimidine are not easily detectable by UV/VIS spectroscopy. The spectral region can be extented by time-resolved IR spectroscopy on carbonyl bonds which are sensitive for the vibrational Stark-effect. As a model system, the photoinduced redox reaction of ferrocenophanone as electron donor and oxazine-1 as electron acceptor was investigated.

The selective observation of suitable transitions requires a source of ultrashort IR pulses with wavelengths tunable in the 1650 - 1750 cm^{-1} range which was achieved by nonlinear three wave mixing in a home-built two-step OPG/OPA-system.

With the help of a 30 cm focal length monochromator a spectral width of 3 cm^{-1} was obtained. The pump-probe cross-correlation width was estimated to be approximately 200 fs (FWHM) from pump-probe experiments on a thin Si-wafer.

The transient absorption spectrum after photoexcitatiton of oxazine-1 at 650 nm showed a fast wavelength shift which is in agreement with the steady-state IR spectrum of chemically oxidized ferrocenophanone and with theoretical predictions.

The time dependence of the difference absorption signal after excitation of oxazine-1 can be fitted with a rise time of 370 fs, a decay time of 5.8 ps and a constant offset convoluted with a gaussian experimental response function with 200 fs FWHM. The transients are fully compatible with the charge transfer dynamics observed by optical spectroscopy.

6.2 Investigation of the heterogenous System **Mc3**/TiO_2

We performed both steady-state and time-resolved absorption and fluorescence measurements on the dye Mc3 which may be interesting for its use in photoelectrochemical cells. The photophysical properties of Mc3 in different solvent compositions and at different pH-values were investigated. The steady-state absortption showed a bathochromic shift of the maximum wavelength from 561 nm to 592 nm with increasing polarity (i. e. increasing water/ethanol ratio) of the solvent. At high water/ethanol ratios the dye tends to form dimers only at low pH-values (pH < 3).

In the water/ethanol/glycerol = 32/8/60 solvent (selected to obtain a good optical glass at low temperatures), the dye showed no aggregation effect at room temperature. However, below freezing temperature the formation of dimers was obvious from the appearance of a new blue shifted band with maximum at 558 nm which was concentration dependent and from an isosbestic point at 564 nm.

In the presence of TiO_2 nanoparticles a red shift by 12 nm of the monomeric band in the steady-state absorption spectrum was observed, which is due to adsorption on the surface. We further observed the appearance of a broad band with maximum at 550 nm which was even further blue shifted than the dimeric band shifted to 534 nm after glycerol addition. The relative amplitude and the maximum wavelength of this H-aggregation band were clearly concentration dependent.

This is due to adsorption and a higher order aggregation (H-aggregates) of the dye molecules on the semiconductor surface. The fluorescence of all bands was strongly quenched by more than two orders of magnitude, which points to efficient adsorption of the dye molecules on the colloid surface and fast electron injection.

In the transient measurements we observed dispersive kinetics for both ground-state recovery and cation decay from nano- to microsecond time scales with evidence for significant sub-nanoscond contributions. Excitation at different wavelengths showed different kinetic decay times for the different species with the H-aggregates exhibiting faster ground state recovery. The kinetic curves could be satisfactorily reproduced by both the random walk and the random flight model.

Transient signals caused by triplets or a magnetic field effect on the recombination signal could not be observed. This is most probably due to a fast spin-lattice relaxation in TiO_2.

6.3 Activated Hole Transfer in Acridine Modified DNA

We investigated the charge shift dynamics between the hole donor 9-alkyl-amino-6-chloro-2-methoxy-acridine (ACMA) covalently attached at an artificial abasic site of a 21-base-pair duplex and the native base G or its easier-to-oxidise analogue Z by using nanosecond time-resolved pump-probe absorption spectroscopy.

After photoexcitation at 450 nm of the duplexes 3'-$\mathbf{X}^+$-A-G-5', 3'-$\mathbf{X}^+$-A-G-G-5' and 3'-$\mathbf{X}^+$-A-G-G-G-5' and their counterparts in the 5'-...-3' direction we investigated the kinetic features of the transient signals of hole transfer from the chromophore $\mathbf{X}^+$ to either a G, GG or GGG site by monitoring (i) the excited state decay with probe wavelength at 660 nm and (ii) the ground state recovery at 425 nm probe wavelength.

We observed, that the oxidation rates in all cases are similar to within a factor of two, which is in line with recent calculations. Due to the high thermal activation energy for the forward hole transfer rate and a zero or small activation energy for the back transfer, the signal of the radical intermediate $\mathbf{X}^{\bullet}$ and the charge recombination could not be resolved.

Activation energies for these duplexes were obtained by temperature dependent measurements of the forward charge shift rates. The activation energies for all three duplexes differed only slightly, and a value of $E_a = 262.8 \pm 23.5$ meV could be derived by application of the classical Marcus equation. We concluded, that the proximal G is initially populated, and that there must be a subsequent process which leads to hole trapping in GG or GGG.

Recent investigations of the apparently anomalous attenuation factor ($\beta > 1.5$ Å^{-1}) led to the conlusion that in addition to the electronic couplings, the activation energies must also be distance dependent.

With increasing donor-acceptor distance the charge transfer mechanism changes from a nearly activationless to a thermally activated regime. Each successive insertion of an (A,T) pair between $\mathbf{X}^+$ and G or Z leads to an increase in the activation energy for forward charge shift of about 0.1 eV.

It was shown that the charge transfer in the ACMA-modified duplexes can be explained within the framework of a distance dependent reorganization energy due to electrostatic grounds. The fit of the experimental data of the transient kinetics for G or Z at different donor-acceptor distances yielded an increase from $\lambda = 0.6 \pm 0.1$ eV for ~ 4 Å to $\lambda = 1.6 \pm 0.1$ eV for ~ 11 Å. This corresponds to a lower limit for the medium reorganization energy of about 0.8 eV at 10 Å donor-acceptor distance.

Bibliography

[Chapter 1]

[1.1] (a) Marcus, R. A.; J. Chem. Phys. 1956, 24, 966
(b) Marcus, R. A.; Sutin, N.; Biochim. Biophys. Acta 1985, 811, 265

[1.2] (a) Jortner, J.; J. Am. Chem. Soc. 1980, 102, 6676
(b) Jortner, J.; Biochim. Biophys. Acta 1980, 594, 193

[1.3] (a) Fleming, G. R.; Chemical Apllications of Ultrafast Spectroscopy. Oxford University Press, Clarendon Press, New York, Oxford, 1986
(b) Manz, J.; Woeste, L.; Ed. Femtosecond Chemistry. VCH Weinheim, New York, Basel, Cambridge, Tokyo, 1995

[1.4] (a) Bixon, M.; Jortner, J.; Michel-Beyerle M. E.; In: Perspectives of photosynthesis; Jortner, J.; Oullman, B.; Ed.; Kluwer Acad. Publ.: Netherlands, 1990, 325
(b) The Photosynthetic Reaction Center; Deisenhofer, J.; Norris, J. R.; Ed.; Academic Press: New York, 1993

[1.5] (a) Burrows, C. J.; Muller, J. G.; Chem. Rev. 1998, 98 1109
(b) Armitage, B.; Chem. Rev. 1998, 98, 1171

[1.6] (a) Taylor J. S.; Acc. Chem. Res. 1994, 27, 76
(b) Taylor J. S.; J. Chem. Educ. 1990, 67, 835
(c) Begley, T. P.; Acc. Chem. Res. 1994, 27, 394
(d) Heelis, P. F.; Hartmann, R. F.; Rose. S. D.; Chem. Soc. Rev. 1995, 289
(e) Carell, T.; Angew. Chem. 1995, 107, 2697 and Angew. Chem. Int. Ed. Engl. 1995, 34, 2491

[1.7] Sancar, A.; Biochemistry 1994, 33, 2

[1.8] Elsaesser, T.; Fujimoto, J. G.; Wiersma, D. A.; Zinth, W.; Eds. Ultrafast Phenomena XI.; Springer Verlag: Berlin, Heidelberg, New York, 1998

[1.9] (a) Bloembergen, N.; Nonlinear Optics; Benjamin, New York 1965
(b) Mewell, A.; Moloney, J. V.; Nonlinear Optics; Addison-Wesley, Reding, MA 1992
(c) Mills, D. L.; Nonlinear Optics; Springer, Berlin, Heidelberg 1991

[1.10] O'Regan, B.; Graetzel, M.; Nature 1991, 353, 737

[1.11] (a) Murphy, C. J.; Arkin, M. R.; Jenkins, Y.; Ghatlia, N. D.; Bossmann, S. H.; Turro, N. J.; Barton, J. K.; Science 1993, 262, 1025
(b) Murphy, C. J.; Arkin, M. R.; Ghatlia, N. D. Bossmann, S. H.; Turro, N. J.; Barton, J. K.; Proc. Natl. Acad. Sci. U.S.A. 1994, 91, 5315
(c) Arkin, M. R.; Stemp, E. D. A.; Holmlin, R. E.; Barton, J. K.; Hoermann, A.; Olson, E. J. C.; Barbara, P. F.; Science 1996, 273, 475
(d) Turro, N. J.; Barton, J. K.; J. Biol. Inorg. Chem. 1998, 3, 201

[1.12] Jortner, J.; Bixon, M.; Langenbacher, T.; Michel-Beyerle, M. E.; Proc. Natl. Acad. Sci. U.S.A. 1998, 95, 12759

[1.13] Meggers, E.; Michel-Beyerle, M. E.; Giese, B.; J. Am. Chem. Soc. 1998, 120, 12950

[1.14] (a) Hartwich, G.; Caruama, C. J.; de Lumley-Woodycar, T.; Wu, Y.; Campbell, C. N.; Heller, A.; J. Am. Chem. Soc. 1999, 121, 10803
(b) Lisdat, F.; Ge, B.; Scheller, F. W.; Electrochem. Commun. 1999, 1, 65
(c) Boon, E. M.; Ceres, D. M.; Drummond, T. G.; Hill, M. G.; Barton, J. K.; Nature Biotechnol. 2000, 18, 1096

[1.15] (a) Braun, E.; Eichen, Y.; Sivan, U.; Ben-Joseph, G.; Nature 1998, 391, 775
(b) Fink, H.-W.; Schoenenberger, C.; Nature 1999, 398, 407
(c) Porath, D.; Bezryadin, A.; De Vries, S.; Dekker, C.; Nature 2000, 403, 635

[1.16] Fukui, K.; Tanaka, K.; Fujitsuka, M.; Watanabe, A.; Ito, O.; J. Photochem. Photobiol. B 1999, 50, 18

[**Chapter 2**]

[2.1] Poellinger-Dammer, F.; Musewald, C.; Heitele, H.; Michel-Beyerle M. E.; Anders, M.; Futscher, M.; Voit, G.; Staab, H. A.; Ber. Bunsenges. Phys. Chem. 1996, 100, 2076

[2.2] Musewald, C.; PhD-thesis, TU-Muenchen 1999

[2.3] Salin, F.; Estable, F.; Saviot, F.; in: Tunable femtosecond sources and optical parametric generators, Barbara, P. F.; Knox, W. H.; Mourou, G. A.; Zewail, A. H. (Eds.); Springer-Verlag Berlin, 1994, page 194

[2.4] a) Heise, H. M.; Schroetter, H. W.; in: Infrared and Raman Spectroscopy; Schrader B. (Ed.); VCH Publ., Inc., New York 1995, p. 273ff
b) Dalby F. W.; Nielsen, H. H.; J. Chem. Phys. 1956, 25, 934

[2.5] Volk, M.; Aumeier, G.; Haeberle, T.; Ogrodnik, A.; Michel-Beyerle, M. E.; Biochim. Biophys. Acta 1992, 1102, 253

[2.6] Volk, M.; Diploma thesis, TU Muenchen 1986

[2.7] Haeberle, T.; Diploma thesis, TU Muenchen 1991

[**Chapter 3**]

[3.1] (a) Friedberg, E. C.; Walker, G. W.; Siede, W.; DNA Repair and Mutagenesis, ASM Press, Washington, 1995
(b) Lindahl, T.; Nature (London) 1993, 362, 709
(c) Hutchinson, F.; Photochem. Photobiol. 1987, 45, 897

[3.2] Li, Y. F.; Kim, S. T.; Sancar, A.; Proc. Natl. Acad. Sci. U.S.A. 1993, 90, 4389

[3.3] (a) Sancar, A.; Smith, F. W.; Sancar, G. B.; J. Biol. Chem. 1984, 259, 6028
(b) Sancar, G, , Smith, F. W.; Lorence, M. C.; Rupert, C. S.; Sancar A.; J. Biol. Chem. 259, 6033
(c) Jorns, M. S.; Sancar, G. B.; Sancar, A.; Biochemistry 1984, 23, 2673
(d) Iwatsku, N.; Joe, C. D.; Werbin, H.; Biochemistry 1980, 19, 1172
(e) Eker, A. P. M.; Hessels, J. K. C.; van de Velde, J.; Biochemistry 1988, 27, 1758

(f) Johnson, J. L.; Hamm-Alvarez, S.; Payne, G.; Sancar, G. B.; Rajagopalan, K. V.; Sancar, A.; Proc. Natl. Acad. Sci. U.S.A. 1988, 85, 2046

[3.4] (a) Aubert, C.; Vos, M. H.; Mathis, P.; Brettel, K.; Nature 2000, 405, 586
(b) Popovic, D. M.; Zmiric, A.; Zaric, S. D.; Knapp, E. W.; J. Am. Chem. Soc. 2002, 124, 3775
(c) Antony, J.; Medvedev, M.; Stuchebrukhov, A. A.; J. Am. Chem. Soc. 2000, 122, 1057

[3.5] Carell, T.; Epple, R.; Gramlich, V.; Angew. Chem. 1996, 108, 676

[3.6] (a) Heelis, P. F.; Kim, S. T.; Okamura, T.; Sancar, A.; J. Photochem. Photobiol. B 1993, 17, 219
(b) Kim, S. T.; Heelis, P. F.; Okamura, T.; Hirata, Y.; Mataga, N.; Sancar, A.; Biochemistry 1991, 30, 11262
(c) Langenbacher, T.; Zhao, X.; Bieser, G.; Heelis, P. F.; Sancar A.; Michel-Beyerle, M. E.; J. Am. Chem. Soc. 1997, 119, 10532

[3.7] Wasielewski, M. R.; Chem. Rev. 1992, 92, 435

[3.8] Bauscher, M.; Maentele, W.; J. Am. Chem. Soc. 1992, 96, 11101

[3.9] Goldman, A. S.; Krogh-Jespersen, K.; J. Am. Chem. Soc. 1996, 118, 12159

[3.10] (a) Schoonover, J. R.; Gordon, K. C.; Argazzi, R.; Woodruff, W. H.; Peterson, K. A., Bignozzie, C. A.; Dyer, R. B.; Meyer, T. J.; J. Am. Chem. Soc. 1993, 115, 10996
(b) Schoonover, J. R.; Strouse, G. F.; Dyer, R. B., Bates, W. B.; Chen, P.; Meyer, T. J.; Inorg. Chem 1996, 34, 273
(c) Spears, K. G.; Wen, X.; Zhang, R.; J. Phys. Chem. 1996, 100, 10206

[3.11] (a) Lambert, D. K.; J. Chem. Phys. 1988, 89, 3847
(b) Marti, J.; Lledos, A.; Bertran, J.; Duran, M.; J. Comput. Chem. 1992, 13, 821

[3.12] (a) Reimers, J. R.; Hush, N. S.; J. Phys. Chem. A 1999, 103, 10580
(b) Reimers, J. R.; Zeng, J.; Hush, N. S.; J. Phys. Chem. A 1996, 100, 1498 (c) Hush, N. S.; Reimers, J. R.; J. Phys. Chem. 1995, 99, 15798

[3.13] Dykstra, C. E.; J. Chem. Educ. 1988, 65, 198

[3.14] Bouanich, J. P.; J. Quant. Spectrosc. Radiat. Transfer 1978, 19, 381

[3.15] Bouanich, J. P.; Van-Thanh, N.; Rossi, I.; J. Quant. Spectrosc. Radiat. Transfer 1983, 30, 9

[3.16] Dunham, J. L.; Phys. Rev. 1932, 41, 721

[3.17] Landau, L. D.; Lifshitz, E. M.; Quantum Mechanics: Non-relativistic Theory, 2nd ed. (Pergamon, New York, 1965), p. 132

[3.18] Lambert, D. K.; J. Chem. Phys. 1991, 94, 6237

[3.19] (a) Fleischmann, M.; Hendra P. J.; McQuillan, A. J.; Chem. Phys. Lett. 1974, 26, 163
(b) Jeanmaire, D. L.; Van Duyne, R. P.; J. Electroanal. Chem. 1977, 84, 1
(c) Schatz, G. C.; Acc. Chem. Res. 1984, 17, 370

[3.20] Andres, J. L.; Marti, J.; Duran, M.; Lledos, A.; Bertran, J.; J. Chem. Phys. 1991, 95, 3521

[3.21] Bauschlicher, C. W.; Chem. Phys. Lett. 1985, 118, 307

[3.22] Bishop, D. M.; J. Chem. Phys. 1993, 98, 3179

[3.23] Kunimatsu, K.; J. Phys. Chem. 1984, 88, 2195

[3.24] Laberge, M.; Vanderkooi, J. M.; Sharp, K. A.; J. Phys. Chem. 1996, 100, 10793

[3.25] Maiti, S.; Walker, G. C.; Cowen, B. R.; Pippenger, R.; Moser, C. C.; Dutton, P. L.; Hochstrasser, R. M.; Proc. Natl. Acad. Sci. U.S.A. 1994, 91, 10360

[3.26] Volk, M.; Kholodenko, Y.; Lu, H. S. M.; Gooding, E. A.; DeGrado, W. F.; Hochstrasser, R. M.; J. Phys. Chem. B 1997, 101, 8607

[3.27] Turbitt, T. D.; Watts, W. E.; J. Organomet. Chem. 1972, 46, 109

[3.28] Sonoda, A.; Moritani, I.; J. Organomet. Chem. 1971, 26, 133

[3.29] Jones, N. D.; Marsh, R. E.; Richards, J. H.; Acta Crystallogr. 1965, 19, 330

[3.30] (a) Zerner, M. C.; Loew, G. H.; Kirchner, R. F.; Mueller-Westhoff, U. T.; J. Am. Chem. Soc. 1980, 102, 589
(b) Newton, M. D.; Ohta, K.; Zhong, E.; J. Phys. Chem. 1991, 95, 2317

[3.31] Wertheim, G. K.; Herber, R. H.; J. Chem. Phys. 1963, 38, 2106

[3.32] Traverso, O.; Scandola, F.; Inorg. Chim. Acta 1970, 4, 493

[3.33] Gilch, P.; Poellinger-Dammer, F.; Steiner, U. E.; Michel-Beyerle, M. E.; Chem. Phys. Lett. 1997, 275, 339

[3.34] Gilch, P.; Poellinger-Dammer, F.; Musewald, C.; Steiner, U. E.; Michel-Beyerle, M. E.; Science 1998, 281, 982

[3.35] Gilch, P.; PhD-thesis, TU Muenchen 1999

[3.36] Hamm, P.; Chem. Phys. 1995, 200, 415

[3.37] Wynne, K.; Hochstrasser, R. M. H.; Chem. Phys. 1995, 193, 211

[**Chapter 4**]

[4.1] (a) Honda, K.; Fujishima, A.; Nature 1972, 238, 37
(b) Bard, A. J.; Science 1980, 207, 139
(c) Tufts, B. J., et al.; Nature 1987, 326, 681
(d) Licht, S.; Hodes, G.; Tenne, R.; Manassen, J.; Nature 1987, 326, 863

[4.2] Gleria, M.; Memming, R. Z.; Phys. Chem. N. F. 1975, 98, 303

[4.3] Matsumura, M.; Mitsuda, K.; Yoshizawa, N.; Tsubomura, H.; Bull. Chem. Soc. Jpn. 1981, 54, 692

[4.4] (a) Clark, M.; Sutin, D.; J. Am. Chem. Soc. 1977, 99, 4676
(b) Hamnett, A.; Dare-Edwards, M.; Wright, R.; Seddon, K.; Goodenough, J.; J. Phys. Chem. 1979, 83, 3280

[4.5] (a) Hagfeldt, A.; Graetzel, M.; Chem. Rev. 1995, 95, 49
(b) Lanzafame, J. M.; Palese, S.; Wang, D.; Miller, R. D. J.; Muenter, A. A.; J. Phys. Chem. 1994, 98, 11020
(c) Linsebigler, A. L.; Lu, G. Q.; Yates, J. T.; Chem. Rev. 1995, 95, 735

[4.6] (a) Bawendi, M. G.; Wilson, W. L.; Rothberg, L.; Phys. Rev. Lett. 1990, 65, 1623
(b) Kamat, P. V.; Gopidas, K. R.; Dimitrijevic, N. M.; Molec. Cryst. and Liqu. Cryst. 1990, 183, 439
(c) Mittleman, D. M.; Schoenlein, R. W.; Shiang, J. J:; Phys. Rev. B 1994, 49, 14435
(d) Rehm, J. M.; McLendon, G. L. Nagasawa, Y.; Yoshihara, K.; Moser, J.; Graetzel, M.; J. Phys. Chem. 1996, 100, 9577
(e) Serpone, N.; Sharma, D. K.; Moser, J.; Chem. Phys. Lett. 1987, 136, 47

[4.7] Lettmann, C.; Hildenbrand, K.; Kisch, H.; Macyk, W.; Maier, W. F.; Applied Catalysis B, Environmental 2001, 32, 215

[4.8] Alivisatos, A. P.; J. Phys. Chem. 1996, 100, 13226

[4.9] Kay, A.; Graetzel, M.; J. Phys. Chem. 1993, 97, 6272

[4.10] (a) Evans, J. E; Springer, K. W.; Zhang, J. Z.; J. Chem. Phys. 1994, 101, 6222
(b) Kamat, P. V.; Das, S.; Thomas, K. G.; George, M. V.; Chem. Phys. Lett. 1991, 178, 75
(c) Eichberger, R.; Willig, F.; Chem. Phys. 1990, 141, 159
(d) Willig, F.; Eichberger, R.; Sundaresan, N. S.; Parkinson, B. A.; J. Am. Chem. Soc. 1990, 112, 2702

[4.11] (a) Colombo, D. P.; Roussel, K. A.; Saeh, J.; Cavaleri, J. J.; Bowman, R. M; Chem. Phys. Lett. 1995, 232, 207
(b) Burfeindt, B.; Hannappel, T.; Storck, W.; Willig, F.; J. Phys. Chem. 1996, 100, 16463
(c) Tachibana, Y.; Moser, J. E.; Graetzel, M.; Klug, D. R.; Durrant, J. R.; J. Phys. Chem. 1996, 100, 20056
(d) Cherepy, N. J.; Smestad, G. P.; Graetzel, M.; Zhang, J. Z.; J. Phys. Chem. B 1997, 101, 9342

[4.12] Huber, R.; Moser, J. E.; Graetzel, M.; Wachtveitl, J.; J. Phys. Chem. B 2002, 106, 6494

[4.13] Huber, R.; Sporlein, S.; Moser, J. E.; Graetzel, M.; Wachtveitl, J.; J. Phys. Chem. B 2000, 104, 8995

[4.14] (a) Martini, I.; Hodak, J. H.; Hartland, G. V.; Kamat, P. V.; J. Chem. Phys. 1997, 101, 8064

(b) Martini, I.; Hartland, G. V.; Kamat, P. V.; J. Phys. Chem. B, 1997, 101, 4826

[4.15] (a) Ghosh, H. N.; J. Phys. Chem. B 1999, 103, 10382
(b) Weng, Y.; Wang, Y.; Asbury, J. B.; Ghosh, H. N.; Lian, T.; J. Phys. Chem. B 2000, 104, 93
(c) Ghosh, H. N.; Asbury, J. B.; Lian, T.; J. Phys. Chem. B 1998, 102, 6482
(d) Ghosh, H. N.; Asbury, J. B.; Weng, Y.; Lian, T.; J. Phys. Chem. B 1998, 102, 10208
(e) Ellingson, R. J.; Asbury. J. B.; Ferrere, S.; Ghosh, H. N.; Lian, T.; Nozik, A.; J. Phys. Chem. B 1998, 102, 6455
(f) Asbury, J. B.; Ellingson, R. J.; Ghosh, H. N.; Ferrere, S.; Nozik, A.; Lian. T.; J. Phys. Chem. B 1999, 103, 3110

[4.16] (a) Martini, I.; Hodak, J. H.; Hartland, G. V.; J. Phys. Chem. B 1998, 102, 607
(b) Martini, I.; Hodak, J. H.; Hartland, G. V.; J. Phys. Chem. B 1998, 102, 9508
(c) Hilgendroff, M.; Sundstrom, V.; Chem. Phys. Lett. 1998, 287, 709 (d Hilgendroff, M.; Sundstrom, V.; J. Phys. Chem. B 1998, 102, 10505

[4.17] (a) Moser, J.; Graetzel, M.; J. Am. Chem. Soc. 1984, 106, 6557
(b) Kamat, P. V.; Fox, M. A.; Chem. Phys. Lett. 1983, 102, 379
(c) Moser, J. E.; Graetzel, M.; Sharma, D. K:; Serpone, N.; Helv. Chim. Acta 1985, 68, 1686
(d) Lanzafame, J. M.; Miller, R. D. J.; Muenter, A. A.; Parkinson, B. A.; J. Phys. Chem. 1992, 96, 2820
(e) Heimer, T. A.; Heilweil, E. J.; J. Phys. Chem. B 1997, 101, 10990

[4.18] (a) Lu, H.; Prieskorn, J. N.; Hupp, J. T.; J. Am. chem. Soc. 1993, 115, 4927
(b) Dang, X.; Hupp, J. T.; J. Am. Chem. Soc. 1999, 121, 8399

[4.19] Bisquert, J; Zaban, A.; Salvador, P.; J. Phys. Chem. B 2002, 106, 8774

[4.20] (b) Tani, T.; Kikuchi, S.-I.; Bull. Soc. Sci. Photogr. Jpn. 1968, 18, 1
(c) Leubner, I. H.; Photogr. Sci. Eng. 1980, 24, 138

[4.21] Gilman, P. B.; Phot. Sci. Eng. 1974, 18, 418

[4.22] (a) Morel, D. L.; Stogryn, E. L.; Ghosh, A. K.; Feng, T.; Purwin, P. E.; Shaw, R. F.; Fishman, C.; Bird, G. R.; Piechowski, A. P.; J. Phys. Chem. 1984, 88, 923
(b) Piechowski, A. P.; Bird, G. R.; Morel, D. L.; Stogryn, E. L.; J. Phys. Chem. 1984, 88, 934
(c) Iriyama, K.; Mizutani, F.; Yoshiura, M. Chem. Lett. 1980, 1399
(d) Mizutani, F.; Iijima, S.; Sasaki, K.; Tanaka, Y.; Nihon Kagaku Kaishi 1983, 6, 933
(e) Mizutani, F.; Iijima, S.; Sasaki, K.; Shimura, Y.; Ber. Bunsen-Ges. Phys. Chem. 1982, 86, 907

[4.23] (a) Morel, D. L.; Ghosh, A. K.; Feng, T.; Stogryn, E. L.; Purwin, P. E.; Shaw, R. F.; Appl. Phys. Lett. 1978, 32, 495
(b) Ghosh, K.; Feng, T.; J. Appl. Phys. 1978, 49, 5982
(c) Meier, H.; Albrecht, W.; Tschirwitz, U.; Zimmerhackl, E.; Geheeb, N.; Ber. Bunsen-Ges. Phys. Chem. 1977, 81, 592
(d) Meier, H.; Albrecht, W.; Ber. Bunsen-Ges. Phys. Chem. 1965, 69, 160
(e) Piechowski, A. P.; Bird, G. R.; Morel, D. L.; Stogryn, E. L.; J. Phys. Chem. 1984, 88, 934
(f) Saito, K.; Yokoyama, H.; Thin Solid Films 1994, 234, 526

[4.24] Sayama, K.; Hara, K.; Tsukagoshi, S.; Abe, Y.; Mori, N.; Satsuski, M.; Suga, S.; Sugihara, H.; Arakawa, H.; Chem. Commun. 2000, 1173

[4.25] Brackmann, U.; Lambdachrome Laser Dyes, Ed.: Lambda Physik GmbH, Goettingen 1994

[4.26] (a) Hartman, P.; in: Crystal Growth; Hartman, P., Ed.; North-Holland: Amsterdam 1973, p. 367
(b) Munera, G.; Moreno, F.; Gonzalez, F.; in: Reactivity of solids; Anderson, J. S.; Roberts, M. W.; Stone, T. S.; Eds.; Chapman and Hall: London 1972, p. 681

[4.27] Nuesch. F.; Graetzel, M.; Chem. Phys. 1995, 193, 1

[4.28] McRae, E. G.; J. Phys. Chem. 1957, 61, 562

[4.29] Balasubramanian, A.; Rao, C. N. R.; Spectrochimica Acta 1962, 18, 1337

[4.30] Lippert, E.; Z. Electrochem. 1957, 61, 962

[4.31] Moser, J. E.; private communication

[4.32] Nuesch, F.; Moser, J. E.; Shklover, V.; Graetzel, M.; J. Am. Chem. Soc. 1996, 118, 5420

[4.33] Gilman, P. B.; et al. in: Photographic Sensitivity, Cox, R. J., Ed.; Academic Press: London, 1973, p. 187

[4.34] (a) McRae, E. G.; Kasha, M.; J. Chem. Phys. 1958, 28, 721
(b) Kasha, M.; Rawls, H. R.; El-Bayoumi, M. A.; Pure Appl. Chem. 1965, 11, 371

[4.35] (a) Jelly, E. E.; Nature, 1936, 138, 1009
(b) Scheibe, G.; Angew. Chem. 1937, 50, 51

[4.36] Khairutdinov, R. F.; Serpone, N.; J. Phys. Chem. B 1997, 101, 2602

[4.37] Inoue, T.; Thin Solid Films 1985, 132, 21

[4.38] (a) Nakahara, H.; Fukuda, K.; Moebius, D.; Kuhn, H.; J. Phys. Chem. 1986, 90, 6144
(b) Wolthaus, L.; Schaper, A.; Moebius, D.; Chem. Phys. Lett. 1994, 225, 3227 (c) Czikkely, V.; Foersterling, H. D.; Kuhn, H.; Chem. Phys. Lett. 1970, 6, 11
(d) Czikkely, V.; Foersterling, H. D.; Kuhn, H.; Chem. Phys. Lett. 1970, 6, 207

[4.39] Mees, C.; James, T.; in Theory of Photographic Process, Macmillan, New York 1966

[4.40] Ehret, A.; Stuhl, L.; Spitler, M. T.; J. Phys. Chem. B 2001, 105, 9960

[4.41] Barazzouk, S.; Lee, H.; Hotchandani, S.; Kamat, P. V.; J. Phys. Chem. B 2000, 104, 3616

[4.42] Muniro, M.; Nozawa, T.; Tamai, N.; Shimada, K.; Yamazaki, I.; Lin, S.; Knox, R. S.; Wittershaus, B. P.; Brune, D. C.; Blankenship, R. E.; J. Phys. Chem. 1989, 93, 7503

[4.43] (a) Das, S.; Kamat, P. V.; J. Phys. Chem. B 1999, 103, 209
(b) Khazraji, A. C.; Hotchandami, S.; Das, S.; Kamat, P. V.; J. Phys. Chem. B 1999, 103, 4693

[4.44] Lossau, H.; PhD thesis, TU Muenchen, 1998

[4.45] Hartwich, G.; Lossau, H.; Ogrodnik, A.; Michel-Beyerle, M. E.; in: The Reaction Center of Photosynthetic Bacteria; Michel-Beyerle, M. E.; Ed.; Springer: Berlin, 1996, p. 199 ff

[4.46] (a) Steiner, U. E.; Ulrich, T.; Chem. Rev. 1989, 89, 51
(b) Hoff, A. J.; Lous, E. J.; in: Biophysical Effects of Steady Magnetic Fields; Eds. Maret, G.; Boccara, N.; Kiepenheuer, J.; Springer Verlag Berlin 1986

[4.47] Howe, R. F.; Graetzel, M.; J. Phys. Chem. 1985, 89, 4495

[4.48] (a) Martini, I.; Harland, G.; Kamat, P. V.; J. Phys. Chem. B 1997, 101, 4826
(b) Liu, D.; Kamat, P. V.; J. Chem. Phys. 1996, 105, 965

[4.49] Solbrand, A.; Lindstroem, H.; Rensmo, H.; Hagfeldt, A.; Lindquist, S. E.; Soedergren, S.; J. Phys. Chem. B 1997, 101, 2514

[4.50] (a) Cao, F.; Oscam, G.; Meyer, G. J.; Searson, P. C.; J. Phys. Chem. 1996, 100, 17021
(b) Dloczik, L.; Ileperuma, O.; Lauermann, I.; Perer, L. M.; Ponomarev, E. A.; Redmond, G.; Shaw, N. J.; Uhlendorf, I.; J. Phys. Chem. B 1997, 101, 10281

[4.51] (a) Kopidakis, N.; Schiff, E. A.; Park, N. G.; van de Lagemaat, J.; Frank, A. J.; J. Phys. Chem. B 2000, 104, 3930
(b) Schichthoerl, G.; Park, N. G.; A. J.; J. Phys. Chem. B 1999, 103, 782

[4.52] (a) Haque, S. A.; Tachibana, Y.; Klug, D. R.; Durrant, J. R.; J. Phys. Chem. B 1998, 102, 1745
(b) Haque, S. A.; Tachibana, Y.; Willis, R. L.; Moser, J. E.; Graetzel, M.; Klug, D. R.; Durrant, J. R.; J. Phys. Chem. B 2000, 104, 538

[4.53] Sodergren, S.; Hageldt, A.; Olsson, J.; Lindquist, S. E.; J. Phys. Chem. 1994, 98, 5552

[4.54] (a) De Jongh, P. E.; Vanmaekelbergh, D.; Phys. Rev. Lett. 1996, 77, 3427
(b) De Jongh, P. E.; Vanmaekelbergh, D.; J. Phys. Chem. B 1997, 101, 2716

[4.55] Schwarzburg, K.; Willig, F.; Appl. Phys. Lett. 1990, 58, 2520

[4.56] (a) Nelson, J; Phys. Rev. B 1999, 59, 15374
(b) Nelson, J.; Haque, S. A.; Klug, D. R.; Durrant, J. R.; Phys. Rev. B 2001, 63, 205321

[4.57] Barzykin, A. V.; Tachiya, M.; J. Phys. Chem. B 2002, 106, 4356

[4.58] (a) van de Lagemaat, J.; Frank, A. J.; J. Phys. Chem. 2000, 104, 4292
(b) van de Lagemaat, J.; Frank, A. J.; J. Phys. Chem. 2001, 105, 11194

[4.59] Weidmann, J.; PhD thesis 1998, TU-Muenchen

[**Chapter 5**]

[5.1] Watson, J.; Crick, F.; Nature 1953, 171, 737

[5.2] Szent-Gyoergi, A.; Nature 1941, 148, 157

[5.3] (a) Eley, D. D.; Spivey, D. I.; Trans. Faraday Soc. 1962, 58, 411
(b) Ladik, J.; Nature 1964, 202, 1208

[5.4] (a) Ladik, J.; Int. J. Quantum Chem. 1971, 38, 307
(b) Suhai, S.; J. Chem. Phys. 1972, 57, 5599
(c) Dee, D.; Bauer, M. E.; J. Chem. Phys. 1974, 60, 541
(d) Eley, D. D.; Mol. Cryst. Liq. Cryst. 1989, 171, 1

[5.5] (a) Sevilla, M. D.; Becker, D.; Electron Spin Reson. 1994, 14, 130
(b) Mroczka, N.; Bernhard, W. A.; Radiat. Res. 1993, 135, 155
(c) Candeias, L. P.; Steenken, S.; J. Am. Chem. Soc. 1992, 114, 699

[5.6] (a) Huettermann, J.; Voit, K.; Oloff, H.; Graeslund, A.; Rupprecht, A.; Faraday Discuss. Chem. Soc. 1984, 78, 135
(b) Jovanovic, S. V.; Simic, M. G.; J. Phys. Chem. 1986, 90, 974
(c) Jovanovic, S. V.; Simic, M. G.; Biochim. Biophys. Acta 1989, 1008, 39

[5.7] Seidel, C. A. M.; Schulz, A.; Sauer, M. H. M.; J. Phys. Chem. 1996, 100, 5541

[5.8] Sugiyama, H.; Saito, I.; J. Am. Chem. Soc. 1996, 118, 7063

[5.9] (a) Saito, I.; Takayama, M.; Sugiyama, H.; Nakatani, K.; J. Am. Chem. Soc. 1995, 117, 6406
(b) Steenken, S.; Chem. Rev. 1989, 89, 503
(c) Steenken, S.; Jovanovic,, S. V.; J. Am. Chem. Soc. 1997, 119, 617

[5.10] (a) Matsugo, S.; Kawanishi, S.; Yamamoto, K.; Sugiyama, H.; Matsuura, T.; Saito, I.; Angew. Chem. Int. Ed. Engl. 1991, 30, 1351
(b) Ito, K.; Inoue, S.; Yamamoto, K.; Kawanishi, S.; J. Biol. Chem. 1993, 268, 13221
(d) Ly, D.; Kan, Y.; Armitage, B.; Schuster, G. B.; J. Am. Chem. Soc. 1996, 118, 8747
(e) Breslin, D. T.; Schuster, G. B.; J. Am. Chem. Soc. 1996, 118, 2311
(f) Muller, J. G.; Hickerson, R. P.; Perez, R. J.; Burrows, C. J.; J. Am. Chem. Soc. 1997, 119, 1501
(g) Stemp, E. D. A.; Arkin, M. R.; Barton, J. K.; J. Am. Chem. Soc. 1997, 119, 2921
(h) Carter, P. J.; Cheng, C. C.; Thorp, H. H.; J. Am. Chem. Soc. 1998, 120, 632

[5.11] (a) Kasai, H.; Yamaizumi, Z.; Berger, M.; Cadet, J.; J. Am. Chem. Soc. 1992, 114, 9692
(b) Cadet, J.; Berger, M.; Buchko, G. W.; Joshi, P. C.; Raoul, S.; Ravanat, J. L.; J. Am. Chem. Soc. 1994, 116, 7403
(c) Raoul, S.; Berger, M.; Buchko, G. W.; Joshi, B. M.; Weinfeld, M.; Cadet, J.; J. Chem. Soc., Perkin Trans. 2 1996, 371
(d) Cullis, P. M.; Malone, M. E.; Merson-Davies, L. A.; J. Am. Chem. Soc. 1996, 118, 2775
(e) Kino, K.; Saito, I.; Sugiyame, H.; J. Am. Chem. Soc. 1998, 120, 7373

[5.12] (a) Demple, B.; Harrison, L.; Annu. Rev. Biochem. 1994, 63, 915
(b) Steenken, S.; Biol. Chem. 1997, 378, 1293

[5.13] (a) Hall, D. B.; Holmlin, E.; Barton, J. K.; Nature 1996, 382, 731
(b) Hall, D. B.; Barton, J. K.; J. Am. Chem. Soc. 1997, 119, 5045
(c) Dandliker, P. J.; Holmlin, R. E.; Barton, J. K.; Science 1997, 275, 1465
(d) Arkin, M. R.; Stemp, E. D. A.; Pulver, S. C.; Barton, J. K.; Chem. Biol. 1997, 4, 389

[5.14] Gasper, S. M.; Schuster, G. B.; J. Am. Chem. Soc. 1997, 119, 12762

[5.15] Nunez, M. E.; Hall, D. B.; Barton, J. K.; Chem. Biol. 1999, 6, 85

[5.16] (a) Levich, V. O.; Adv. Electrochem. 1966, 4, 249
(b) Kestner, N. R.; Logan, J.; Jortner, J.; J. Phys. Chem. 1974, 78, 2148

(c) Ulstrup, J.; Jortner, J.; J. Chem. Phys. 1975, 63, 4358
(d) Jortner, J.; J. Chem. Phys. 1976, 64, 4860
(e) Marcus, R. A.; J. Chem. Phys. 1984, 8, 4494

[5.17] Giese, B.; Spichty, M.; ChemPhysChem 2000, 1, 195

[5.18] Berlin, Y. A.; Burin, A. L.; Ratner, M. A.; J. Phys. Chem. A 2000, 104, 443

[5.19] Bixon, M.; Jortner, J.; J. Chem. Phys. 1997, 107, 5154

[5.20] Efrima, S.; Bixon, M.; Chem. Phys. 1976, 13, 447

[5.21] Brun, A. M.; Harriman, A. J.; J. Am. Chem. Soc. 1992, 114, 3656

[5.22] (a) Lewis, F. D.; Wu, T.; Zhang, Y.; Letsinger, R. L.; Greenfield, S. R.; Wasielewski, M. R.; Science 1997, 277, 673
(b) Lewis, F. D.; Wu, T.; Liu, X.; Letsinger, R. L.; Greenfield, S. R.; Miller, S. E.; Wasielewski, M. R.; J. Am. Chem. Soc. 2000, 122, 2889

[5.23] Shafirovich, V.; Dourandin, A.; Huang, W.; Luneva, N. P.; Geacintov, N. E.; Phys. Chem. Chem. Phys. 2000, 2, 4399

[5.24] (a) Sachs, S. B.; Dudek, S. P.; Hsung, R. P. Sita. L. R.; Smalley, J. F.; Newton, M. D.; Feldberg, S. W.; Chidsey, C. E. D.; J. Am. Chem. Soc. 1997, 119, 10563
(b) Creager, S.; Yu, C. J.; Bamdad, C.; Ot'Connor, S.; MacLean, T.; Lam, E.; Chong, Y.; Olsen, G. T.; Luo, J.; Gozin, M.; Kayyem, J. F.; J. Am. Chem. Soc. 1999, 121, 1059
(c) Davis, W. B.; Svec, W. A.; Ratner, M. A.; Wasielewski, M. R.; Nature 1998, 396, 60
(d) Finckh, P.; Heitele. H.; Volk, M.; Michel-Beyerle, M. E.; J. Phys. Chem. 1988, 92, 6584
(e) Benniston, A. C.; Goulle, V.; Harriman, A.; Lehn, J.-M.; Marezinke, B.; J. Phys. Chem. 1994, 98, 7798

[5.25] (a) Page, C. C.; Moser, C. C.; Chen, X.; Dutton, P. L.; Nature 1999, 402, 47
(b) Mutz, M. W.; Case, M. A.; Wishart, J. F.; Ghadiri, M. R.; McLendon, G. L.; J. Am. Chem. Soc. 1999, 121, 858, 859
(c) Isied, S. S.; Ogawa, M. Y.; Wishart, J. F.; Chem. Rev. 1992, 92, 381
(d) Winkler, J. R.; Gray, H. B.; Chem. Rev. 1992, 92, 369

[5.26] (a) Closs, G. L.; Miller, J. R.; Science 1988, 240
(b) Leland, B. E.; Joran, A. D.; Felker, P. M.; Hopfield, J. J.; Zewail, A. H.; Dervan, P. B.; J. Am. Chem. Soc. 1985, 89, 5571
(c) Oevering, H.; Paddon-Row, M. N.; Heppener, M.; Oliver, A. M.; Cotsaris, E.; Verhoeven, J. W.; Hush, N. S.; J. Am. Chem. Soc. 1987, 109
(d) Carter, M. J.; Rowe, G. K.; Richardson, J. N.; Tender, L. M.; Terrill, R. H.; Murray, R. W.; J. Am. Chem. Soc. 1995, 117, 2896

[5.27] (a) Fukui, K.; Tanaka, K.; Angew. Chem. 1998, 110, 167
(b) Fukui, K.; Tanaka, K.; Nucleic, Acids Res. 1996, 24, 3962
(c) Fukui, K.; Inwane, K; Shimidzu, T.; Takano, Y.; Tetrahedron Lett. 1996, 37, 4983
(d) Fukui, K.; Morimoto, M.; Segawa, H.; Tanaka, K. Shimidzu, T.; Bioconjugate Chem. 1996, 7, 349

[5.28] Liu, Y.-P.; Newton, M. D.; J. Phys. Chem. 1994, 98, 7162

[5.29] Tavernier, H. L.; Fayer, M. D; J. Phys. Chem. 2000, 104, 11541

[5.30] Cohen, J. S.; Ed. (1989) Oligodeoxynucleotides: Antisense Inhibitors of Gene Expression, CRC Press, Boca Raton, FL.

[5.31] Symon, R. H.; Ed. (1989) Nucleic Acid Probes, CRC Press, Boca Raton, FL.

[5.32] (a) Kubota, Y.; Motoda, Y.; Shigemune, Y.; Fujisaki, Y.; Photochem. Photobiol. 1979, 29, 1099
(b) Georghiou, S.; Photochem. Photobiol. 1977, 26, 59

[5.33] (a) Asseline, U.; Toulme, F.; Thuong, N. T.; Delarue, M.; Montenay-Garestier, T.; Hélène, C.; EMBO J. 1984, 3, 795
(b) Asseline, U.; Delarue, M.; Lancelot, G.; Toulme, F.; Thuong, N. T.; Montenay-Garestier, T.; Hélène, C.; Proc. Natl. Acad. Sci. U.S.A. 1984, 81, 3297

[5.34] (a) Sun, J.; Rougee, M.; Delarue, M.; Montenay-Garestier, T.; Hélène, C.; J. Phys. Chem. 1990, 94, 968
(b) Marty, A.; Bourdeaux, M.; Dell'Amico, M.; Viallet, P.; Biophys. J. 1986, 13, 251
(c) Fan, P.; Haerd, T.; Kearns, D. R.; J. Phys. Chem. 1989, 93, 6615

[5.35] Nastasi, M.; Morris, J. M.; Rayner, D. M.; Soligy, V. L.; Szabo, A. G.; Williams, D. F.; Williams, R. E.; Yip, R. W.; J. Am. Chem. Soc. 1976, 98, 3979

[5.36] (a) Jin, R.; Gaffney, B. L.; Wang, C.; Jones, R. A.; Breslauer, K. J.; Proc. Natl. Acad. Sci. U.S.A. 1992, 89, 8832
(b) Lu, M.; Guo, Q.; Kallenbach, N. R.; Biochemistry 1993, 32, 598

[5.37] Spassky, A.; Angelov, D.; Biochemistry 1997, 36, 6571

[5.38] Giese, B.; Wessley, S.; Sporman, M.; Lindemann, U.; Meggers, E.; Michel-Beyerle, M. E.; Angew. Chem. 1999, 111, 1050 and Angew. Chem. Int. Ed. 1999, 38, 996

[5.39] Meggers, E.; Kusch, D.; Spichty, M.; Willie, U.; Giese, B.; Angew. Chem. 1998, 110, 474 and Angew. Chem. Int. Ed. Engl. 1998, 37, 460

[5.40] Nakatani, K, Dohno, C.; Nakamura, T.; Saito, I.; Tetrahedron Lett. 1998, 39, 2779

[5.41] (a) Melvin, T. Cunniffe, S.; Papworth, D.; Roldan-Ajona, T.; O'Neill, P.; Photochem. Photobiol. 1997, 65, 660
(b) Sistare, M. F.; Codden, S. J.; Heimlich, G.; Thorp, H. H.; J. Am. Chem. Soc. 2000, 122, 4742

[5.42] (a) Kawanishi, S.; Oidawa, S.; Murata, M.; Tsukitiome, H.; Saito, I.; Biochemistry 1999, 38, 16733
(b) Ito, K.; Kawanishi, S.; Biochemistry 1997, 36, 1774

[5.43] (a) Holmlin, R. E.; Dandliker, P. J.; Barton, J. K.; Angew. Chem. 1997, 109, 2830 and Angew. Chem. Int. Ed. Engl. 1997, 36, 2714
(b) Hall, D. B.; Kelley, S. O., Barton, J. K.; Biochemistry 1998, 37, 15933

[5.44] Voityuk, A. A.; Jortner, J.; Bixon, M.; Roesch, N.; Chem. Phys. Lett. 2000, 324, 430

[5.45] Bixon, M.; Jortner, J.; Adv. Chem. Phys. 1999, 106, 35

[5.46] Hess, S.; Goetz, M.; Davis, W. B.; Michel-Beyerle, M. E.; J. Am. Chem. Soc. 2001, 123, 10046

[5.47] Voityuk, A. A.; Roesch, N.; Bixon, M.; Jortner, J.; J. Phys. Chem. B 2000, 104, 9740

[5.48] Lewis, F. D.; Liu, X.; Liu, J.; Miller, S. E.; Hayes, R. T.; Wasielewski, M. R.; Nature 2000, 406, 51

[5.49] Bixon, M.; Giese, B.; Wessely, S.; Langenbacher, T.; Michel-Beyerle, M. E.; Jortner, J.; Proc. Natl. Acad. Sci. USA 1999, 96, 11713

[5.50] (a) Neta, P.; J. Phys. Chem. 1979, 83, 3096
(b) Jones, G. H.; Farahat, M. S.; Greenfield, S.; Gosztola, D. J.; Wasielewski, M. R.; Chem. Phys. Lett. 1994, 229, 40

[5.51] Hess, S.; Davis, W. B.; Voityuk, A. A.; Roesch, N.; Michel-Beyerle, M. E.; Ernsting, N. P.; Kovalenko, S. A.; Lustres, J. L. P.; ChemPhysChem 2002, 5, 452

[5.52] Kelley, S. O.; Barton, J. K.; Chem. Biol. 1998, 5, 413

[5.53] Hale, J. M.; in Reactions of Molecules at Electrodes; Hush, N. S.; Ed.; Wiley Interscience: New York, 1971, pp. 229

[5.54] Jortner, J.; Bixon, M.; J. Chem. Phys. 1988, 88, 167

[5.55] (a) Giese, B. Acc. Chem. Res. 2000, 33, 631-636
(b) Lewis, F. D.; Letsinger, R. L.; Wasielewski, M. R. Acc. Chem. Res. 2001, 34, 159-170

[5.56] (a) Brunschwig, B. S.; Ehrenson, S.; Sutin, N. J. Am. Chem. Soc. 1984, 106, 6858
(b) Yonemoto, E. H.; Saupe, G. B.; Schmehl, R. H.; Hubig, S. M.; Riley, R. L.; Iverson, B. L.; Mallouk, T. E. J. Am. Chem. Soc. 1994, 116, 4786

List of Publications

1. SPECTATOR BONDS AS SENSITIVE CARBONYL SENSORS FOR CHARGE TRANSFER REACTIONS ON THE FEMTO-SECOND TIME SCALE

   M. Volk, P. Gilch, C. Kompa, R. Haselsberger, P. Haerter, M. Stoeckl, W. Scherer, K. Latzel and M.E. Michel-Beyerle; J. Phys. Chem. A 2000, 104 (21), p. 4984 - 4988

2. DYNAMICS OF HOLE TRAPPING BY G, GG and GGG IN DNA

   W. B. Davis, I. Naydenova, R. Haselsberger, A. Ogrodnik, B. Giese and M.E. Michel-Beyerle; Angew. Chem. Int. Ed. 2000, 39, No. 20, p. 3649 - 3652

3. DISTANCE-DEPENDENT ACTIVATION ENERGIES FOR HOLE INJECTION FROM PROTONATED 9-ALKYL-AMINO-6-CHLORO-2-METHOXY-ACRIDINE INTO DUPLEX DNA

   W. B. Davis, S. Hess, I. Naydenova, R. Haselsberger, A. Ogrodnik, M. D. Newton and M. E. Michel-Beyerle; J. Am. Chem. Soc. 2002, 124 (11); p. 2422 - 2423

Danksagung

Mein Dank gilt all jenen, die zum Gelingen dieser Arbeit beigetragen haben, insbesondere:

Frau Prof. M.-E. Michel-Beyerle dafür, dass sie es mir ermöglichte, auf dem Gebiet der Laser-Spektroskopie zu arbeiten und die interessante Welt der Ladungstransfer-Reaktionen zu entdecken, sowie für die stetige Betreuung und Unterstützung meiner Arbeit,

Dr. Martin Volk, Dr. Peter Gilch und Dr. Christian Musewald und vor allem Christian Kompa für die Einführung in das Gebiet der Femtosekunden-Spektroskopie und die jederzeitige Unterstützung und technische Hilfeleistung bei Aufbau und Durchführung der IR-Experimente,

Dr. Alexander Ogrodnik für rat- und tatkräftige Unterstützung bei der (Wieder)-Inbetriebnahme des Nanosekunden-Labors und jederzeitige Diskussionsbereitschaft bei wichtigen Fragen der TiO_2- und DNA-Experimente,

Frau Dr. Izabela Naydenova für die erfolgreiche Zusammenarbeit, den steten und unermüdlichen Einsatz für das Fortschreiten dieser Arbeit, die stimulierenden Diskussionen und das angenehme Labor-Sharing,

Dr. William B. Davis, Dr. Stephan Hess und Dr. Mirco Götz für die gute Kooperation, die lehrreichen Einblicke in die Oxidationsdynamik der DNA und die wichtigen Erkenntnisse aus dem Femtosekunden-Labor,

Frau Reischl und Frau Gabi Dietrich für die Hilfe bei organisatorischen Fragen und die kompetente Führung des Sekretariats,

Till v. Feilitzsch, Tanja Schüttrigkeit, Pancho Tzankov, Dr. Alexej Chugreev, Dr. Rainer Feick, Dr. Gagik Gurzadyan, Dr. Andreas Kummer, Dr. Thomas Langenbacher und alle bereits Genannten für die Zusammenarbeit und die gute Atmosphäre in unserer Arbeitsgruppe.

sowie meinen Eltern für Ünterstützung und Rückhalt auf allen anderen Gebieten.